



**Pd doped mesoporous biochar catalysts for the selective
hydrogenation of alkynes to alkenes.**

being a thesis submitted in fulfilment of the
Requirements for the degree of

MSc (by research)

University of Hull

Karl Hornsby

March 2024

Acknowledgements

I would also like to thank my supervisors Dr Martin Taylor and Dr Grazia Francesconi for all their support. I would also like to thank Dr Martin Taylor as a friend for sticking with me, pushing me to be better and for not giving up on me. I would also like to thank my mother for all her years of support.

I would finally like to thank Benedicts Sandwich Bar, your breakfast wraps kept me going and my spirits high.

Thesis Summary

The quest to develop Pd doped, sustainable catalysts for the selective hydrogenation of phenylacetylene resulted in the synthesis of two families of materials. Derived from lignocellulosic biomass residues, specifically barley straw, bulk and mesoporous biochars were created and characterised (TGA, CHN, N₂ physisorption, PXRD, FTIR, SEM/EDX and HRTEM). Bulk biochars were produced after pyrolysis across a range of temperatures (500, 600, 700 and 800 °C) of leached barley straw, resulting in a carbon support material with low surface area but customisable Lewis acidity. Mesoporous biochars were produced following an elegant pre and post-treatment approach by using sacrificial KOH to generate a porous network. Using this method, biochars were created with an available surface area up to 1436.81 m² g⁻¹ (ABC-1), and a pore size as small as ~4 nm. Individually, the materials were all impregnated with a nominal loading of 1 wt% Pd which generated dispersed nanoparticles. The Pd nanoparticles were of similar size across all materials (averaging ~6.2 nm), within error and proved to be a minimum requirement for the catalytic transformation of phenylacetylene. By investigating the role of reaction temperature and how the structure (physical and chemical) of a biochar catalyst support can direct hydrogenation reactions, it was found that for a bulk biochar, by increasing pyrolysis temperature a hydrogen driven cascade reaction occurred. This meant that induced chemical functionality of the support led to the desired product, styrene, being consumed to ethylbenzene. For the case of mesoporous supports, by dispersing Pd sites across the material, it is believed that styrene re-adsorption was not favoured as the selectivity towards ethylbenzene was substantially lower than all bulk support testing. Additionally, when following normalised initial rates by factoring in the total Pd content of the catalyst, it was found that the mesoporous catalysts were superior across the board in terms of reaction rate and product selectivity.

Table of contents

Acknowledgements	2
1.0 Introduction	12
1.1 What is a catalyst?	13
1.2 What is Biochar?	17
1.2.1 Uses of Biochar	19
1.2.2 Activated Carbon	25
1.3 Catalytic hydrogenation reactions	27
1.4 The selective hydrogenation of phenylacetylene to styrene	27
1.5 Aims and Objectives	31
2.0 Methodology	34
2.1 Pre-Treatment of Barley Straw	34
2.2 Slow Pyrolysis of Barley Straw	36
2.2.1 Biochar Derived Catalyst synthesis	36
2.3 Mesoporous Biochar catalyst preparation & use	36
2.3.1 Mesoporous Honeycomb Biochar Production	36
2.3.2 Mesoporous Honeycomb Biochar Derived Catalyst synthesis	38
2.4 Catalyst Testing	39
2.5 Instrumentation	41
2.5.1 Gas chromatography (GC-FID)	41
2.5.2 Fourier transform infrared spectroscopy (FTIR)	42
2.5.3 Thermogravimetric analysis (TGA)	43
2.5.4 Ultimate Analysis	45
2.5.5 Scanning Electron Microscopy (SEM)	46
2.5.6 Transmission Electron Microscopy (TEM)	47
2.5.7 Brunauer–Emmett–Teller (BET) theory	48
2.5.8 Powder X-ray Diffraction (PXRD)	51
3.0 The textural and chemical properties of bulk and mesoporous biochars	55
3.1 Characterisation of Raw and Leached Barley Straw	55
3.1.1 Thermogravimetric Analysis (TGA)	55
3.1.2 Ultimate analysis of raw and leached barley straw	59
3.1.3 FTIR of raw and leached barley straw	59
3.1.4 SEM of raw and leached barley straw	61

3.2 Characterisation of bulk biochars	62
3.2.1 Thermogravimetric analysis of bulk biochars	63
3.2.2 Ultimate analysis of bulk biochars	64
3.2.3 FTIR analysis of bulk biochars	65
3.2.4 SEM/EDX analysis of bulk biochars.....	66
3.2.5 Porosity of bulk biochars	68
3.3 Characterisation of Pd doped bulk biochars	68
3.3.1 Thermogravimetric analysis of Pd doped bulk biochars	69
3.3.2 Textural properties of Pd doped bulk biochars	69
3.3.3 FTIR of Pd doped bulk biochars.....	70
3.3.4 PXRD of Pd doped bulk biochars	71
3.3.5 SEM/EDX of Pd doped bulk biochars	72
3.3.6 TEM of Pd doped bulk biochars with particle size histograms.	74
3.4 Characterisation of high surface area mesoporous biochars	80
3.4.1 Thermogravimetric analysis of mesoporous biochars.....	80
3.4.2 Textural properties of high surface area mesoporous biochars.	81
3.4.3 FTIR of mesoporous biochars	83
3.4.3 XRD of mesoporous biochars	84
3.5 Characterisation of high surface area, Pd doped mesoporous biochars	85
3.5.1 Thermogravimetric analysis of mesoporous Pd doped biochars	86
3.5.2 Textural properties of mesoporous Pd doped biochars	86
3.5.3 FTIR comparison of mesoporous Pd doped biochars	87
3.5.4 XRD of mesoporous Pd doped biochars	88
3.5.5 SEM/EDX of mesoporous Pd doped biochars	89
3.5.6 TEM of mesoporous Pd doped biochars with particle size histograms	91
4.0 The Selective hydrogenation of phenylacetylene using a bulk and mesoporous biochars.....	97
4.1 Bulk biochar catalyst hydrogenation reactions	97
4.1.1 Bulk biochar reactions at 30 °C	98
4.1.2 Bulk biochar reaction at 50 °C	100
4.1.3 Bulk biochar reaction at 70 °C	102
4.1.4 Initial rate for Bulk biochar reaction	105
4.1.5 Reaction activation energy for the Pd/BC catalysts	106
4.2 Mesoporous biochar catalyst hydrogenation reactions	108

4.2.1 Mesoporous biochar reaction at 30 °C	108
4.2.2 Mesoporous biochar reaction at 50 °C	110
4.2.3 Mesoporous biochar reaction at 70 °C	111
4.2.4 Initial rate for mesoporous biochar reaction	113
4.2.5 Reaction activation energy for the Pd/BC catalysts	114
4.3 Bulk and mesoporous biochar data repository	115
4.4 Pd doped biochars – suggested reaction mechanisms	116
5.1 Conclusions	119
5.2 Future Work	120
6.0 References	123

Table of Figures

Figure 1: Figure 1: Activation energy diagram for a catalysed and non-catalysed reaction (Modified from https://www.chemengonline.com/catalysis-fundamentals/)	13
Figure 2: Example reaction of hydrogenation	17
Figure 3: Methods by which biochar can be applied to pollution remediation for (a) metal extraction and (b) organic contamination (modified from reference 42)	21
Figure 4: Uses of activated carbon ⁸⁰	27
Figure 5: Reaction mechanism for the selective hydrogenation of phenylacetylene to styrene	28
Figure 6: Possible surface adsorption profiles of styrene on a catalyst surface	31
Figure 7: Graphical representation of overall bulk and mesoporous Pd/biochar methodology	35
Figure 8: Radleys Starfish parallel reactor platform operating the hydrogenation of four reactions simultaneously	40
Figure 9: LECO-Agilent Technologies 7890A Gas Chromatograph with flame ionisation detector	40
Figure 10: Thermo Scientific Nicolet iS5 without the PIKE MIRacle single reflection horizontal ATR accessory	43
Figure 11: Figure 10: LECO TGA 701 thermogravimetric analyser for multiple, large samples under parallel conditions	44
Figure 12: Mettler Toledo TGA/DSC 1 STAR system for small scale samples	45
Figure 13: Fisons Instruments EA 1108 CHNS elemental analyzer	46
Figure 14: Zeiss Evo 60 SEM with an Oxford instruments X-Max 80	47
Figure 15: FEI Titan3 Themis 300 Transmission Electron Microscope	48
Figure 16: Micromeritics TriStar Surface Area and Porosity Analyzer with degassing station	49
Figure 17: PANalytical Empyrean series 2 diffractometer	53
Figure 18 Weight loss curve for raw and leached barley straw	58

Figure 19: Derivative Weight Loss Graph for raw and leached barley straw	59
Figure 20: FTIR of raw and leached barley straw.....	60
Figure 21: SEM of raw barley straw (0.25 mm grains), where A and B are at the same magnification but in different regions on the sample.....	62
Figure 22: SEM image of leached barley straw, where A and B are at the same magnification but in different regions on the sample.....	62
Figure 23: TGA Weight loss curve for Bare 800 °C Biochar	64
Figure 24: FTIR of biochar made at 500 °C, 600 °C, 700 °C and 800 °C.....	66
Figure 25: SEM images of [A] BC/500 biochar at a magnification of X100 and [B] BC/500 biochar at a magnification of X1000.....	67
Figure 26: SEM images of: [A] BC/600 biochar at a magnification of X100 and [B] BC/600 biochar at a magnification of X500.....	67
Figure 27: SEM images of: [A] BC/700 biochar at a magnification of X100 and [B] BC/700 biochar at a magnification of X1000.....	68
Figure 28: TGA weight loss curve for Pd doped bulk biochars Pd/BC500, Pd/BC600, Pd/BC700 and Pd/BC800	69
Figure 29: FTIR of 1 wt% Pd/BC500, 1 wt% Pd/BC600, 1 wt% Pd/BC700 and 1 wt% Pd/BC800	70
Figure 30: PXRD of Pd doped bulk biochar 1 wt% Pd/BC500, 1 wt% Pd/BC600, 1 wt% Pd/BC700 and 1 wt% Pd/BC800	71
Figure 31: SEM image of [A] Pd/BC500 biochar at a magnification of X450, [B] Pd/BC500 biochar at a magnification of X1000, [C] Pd/BC500 biochar at a magnification of X4000	73
Figure 32: SEM image of [A] Pd/BC600 biochar at a magnification of X400, [B] Pd/BC600 biochar at a magnification of X1140, [C] Pd/BC600 biochar at a magnification of X2000	73
Figure 33: SEM image of [A] Pd/BC700 biochar at a magnification of X450, [B] Pd/BC700 biochar at a magnification of X1350, [C] Pd/BC700 biochar at a magnification of X1500	73
Figure 34: SEM image of [A] Pd/BC800 biochar at a magnification of X400, [B] Pd/BC800 biochar at a magnification of X1200, [C] Pd/BC800 biochar at a magnification of X1350.....	74
Figure 35: TEM images of [A] Site A of Pd/BC500, [B] Site B of Pd/BC500 at similar magnifications and [C] An atomically resolved Pd nanoparticle with accompanying lattice spacing	76
Figure 36: Pd particle size distribution for Pd/BC500	77
Figure 37: TEM images of [A] Site A of Pd/BC600 at low magnification and [B] Site B of Pd/BC600 at high magnification.....	77
Figure 38: Pd particle size distribution for Pd/BC600	78
Figure 39: Figure 39: TEM images of [A]site A of Pd/BC700 [B] Site B of Pd/BC700 both at similar magnification	78
Figure 40: Pd particle size distribution for Pd/BC700	79
Figure 41: TEM images of [A] Pd/BC800 [B] Pd/BC800	79
Figure 42: Pd particle size distribution for Pd/BC800	80

Figure 43: TGA weight loss curve for mesoporous biochars ABC-1, ABC-0.5 and ABC-0.25.....	81
Figure 44: A stacked plot of BET Isotherms for ABC-1, ABC-0.5 and ABC-0.25	83
Figure 45: FTIR spectra of ABC-1, ABC-0.5, ABC-0.25.....	84
Figure 46: PXRD of mesoporous biochars ABC-1, ABC-0.5 and ABC-0.25 with comparison to the bulk biochar BC/800	85
Figure 47: TGA weight loss curve for mesoporous Pd doped biochars Pd/ABC-1, Pd/ABC-0.5 and Pd/ABC-0.25	86
Figure 48: A stacked plot of BET Isotherms for Pd/ABC-1, Pd/ABC-0.5 and Pd/ABC-0.25.....	87
Figure 49: FTIR of Pd/ABC-1, Pd/ABC-0.5 and Pd/ABC-0.25.....	88
Figure 50: PXRD of mesoporous Pd doped biochars Pd/ABC-1, Pd/ABC-0.5 and Pd/ABC-0.25 (the data shown for Pd/ABC-0.25 has been divided by 100x to bring its intensity in line with the other two samples due to different sample amounts used)	89
Figure 51: SEM image of [A] Pd/ABC-1 at a magnification of X500, [B] Pd/ABC-1 at a magnification of X2500 and [C] Pd/ABC-1 at a magnification of X25000	90
Figure 52: SEM image of [A] Pd/ABC-0.5 at a magnification of X500, [B] Pd/ABC-0.5 at a magnification of X2500 and [C] Pd/ABC-0.5 at a magnification of X25000	91
Figure 53: SEM image of [A] Pd/ABC-0.25 biochar at a magnification of X500, [B] Pd/ABC-0.25 biochar at a magnification of X2500 and [C] Pd/ABC-0.25 biochar at a magnification of X25000.....	91
Figure 54: Representative TEM images of [A] Pd/ABC-1 and [B] Pd/ABC-1.....	93
Figure 55: Histogram for measured Pd particle sizes for Pd/ABC-1	93
Figure 56: Representative TEM images of Pd/ABC-0.25 at varying magnification (Image A, B and C) to show particle dispersion and agglomerates.....	94
Figure 57: Histogram for measured Pd particle sizes for Pd/ABC-0.25.....	94
Figure 58: [A] conversion of phenylacetylene at 30 °C. [B] Selectivity of styrene and [C] Selectivity for ethylbenzene for Pd/BC500, Pd/BC600, Pd/BC700 and Pd/BC800.....	99
Figure 59: [A] conversion of Phenylacetylene at 50 °C. [B] Selectivity of Styrene at 50 °C and [C] Selectivity for Ethylbenzene at 50 °C 1 wt% BC/500, 1 wt% BC/600, 1 wt% BC/700 and 1 wt% BC/800.....	101
Figure 60: [A] conversion of Phenylacetylene at 50 °C. [B] Selectivity of Styrene at 50 °C and [C] Selectivity for Ethylbenzene at 50 °C 1 wt% BC/500, 1 wt% BC/600, 1 wt% BC/700 and 1 wt% BC/800.....	104
Figure 61: Initial rate of reaction for Pd/BC500, Pd/BC600, Pd/BC700 and Pd/BC800 at 30 °C 50 °C and 70 °C.....	106
Figure 62: [A] conversion of Phenylacetylene at 30 °C. [B] Selectivity of Styrene at 30 °C and [C] Selectivity for Ethylbenzene at 30 °C for Pd/ABC-1, Pd/ABC-0.5 and Pd/ABC-0.25.....	109
Figure 63: [A] conversion of Phenylacetylene at 50 °C. [B] Selectivity of Styrene at 50 °C and [C] Selectivity for Ethylbenzene at 50 °C for Pd/ABC-1, Pd/ABC-0.5 and Pd/ABC-0.25.....	111
Figure 64: [A] conversion of Phenylacetylene at 70 °C. [B] Selectivity of Styrene at 70 °C and [C] Selectivity for Ethylbenzene at 70 °C for Pd/ABC-1, Pd/ABC-0.5 and Pd/ABC-0.25.....	113

Figure 65: [A]Initial rate of reaction for Pd/ABC-1, Pd/ABC-0.5 and Pd/ABC-0.25 at 30 °C 50 °C and 70 °C. [B] Initial rate of reaction for Pd/BC500, Pd/BC600, Pd/BC700 and Pd/BC800 at 30 °C 50 °C and 70 °C	114
Figure 66: Proposed reaction mechanisms for both the Pd doped BC and ABC families	117

Table of Tables

Table 1: Comparison between Homogeneous and Heterogeneous Catalysis ¹⁶	16
Table 2: Comparison of all parameters for slow, fast, and Flash Pyrolysis	18
Table 3: Examples of how biochar can be used in catalysis.	23
Table 4: Examples of how Activated Carbon can be used in catalysis.	26
Table 5: Previous catalytic packages used for phenylacetylene hydrogenation.	29
Table 6: Results from the Proximate analysis of raw and leached barley straw	57
Table 7: Results from the Ultimate analysis of raw and leached barley straw	59
Table 8: Results from the ultimate analysis of raw and leached barley straw compared to that of biochar produces at 500°C, 600 °C, 700 °C and 800°C	65
Table 9: Results from the Ultimate analysis, TGA and BET of 1 wt% Pd/BC500, Pd/BC600, Pd/BC700, and Pd/BC800	70
Table 10: The reduction in silicon content in biochars by varying pyrolysis temperature.	72
Table 11: Measured loading of Pd on bulk biochar through EDX	74
Table 12: Results of TEM and XRD showing Pd sizing and loading.	75
Table 13: Results from the ultimate analysis, TGA and BET of ABC-1, ABC-0.5, ABC-0.25	82
Table 14: Results from the Ultimate analysis, TGA and BET of 1 wt% Pd/ABC-1, 1 wt% Pd/ABC-0.5 and 1 wt% Pd/ABC-0.25	87
Table 15: Measured loading of Pd on mesoporous biochar through EDX	91
Table 16: Table 15: Tables showing estimated and measured Pd size.	92
Table 17: Summary of all characterisations performed, across all samples.	95
Table 18: Table showing the conversion of Phenylacetylene, Selectivity for styrene and ethylbenzene for Pd/BC500, Pd/BC500, Pd/BC500 and Pd/BC500 at 30°C	100
Table 19: Conversion of Phenylacetylene, Selectivity for styrene and ethylbenzene for Pd/BC500, Pd/BC500, Pd/BC500 and Pd/BC500 at 50°C, comparing with Pd free BC supports	102
Table 20: Table showing the conversion of Phenylacetylene, Selectivity for styrene and ethylbenzene for 1 wt% Pd/BC500, 1 wt% Pd/BC500, 1 wt% Pd/BC500 and 1 wt% Pd/BC500 at 70°C.	104
Table 21: shows the initial rate for as well as the activation energy for Pd/BC500, Pd/BC600, Pd/BC700 and Pd/BC800	107
Table 22: Table showing the conversion of Phenylacetylene, Selectivity for styrene and ethylbenzene for Pd/ABC-1, Pd/ABC-0.5 and Pd/ABC-0.25 at 30 °C	109
Table 23: Table showing the conversion of Phenylacetylene, Selectivity for styrene and ethylbenzene for Pd/ABC-1, Pd/ABC-0.5 and Pd/ABC-0.25 at 50 °C.	111

Table 24: Table showing the conversion of Phenylacetylene, Selectivity for styrene and ethylbenzene for Pd/ABC-1, Pd/ABC-0.5 and Pd/ABC-0.25 at 70 °C	113
Table 25: Shows the initial rate for as well as the activation energy for Pd/ABC-1, Pd/ABC-0.5 and Pd/ABC-0.25	115
Table 26: An overview of phenylacetylene conversion and reaction selectivities, across all temperatures and catalysts after 360 min.....	116

Chapter 1

Introduction

1.0 Introduction

As we edge closer to the 1.5°C increase in global temperature from pre-industrial levels and possible collapse of many ecosystems. One industry to look at to decrease its carbon emissions as well as making it more environmentally friendly is the catalyst industry which currently makes up approximately 8% of the global carbon footprint ¹. This is likely to increase as the market for metal catalyst is expected to grow from 2022 to 2031 at a CARG (compound annual growth rate) of 4.5% ², this will lead to more CO₂ produced. You may wonder why catalysis is such an important industry to reduce its carbon emissions this is because of its critical role in modern industry as over 80% of all manufactured products involve a catalyst. As well in the production of industrial chemicals that the world produces approximately 90% use a catalyst ³.

Although in recent years there has been a major shift into the development of green and sustainable chemistry, opposed to the continuous development of catalysts for upgrading crude oil derived components. This includes the use of bio renewable feedstock materials derived from lignocellulosic biomass, specifically second-generation sources. First generation biomass pertains to food components and has sparked the food vs fuel debate, a long-standing issue where food crops have been directly converted into fuel sources (mostly bioethanol) opposed to being harvested for feeding the people ⁴. Topical in the United States of America (USA), bushels of corn are frequently used for the production of petrol additives through fermentation. Second generation waste streams are those that can be part of the food processing industry but are not directly involved with food, i.e, branches, stems, leaves, husks, shells, seeds, straws, pulps and woodchips ^{5 6}. Lignocellulose itself pertains to three core organic components, lignin, cellulose and hemicellulose ⁷. Cellulose and hemicellulose are polymeric sugar systems that are physically supported by the lignin backbone for rigidity. Cellulose is comprised of hexose (monosaccharides with six carbon atoms) and hemicellulose is built from pentose (monosaccharides with five carbon atoms). Sugar in waste streams hold substantial value, be

that through the classical fermentation to bioethanol shown for first generation fuels, or through the production of bio-oils by utilising pyrolysis, possibly the future of all green and sustainable chemistry as bio-oils are rich mixtures of organic components that can be directly upgraded catalytically and, in some cases, used as ‘drop in’ fuels. However, bio-oils are acidic and often seen as arduous to separate, therefore the accommodation of bio-oils into the bio-economy is not fully integrated, yet.

1.1 What is a catalyst?

We can define a catalyst as a substance that increases the rate of reaction without itself being consumed in the process ⁸. The way it does this is by lowering the activation energy this is done by either providing a different mechanism for the reaction to take at a lower activation energy or by providing a surface and orientation this means that they are in close proximity to the reagent and can bring them in at the right orientation ⁹. The activation energy diagram in **Figure 1** shows the required energy for a chemical reaction to take place is substantially lower when in the presence of a catalyst.

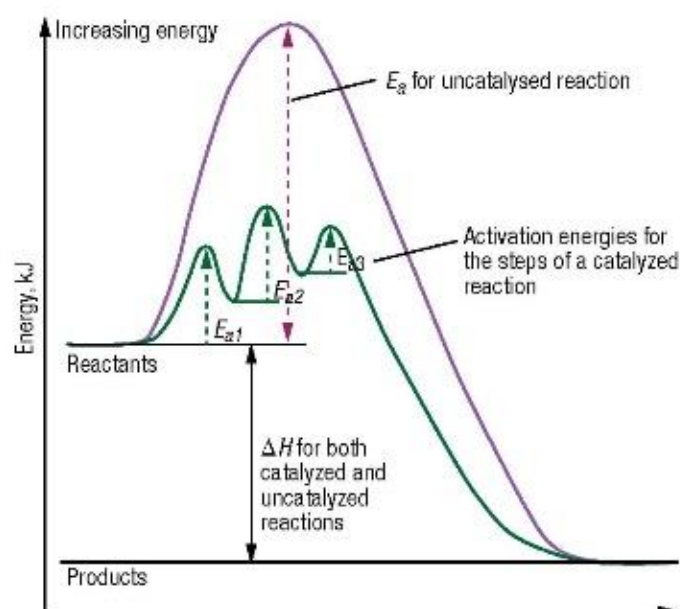


Figure 1: Figure 1: Activation energy diagram for a catalyzed and non-catalysed reaction (Modified from <https://www.chemengonline.com/catalysis-fundamentals/>)

Catalyst selectivity refers to the direction of a chemical reactions towards its products, where optimised catalytic reactions strive to minimise the undesired by-products in favour of increase the yield of the desired product. It is believed that selectivity is the most critical aspect to catalysis, controllable chemical reactions with favourable products formed over side reactions. Activity itself, although a driving force in catalyst selection is overcome by the notion that one can simply add more catalyst (decrease the reactant: catalyst ratio). By providing more reaction active sites, the rate of reaction can be increased and ultimately increase product yield. Alternatively, modify the reaction conditions to boost activity, although at a risk to the selectivity and therefore can be sometimes considered counter intuitive if the reaction has already been optimised.

Catalysts can be broken down into two categories, that being homogeneous and heterogeneous. These categories refer to what the what phase the catalyst and reaction are in. Homogeneous catalysis takes place when the catalyst and the reactants are in the same phase e.g., both are a liquid or gas. Whereas heterogeneous catalysis is where the catalyst and the reactants are in a different phase, an example your catalyst could be a solid and your reactants are either in a liquid or gaseous form.

For heterogeneous catalysts support materials are critical, a platform for an active nanoparticle to be embedded and be used for a chemical reaction, either through the adsorption onto the surface or a porous material where diffusion will allow mass transfer to occur. Support materials as they have been investigated overtime have been found to play a critical role in nanoparticle stability. This can include limiting/preventing particle sintering and agglomeration, it can also aid in catalytic promotion where electrons are able to be donated and or move, protecting an active site from oxidation or poisoning. This being said, the classical supports; Al_2O_3 , TiO_2 , Fe_2O_3 , MgO , CeO_2 , SiO_2 , activated carbon, ZnO and CaCO_3 ^{10, 11 12 13}, with the exception of activated carbon (depending on how it is produced) is the subject of large

scale quarrying and as a result, substantial carbon emissions. This diminishes the shine catalysts have on reducing net emissions through their own heavy ancestral carbon footprint. A modern-day solution to this problem is the use of lignin derived biochars, a CO₂ neutral option for supporting heterogenous catalysts.

Table 1 shows that with regards to homogeneous catalysts, they can be more selective for specific reactions and can exhibit increased activity due to the accessibility to the metal centre which is the active site. As a result, they are not restricted by mass transfer limitations. However, this comes with the restrictions in the applications the catalyst can be used in, as well as a difficulty in the catalyst separation process making it tedious and expensive as they are in the same phase. Therefore, this can add a high cost to the chemical reaction due to the high loss of the catalyst. In comparison heterogeneous catalysts can be less selective and provide lower activity due to cases of severe mass transfer limitations. However, as a positive these catalysts are easily separated or removed from reactors, and apart from the use of precious metals (Pt, Pd, Au or Rh), can be considered cheaper options than homogeneous catalysts. Additionally, they require less solvents with considered in the liquid phase, while directly applicable for gas phase and plasma-based reactions, unlike homogeneous catalysts. The best-known catalyst examples for this are the catalytic convertor for the internal combustion engine or to produce ammonia through the Haber-Bosch process. The method of homogeneous catalysed hydrogenation is important because it is used to produce both fine and bulk chemicals on an industrial scale ^{14, 15}.

Table 1: Comparison between Homogeneous and Heterogeneous Catalysis ¹⁶.

	Homogeneous	Heterogeneous
Active Centres	All Atomic at the centre of organic linkers (organometallic)	Only on the surface of a support
Selectivity	High	Tuneable
Mass Transfer Limitations	Very rare	Can be severe
Structure/Mech	Defined	Undefined
Catalyst Separation	Tedious/Expensive (extraction or distillation)	Easy
Applicability	Limited	Wide
Cost of Catalyst Losses	High	Low

The most famous of these is the Haber-Bosch process which use an unsupported Fe catalyst (iron mesh with a ~10% potassium promotor) for the production of ammonia as well as a Ni catalyst for the production of margarine, also known as saturating fatty acids. Hydrogenation is a chemical reaction with molecular hydrogen (H_2) that has dissociated on the surface of a metal nanoparticle. Depending on the metal used the required hydrogen dissociation energy can be varied. Pd is used because H_2 can easily dissociate on its surface ¹⁷. The adsorbed hydrogen will then react with organic molecules that have also adsorbed onto the surface of the metal active site or support. Here, bond saturation can take place where $C=C$, $C\equiv C$ and or $C=O$ as examples can be 'hydrogenated' to $C-C$, $C=C$ ($C-C$) and $C-OH$, respectively ¹⁰⁻¹². Typical metals used for heterogenous catalysed hydrogenation reactions are iridium, nickel, palladium, platinum, rhodium, and ruthenium ¹⁸. However, copper is also considered but normally requires

a pressurized environment (high required hydrogen dissociation energy)¹⁹. For the example in **Figure 2**, hydrogenating hexadiene to hexane increases the boiling point of the chemical and subtly its molecular mass. By altering the structure through bond saturation, the applications of the chemical are radically altered. For hexadiene, its primary application is as a cross linker to produce larger molecules. However, hexane is primarily used as a solvent that can be used to as a cleaning agent, medium to extract oils and other chemicals from solids, it is also used in the fragrances and flavourings sector²⁰. Modifying oxygenates will lead to different molecule functionalities which also drives different chemical applications.

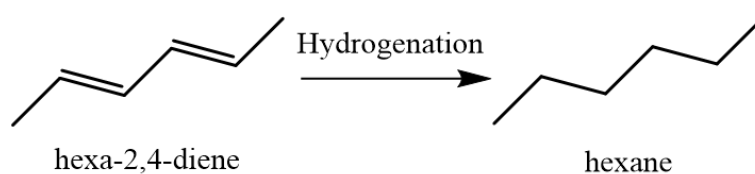


Figure 2: Example reaction of hydrogenation.

1.2 What is Biochar?

Humans have been making a form of biochar for >38000 years in the form of charcoal, using it as a pigment and then later for the production of steel to be used for building, followed rapidly afterwards for warfare²¹. Biochar can be described as a carbon rich charcoal like substance, derived as a by-product following the thermal treatment of biomass or organic materials in an oxygen-depleted or oxygen-limited environment²². One of the thermal treatments used to create biochar is pyrolysis. Which is defined as the process of decomposing biomass or organic materials thermally in an oxygen free environment at a range of temperatures from 300-900 °C²³. Pyrolysis can be further broken down into three sub types these being slow, fast, and flash pyrolysis. the by-products that are made from the process are biochar, bio-oil, and syngas. Slow pyrolysis as the name suggest is the slowest of the three types of pyrolysis with its time frame measuring form minutes to days as well as the temperature being on the low side usually not exceeding 500 °C with a low heating rate of anywhere from 0.1-2.0 °C, the relatively low

temperature promotes the production of biochar and tar ²⁴. Now, we jump to the opposite end of the spectrum to flash pyrolysis. This form of pyrolysis temperature usually ranges from 400-600 °C but may go as high as 1000 °C ²⁴. What gives flash pyrolysis its name is its fast-heating rates that may reach as high as 2500 °C per second. this flash heating rate and low retention time of less than 0.5 seconds leads to the major product components being bio-oil. Now that we have mentioned both ends of the spectrum, we can look at the final type which is fast pyrolysis which has a close relation to fast pyrolysis. whereas in flash pyrolysis the heating rate may reach 2500 °C per second in fast pyrolysis the heating rate is 10-200 °C per second with a short residence time of 0.5-10.0 seconds this results in the promotion of the syngas and bio-oil over biochar ^{24, 25}, an overview of this section is illustrated in **Table 2**.

Table 2: Comparison of all parameters for slow, fast, and Flash Pyrolysis

Pyrolysis Type	Temperature (°C)	Heating rate	Major Products
Slow	500	0.1-2.0 °C per min	Biochar & Tar
Fast	400-1000	10-200 °C per second	Syngas & Bio-oils
Flash	2500	2500 °C per second	Bio-oil

Bio-oils themselves are a source of sustainable chemicals, often referred to an “oxygenate soup”. This naming is due to the rich supply of oxygen containing chemicals (acids, alcohols, aldehydes, ketones or esters ²⁶) often present, although oxygen containing compounds are not exclusive to bio-oil. There are often short/long chained hydrocarbons as well as other aromatic and branched molecules ²⁷. Bio-oil is a viscous substance that is highly acidic ²⁸, and its chemical composition is variable depending on the feedstock used, prior thermochemical pre-treatment and the method of fast pyrolysis such as the presence of a catalyst ²⁹. Often a catalyst is placed in the path of pyrolysis vapours to prevent coking and rapid deactivation, here cracking reactions can take place or chemical transformations if there is a source of hydrogen in the stream. Already operating at scale there is an industrial presence of liquid fuel production

through the catalytic pyrolysis of various feedstocks, be that plastics, waste tyres or other bio renewable materials ^{30, 31}.

1.2.1 Uses of Biochar

Biochar is used in a wide array of industries such as the farming sector/land remediation, gardening (commercial soil additive), building sector, fluid decontamination, biogas production, medicine and textiles ³². It can also be used in the sequestration of additional carbon, as well as in the industrial sector in support for catalysis ³³.

For the farming sector improving poor quality soil can allow them to grow more crops. This can be achieved by soil amendment. With the addition of biochar, it has been shown that it reduces the density and stiffness of the soil allowing for a reduction of fuel need in the soils development for agricultural uses ³⁴. Another benefit for the addition of biochar to soil is once added it has been shown to improve both the air and water management of the soil ³⁵. This improvement to the water management mean that the soil now has its ability to retain an increased amount of water as well as decreasing the amount lost to evaporation ^{36 37}. With the addition of biochar, the overall colour of the soil becomes darker which has been noted to increase the soil's temperature by about 0.5 °C which may accelerate germination ^{38 39}.

For fluid decontamination biochar has been used as an adsorbent due to the fact it is very easy to tailor it to the desired pollutant, due to the ease at which it can be functionalized as well as its overall porous nature with a controllable specific surface area ^{40, 41}. This enables the biochar to be used on the removal of pollutants form the air as well as water. As we can see in **Figure 3a** there are a few ways that have been proposed for the mechanism for the interaction with heavy metals. With electrostatic attractions, ion-exchange and surface complexation being used by the abundant surface based functional groups such as carboxylic acid (-COOH) and hydroxyls (-OH). **Figure 3a** and **Figure 3b** both show that the electrostatic adsorption-

desorption processes are pH responsive. This means that increased adsorption to the surface can be promoted by either a low or high pH, where the release (desorption) would be facilitated using the counter pH. This phenomenon is also mimicked for metal uptake when utilising biochars for environmental remediation, the negatively charged surface will attract metal ions at different rates, subject to the solution pH. Biochar can also undergo direct physical adsorption through impregnation routes (**Figure 3a**), this is also shown by the pore filling mechanism (**Figure 3b**) which is possible if the biochar used is activated and possesses a pore network. Albeit, pores can be functionalised similarly to a surface where functional groups can regulate adsorption through variation to the pH. Again, much like a standard surface, a pore network can contain a hydrophobic component which will improve uptake processes by preventing water adsorption, therefore prevent competition.

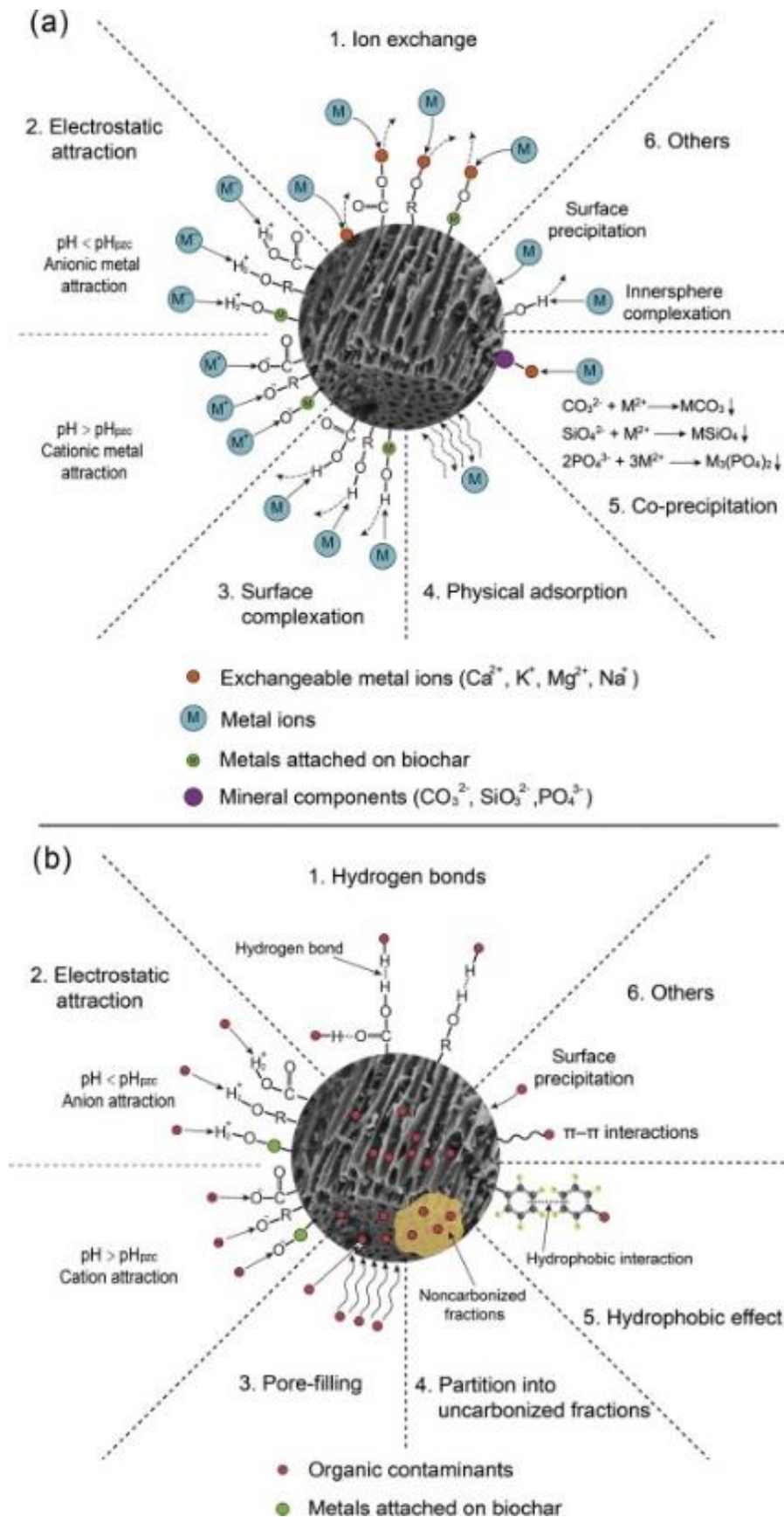


Figure 3: Methods by which biochar can be applied to pollution remediation for (a) metal extraction and (b) organic contamination (modified from reference 42)

For the building sector the reduction of CO₂ emissions is a must as one of the main materials used in construction concrete. This accounts for ~8% of worldwide CO₂ emissions⁴³. One method of decarbonising the concrete industry is through the use of bio-based materials in the production of vital carbonate materials. Biochar has been looked at as one of these bio-based additives and reports suggest a positive effect on the mechanical, thermal and physical properties of the cement⁴⁴. As a result, diversifying supply chains and product lines, depending on the end point concrete application. The uses of biochar in the medical field are being steadily developed and mostly in their infancy. Albeit lignocellulosic biomass derived materials are well known in the drug delivery such as sporopollenin, a porous waste derived material⁴⁵. It is also worth noting that bio-based materials can be used in the human body as it has been shown to be both biocompatible and have a low cytotoxicity^{46,47}. For the use in textile industry, it has been found that adding biochar to textiles will enable increased moisture transfer, as well as improving water vapour permeability making the item of clothing applicable for sportswear or work attire that can promote perspiration⁴⁸.

Another application for biochar is in the sequestration of carbon. It is estimated that approximately 9.5 BT of carbon can be stored in soil by the year 2100⁴⁹. This has also been linked to physical carbon offset schemes where carbon credits are generated and can be allocated to industrial sectors. Here, through the carbon offset scheme, net emissions can be “cancelled out” or “offset” through the acquisition of stored carbon. This is where your net emissions sins can be absolved by appropriating solid carbon neutral materials^{50,51}. Although this concept is often considered to be a form of greenwashing, a rhetoric for doing no harm by effectively glossing over the heart of the problem by appearing to do something. By providing a company with a physical carbon entity, a monetary value can be applied where the carbon market itself can be massively volatile.

Biochar has itself in the past being used as a catalyst on its own. One such use is sulfonated biochar's in the production of biodiesel ⁵², sulfonated materials are classically regarded as solid acids and can facilitate transesterification reactions instead of using sacrificial acids (HCl or H₂SO₄) or bases (NaOH or KOH). Instead of acting as the catalyst the biochar can be used as a support medium for a catalytic metal site as a wide variety of catalyst have been employed in the literature for a variety of applications. These species include both monometallic and bimetallic alloys such as Ag/Fe, Fe/Pd, and Ni/Fe which have been used for the removal of carbon tetrachloride, nitrates and 1,2,4-trichlorobenzene in an aqueous system respectively ⁵³ ⁵⁴. A varied insight into how biochar supports have been used for various catalysis applications is shown in **Table 3**.

Table 3: Examples of how biochar can be used in catalysis.

Catalyst	Biochar	Application	Reference
NiCo/SDSW-ABC	Sargassum tenerrimum	Phenol hydrogenation	55
Ni/AC	Wheat straw	Hydrogen Production	56
(Fe(xwt%)/CBC) (Fe(xwt%)/CAC)	Chlorella vulgaris microalgae	Catalytic fast pyrolysis	57
σK/PB-T	Peat	Biodiesel Production (Transesterification)	58
Pt/BC	Maple	Furfural Hydrogenation	59
PdBCFe ₃ O ₄	Arabica coffee Straw	H ₂ O ₂ sensor	40
PC@CoFe PC@CoNi	Pinewood sticks	Tar reforming post pyrolysis	60
BWC/NiO-MoO 800	Wood chips	Biodiesel Production	61

		(Transesterification)	
Ru/N-ABC-X	<i>Pinus sylvestris</i>	Methanation	62
PRC/BMC, PRC/BTC	cotton linters	Electro-oxidation of methanol	63
RM-BC _(HP) , BC _(HP) , RM _(HP)	red mud and coconut shells	persulfate (PS) activator	64
BC@Ni/Fe	Biochar	remediation of decabromodiphenyl contaminated soil	65
Co/EAC	Macauba fruit	Biofuel production (deoxygenation)	66
Ni-char	Pine wood	Cracking of toluene	67
biochar-based solid acid catalyst	Corn stover	Chemical synthesis Hydrolysis	68
Sulfonated biochar	Wood chips and pelletized punt hulls	Hemicellulose Hydrolysis	69
SnO ₂ -Co ₃ O ₄ /C biochar	Hydrolyzed lignocellulose residues and sugars	Hydrolysis to get Furfural	70
Fluorine anion- containing ionic liquid modified biochar sulfonic acid	Bamboo powder	Hydrolysis of cellulose to furfural	71
CaO based biochar solid acid catalyst	Palm kernel shell	methanolysis reaction of sunflower	72

Sulfonated biochar	Wood chips	pre-esterification	73
Ni/AC	Cotton stalk	Hydrogen Production	56
MnACeO _x /biochar, MnACeO _x /biochar	Cotton stalk	NO oxidation	74
Biochar/TiO ₂	Corn cob	Photocatalytic degradation of sulfamethoxazole	75

1.2.2 Activated Carbon

Activated carbon is described as a predominantly amorphous solid carbon material with a highly developed internal surface area, amounting to high level of possible surface reactivity⁷⁶. The activation of carbon is done because it allows the carbon to be used in a wider verity of ways as the high surface area and porosity and surface functionality can be used⁷⁷. The highly porous nature makes it useful for the adsorption of both gases and solutes from aqueous solutions⁷⁸. As can be seen in **Table 4** as well as **Figure 4**, there are many uses for activated carbon. Activated carbons can be made from any sufficiently carbon rich feedstock such as first and second-generation biomass. The activation process can turn what would be a bulk material into a species that is highly porous with a large available surface area. The resulting material is referred to as activated carbon and has been readily commercialised. This process is carried out so that there is a greater available surface area, enabling the ability to act as a filter material, facilitating the surface adsorption of pollutants, be that in the liquid or gas phase. There are two major methods to produce activated carbons, these are through physical and chemical activation. Physical activation is carried out by adding hot gases after pyrolysis to develop the pore structure. These gases are usually CO₂, N₂, NH₃ O₂, air and steam but it can be a combination of the gases⁷⁹. The carbon activation temperature ranges used are between 700-

900 °C^{80 81}. Chemical activation is done before being thermally treated and involve the activating agent reacting with the biomass, by either oxidation or dehydration operating at much lower temperature than those for physical activation. Activating agents can be acids such as H₂SO₄, HCl, H₃PO₄ and HNO₃, as well as bases such as KOH and NaOH, as well as other oxidising agents such as H₂O₂ and KMnO₄^{82 79}.

Table 4: Examples of how Activated Carbon can be used in catalysis.

Feedstock	Application	Reference
Cherry stone	Absorbent	83
Municipal Waste	Removal of dioxins from incineration	84
Cane bagasse	Water Treatment	85
Norit RB3	CO ₂ adsorption	86
Norit® D10 activated carbon powder	Deoxygenation of fatty acids to diesel hydrocarbons	87-89
Wood char, Cellulose, pumping residues black liquid and fine cellulose sludge	Fuel Cells	90
Coal, Petroleum, Vegetable, Polymer	Gass separation and Storage	91
Coconut shells	Desalination	92
Eichhornia crassipes (common water hyacinth)	Supercapacitor	93
Rice Husk	Methanation	94

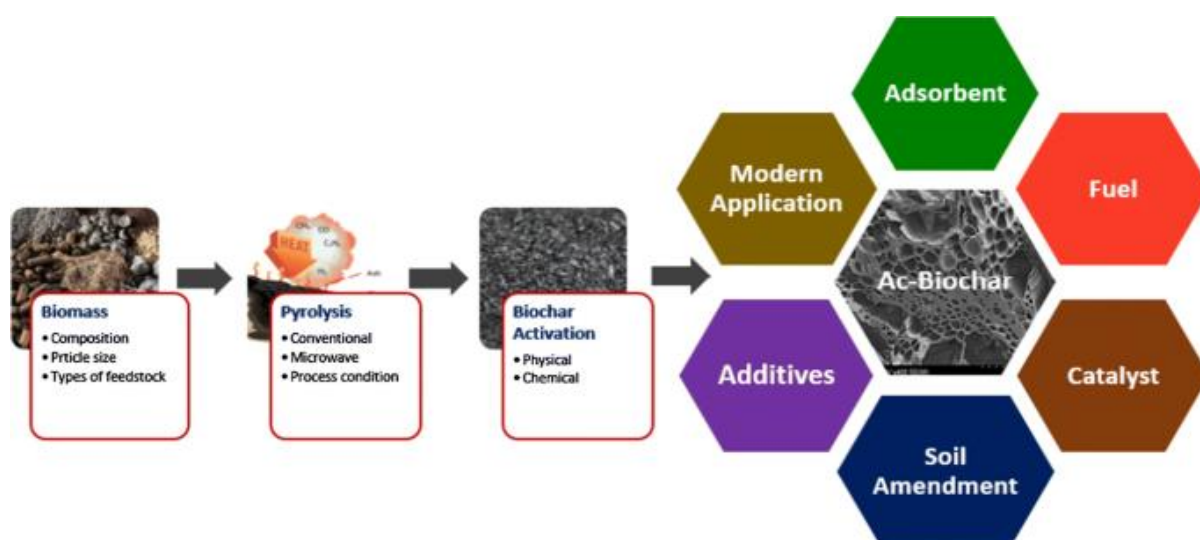


Figure 4: Uses of activated carbon ⁸⁰

1.3 Catalytic hydrogenation reactions

This thesis will detail the efficacy of biochar supported catalysts for the hydrogenation of a model compound. By using a sustainable catalyst support, initial steps can be taken to create a true circular economy, here waste resources can be repurposed and applied to green chemical synthesis. The initial question to ask is, what is hydrogenation? Hydrogenation is the method by which hydrogen (often in the gaseous form) is dissociated or otherwise known as activated, mentioned above. The hydrogen atoms are then able to directly react with π -bonds in chemical compounds, either resulting in the saturation of molecules (removal of all π systems) in favour of just σ -bonds, an example of molecule saturation is shown in **Figure 1**. By doping lignocellulosic biomass waste derived biochars with a low metal loading of a metal capable of facilitating hydrogen dissociation, catalytic turnover can take place and ideally tuned, depending on the quality and attributes of the biochar support.

1.4 The selective hydrogenation of phenylacetylene to styrene

The production of styrene is important as it used widely in the production of polystyrene, as well as synthetic rubbers like Acrylonitrile Butadiene Styrene (ABS) and Styrene-Butadiene (SBR) ⁹⁵. In 2021, the global market for styrene was at approximately 30 million tonnes which

is expected to grow at a Compounded Annual Growth Rate (CAGR) of 5.6% until 2030 ⁹⁶. The dominant method to produce styrene is through the dehydrogenation of ethylbenzene over an iron oxide catalyst ⁹⁷. A pure feedstock of styrene is vital as a specific impurity in the reaction, phenylacetylene. Phenylacetylene is a poison to the styrene polymerization catalyst causing it to deactivate ⁹⁸. As you can be seen in **Figure 5**, phenylacetylene can be partially (selectively) hydrogenated to styrene but will also over convert into ethylbenzene. As this reaction occurs under both mild temperatures as well as atmospheric pressure it makes this reaction a perfect probe reaction to test and optimise new catalysts ⁹⁸. Moreover, although styrene production is dominated by crude oil derivatives, phenylacetylene has been found to be waste derived, specifically in the tar fraction of municipal solid fractions post pyrolysis ⁹⁹. This adds greater value to the overall thesis as both the reaction and catalyst supports share a nexus, waste.

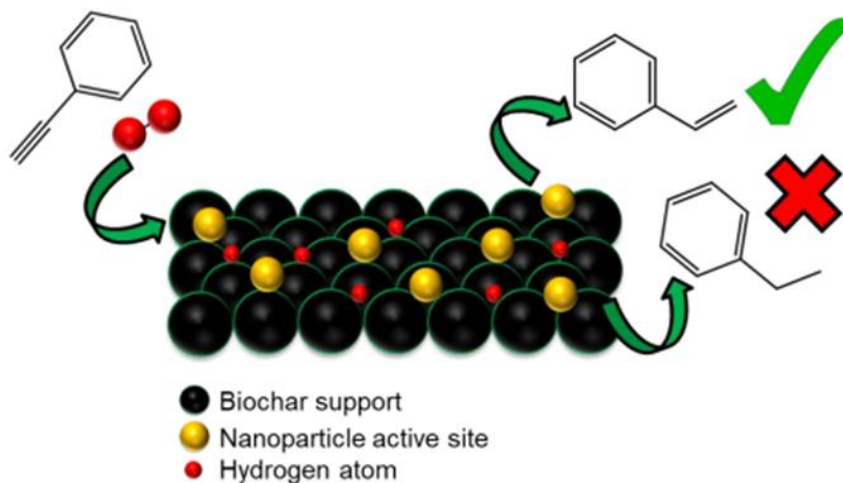


Figure 5: Reaction mechanism for the selective hydrogenation of phenylacetylene to styrene

From the literature we can see that there are three main metals that have been used for the selective hydrogenation of phenylacetylene; gold (Au), platinum (Pt) and palladium (Pd) ¹⁰⁰ ¹⁰¹. A range of other catalysts, their reaction conditions, hydrogen species used (molecular or transfer through solvent) are listed in **Table 5**. Other metals have also been used in the selective

hydrogenation of phenylacetylene such as platinum (Pt), gold (Au), copper (Cu) as well as examples of bimetallic alloys such as NiZn₃ and PtCu. These metal configurations have been seen to be supported on Al₂O₃, carbon, modified mesoporous silica (SBA-15) and complex supports such as layered double hydroxides (LDH), utilising both molecular hydrogen and hydrogen donors ^{102 103 104}.

Table 5: Previous catalytic packages used for phenylacetylene hydrogenation.

Catalyst	Reaction conditions	Hydrogen species	Selectivity	Reference
Pt/ α -Al ₂ O ₃	T = 30-90 °C P = 0.129-0.618 MPa	H ₂	50-66 %	105
Au/Al ₂ O ₃	T = 80 °C P = 1.5 × 10 ⁻³ – 0.88 atm	H ₂	100 %	106
NiZn ₃ /AlSBA-15	T = 40 °C P = 0.1 MPa	H ₂	90%	107
PtCu/C	T = 35 °C P = 6 MPa	H ₂	94 %	108
Zn-Ti LDH	T = 45 °C P = Atmospheric	H ₂	90 %	102
Pd–Ag/ZnO	T = 40 °C P = Atmospheric	H ₂	88 %	109
[Pd(2-pymo) ₂] _n	T = 45 °C P = Atmospheric	NH ₃ BH ₃	100 %	110
Pd–Cu/Al ₂ O ₃	T = 40 °C	H ₂	71 %	103
Pd–Zn/Al ₂ O ₃	P = 0.1 MPa		82 %	

Cr/3Pd/SiO ₂	T =20-45 °C P = Atmospheric	H ₂	72-97 %	111
-------------------------	--------------------------------	----------------	---------	-----

T= Temperature, P = pressure

The catalytic package that has dominated selective hydrogenation of alkynes is the Lindlar catalyst¹¹²⁻¹¹⁴. This material contains ~5 wt.% Pd supported on porous calcium carbonate that has been treated with different forms of lead and quinoline to enable a self-poisoning or terminating material, preventing/limiting over conversion¹¹⁵. This catalyst is a problem due to the relatively high amounts of Pd used, as well as the need to use lead and quinoline¹¹⁶. On a sustainability angle this catalyst is not appropriate, the excessively high Pd content is both costly and a waste, compared with other catalysts now shown in the literature. Additionally, upon disposal of the spent catalyst, one needs to be mindful on the appropriate handling of lead due to its toxicity, especially in water. The Lindlar catalyst cannot be considered a State Of The Art (SOTA) due to being developed in 1966, catalyst innovation and advancement has gone through several renaissances in the past 57 years, especially for selective hydrogenation reactions. This includes the development of single atom catalysts, single atom alloys and bimetallic nanoparticles that can modify reaction selectivity by changing molecular adsorption^{10, 12, 117, 118}. By doing so, one can often omit the use of additives that can be used as a catalyst poison and prevent the risk of leaching into the reaction. Leaching is where metals will release from their support and enter the liquid phase with the reaction. As a result, lower the overall activity of the reaction. For the case of phenylacetylene, this is a flat molecule but once converted to styrene, the produced alkene has a bent conformation. This means that it can align end-on to the catalyst surface, as a result making the over conversion very favourable to ethylbenzene, this concept is shown in **Figure 6**. The ability to align end-on, although a problem for this work as ethylbenzene production would be favoured, the overall aromatic ring structure is preserved. This means that the molecular adsorption benefits selectivity by

preventing “deep” hydrogenation and therefore the production of vinylcyclohexane (ring hydrogenation only) or ethylcyclohexane (complete hydrogenation).

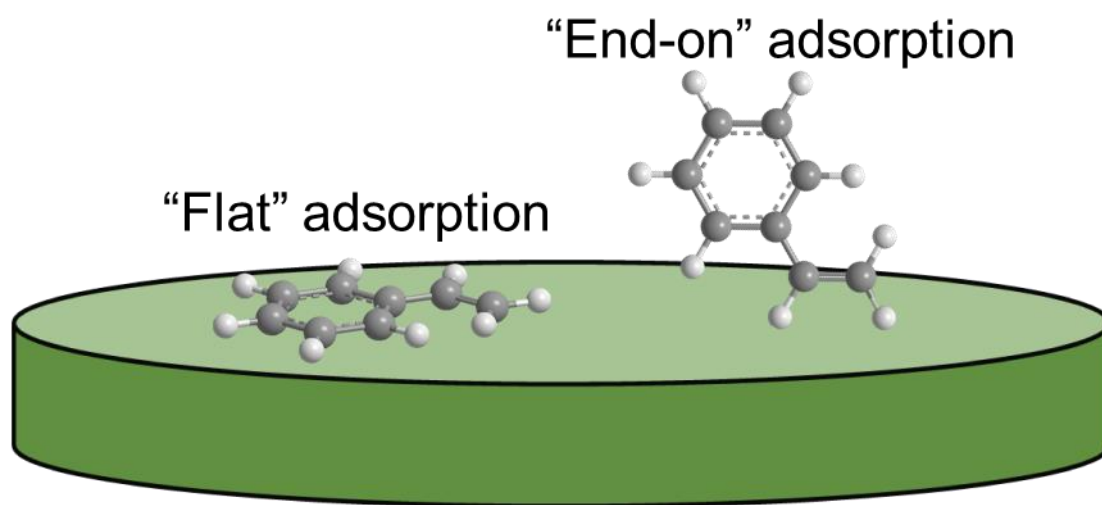


Figure 6: Possible surface adsorption profiles of styrene on a catalyst surface.

1.5 Aims and Objectives

In this work I will assess the effect of biochar support on dispersed Pd nanoparticles for the selective hydrogenation of phenylacetylene using molecular hydrogen. This will investigate the effect of pyrolysis temperature on the physical and surface chemical structure of the biochar, as well as biochar activation to probe whether a mesoporous biochar is more effective than a bulk material. In each case, evaluate the reaction selectivity for a ~1 wt% Pd/biochar catalyst. The wider literature on the proposed reaction is dominated by MO_x support materials which are considered as “high carbon”, this is due to their production from quarry sites being carbon intensive. Therefore, the use of “low carbon” supports in the form of biochars (derived from barley straw waste) will be investigated for their role in the selective hydrogenation of phenylacetylene when impregnated with Pd nanoparticles. Palladium has already been shown in the past to be effective for this reaction (**Table 5**), both in a monometallic and bimetallic form. This being said, the literature generally only considers carbon support materials in the form of “activated carbons”, which possess a fossil fuel background and for the case of the

reference shown, this utilises high hydrogen pressure to conduct the reaction. This work will target the clear gaps in the literature to determine the following:

- Can a biomass derived biochar be used as an effective catalyst support of the selective hydrogenation of an alkyne?
 - Can a Pd/biochar catalyst operate this reaction under ambient hydrogen pressure and mild temperatures?
- Can the biochar support be tailored to benefit reaction selectivity?
- Can Pd particle size be regulated to ensure a monodisperse environment on a biochar?
- Can a biochar support be effectively compared with MO_x supports in the literature?
- Can bulk biochars be activated, does this structural alteration change reaction activity and selectivity?

Chapter 2

Experimental

2.0 Methodology

The production of Pd doped bulk and mesoporous biochars evolves from the initial, locally sourced barley straw feedstock. After initial feedstock pre-treatments, be that physical (milling) and physicochemical (leaching), where ash components are dissolved into solution and removed from the feedstock via diffusion. The resulting feedstock then takes two different routes, the first is straight to slow pyrolysis to generate a bulk biochar, the second involves an additional pre-treatment step involving sonication in potassium hydroxide followed by pyrolysis and post-processing to remove salt via reflux in acid (activation). The formed F biochars were then impregnated with palladium (II) acetylacetonate ($\text{Pd}(\text{acac})_2$) and annealed/reduced to generate a Pd^0 reaction site. A step-by-step method breakdown is listed below as well as a method flow chart in **Figure 7**.

2.1 Pre-Treatment of Barley Straw

The locally sourced barley straw was initially milled at 10000 RPM for 2 min using a Retsch GM200 Grindomix Knife Mill. The high RPM and time were chosen to acquire many particles of <0.25 mm (fine powder). The milled barley straw was then sieved for 5 min at 0.80 mm/g using a Retsch AS200 Vibratory Sieve Shaker, here all fractions were collected and stored in glass jars. By using the method mentioned, the <0.25 mm fraction was the major and preferred sample size produced. The reclaimed feedstock was then leached (water washed) in deionized water at 10 g/L for 4 h at room temperature. The leached material was separated using vacuum filtration and dried overnight at 105 °C in a Fisherbrand gravity conventional oven.

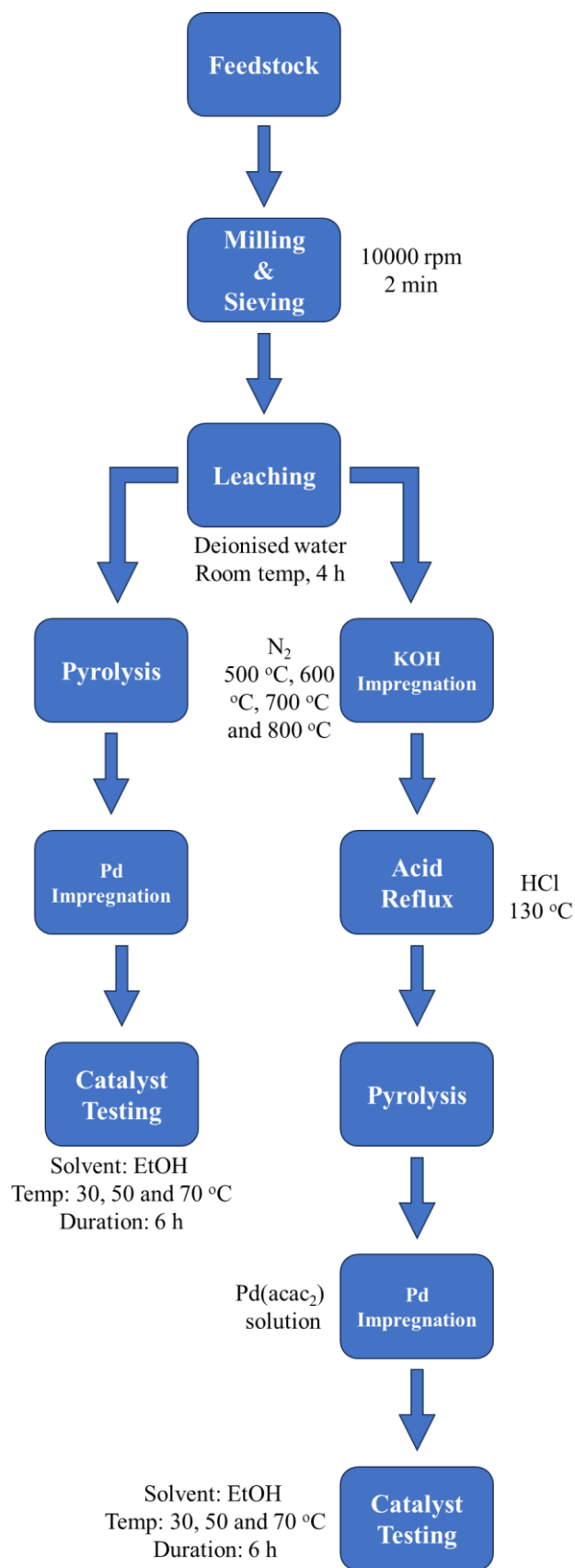


Figure 7: Graphical representation of overall bulk and mesoporous Pd/biochar methodology.

2.2 Slow Pyrolysis of Barley Straw

After the feedstock was dried, it was placed in two ceramic boats (2 g per boat). The filled boats were placed in a horizontal tube furnace for slow pyrolysis individually at 500 °C, 600 °C, 700 °C and 800 °C at a ramp rate of 5 °C/min, holding for 1 h under flowing nitrogen (~50 mL/min). Once cooled, the biochars were recovered and washed in ethanol (Fisher scientific \geq 99.8 %) and acetone (Fisher scientific \geq 99.8 %) until the washing ran clear, this was to remove traces of adsorbed tar and bio-oil, the biochar was then dried overnight at 105 °C in a Fisherbrand gravity conventional oven, once dried the biochar was ground to a fine powder in a mortar and pestle.

2.2.1 Biochar Derived Catalyst synthesis

Each of the produced biochars (~1 g) were immersed in 75 mL of water containing the 0.3g of Pd(acac)₂ (ALDRICH 99%) to achieve a 1 wt% loading of Pd/biochar. The suspension was mixed at 300 rpm for 3 h, covered, before heating at 80 °C to drive off the gradually overnight. Once dried the material were reclaimed and then transferred to a horizontal tube furnace to be annealed and reduced using a 10% H₂/N₂ flow at 500 °C for 3 h (3 °C/min). This created the following samples 1 wt% Pd/BC500, 1 wt% Pd/BC600, 1 wt% Pd/BC700 and 1 wt% Pd/BC800.

2.3 Mesoporous Biochar catalyst preparation & use

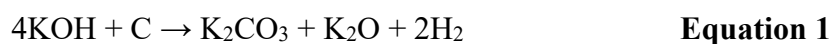
2.3.1 Mesoporous Honeycomb Biochar Production

The leached barley straw feedstock was introduced to a suspension of potassium hydroxide (KOH) at the mass ratios of 1:1, 1:0.5 and 1:0.25. So, for every 1 g of leached feedstock there was 1 g, 0.5 g and 0.25g of KOH in 100 mL of deionised water and these were sonicated in a Fisherbrand™ S-Series Heated Ultrasonic Cleaning Bath for 4 h at 50 °C. The materials were then heated to 80 °C while being mixed at 300 rpm overnight to drive off the deionised water,

forming a yellow/green biomass + KOH cake. This method was used as it follows typical synthesis routes to generate activated carbons at an industrial scale for commercial operations
119.

The biomass + KOH cake was then slowly pyrolyzed at 800 °C at a ramp rate of 5 °C/min and held at temperature for 1 h under flowing nitrogen (~50 mL/min). KOH is used because the metallic potassium (K) intercalation expands the carbon lattice in the biochar ¹²⁰. The KOH will also hydrolyse the sugars that are in the barley straw ¹²¹ Once cooled, the biochars were recovered and washed in ethanol and acetone to remove adsorbed tar and bio-oil, until the washing ran clear. The biochar was then dried for 1 h at 105 °C in a Fisherbrand gravity conventional oven. The dried biochars were then refluxed in 100 mL of 5 M hydrochloric acid (Fisher scientific S,G 1.18 ~37%) (HCl) for 3 h to digest the KOH and other trace metals naturally present in the biochar (ash). After refluxing, the materials were separated using vacuum filtration and washed with 500 mL deionised water to remove HCl residues, this was followed by drying overnight in a Fisherbrand gravity conventional oven at 105 °C.

Although there are many different chemicals that we can use for this process such as ZnCl₂, H₃PO₄, NaOH and KOH ⁸⁰. In this study KOH was chosen due to its availability, low toxicity in comparison to the others and the fact that metallic potassium intercalation expands the carbon lattice in the biochar. As KOH is a base, it will hydrolyse hemicellulose and cellulose, liberating hexose (C₆) and pentose (C₅) sugar units (**Equations 1-4**) this occurs before the sacrificial templating agent can be impregnated into the barley straw matrix and in this case that is the K⁺ ions. ^{122, 123}. Below are shown the activation mechanisms ¹²⁴.



Deep apertures were achieved by the etching of carbon atoms (**Equation 1** and **Equation 2**). The metallic K that is generated at temperatures $>600^\circ\text{C}$ within the matrix contributes to the expansion of the pores. The barley straw porous structure was further improved by the addition of the K_2CO_3 , while the barley straw was carbonised at higher temperatures this was produced as seen in **Equation 3**. **Equation 3** and **Equation 4** show that metallic K, K_2O , CO_2 and CO are formed as a result of the complete consumption of KOH, and the K_2O and K_2CO_3 that has been formed at temperatures $>700^\circ\text{C}$ where significantly reduced. As a result of refluxing with HCl, the metallic K residues were converted to KCl which is soluble in water, this was removed from the biochar matrix as well as other ash-based metals that can be present in barley straw such as Na, Mg and Ca ¹²⁴.

2.3.2 Mesoporous Honeycomb Biochar Derived Catalyst synthesis

Each of the produced activated biochars (~1 g) were immersed in 75 mL of water containing the required 0.3g of $\text{Pd}(\text{acac})_2$ (ALDRICH 99%) to achieve a 1 wt% loading of Pd supported on activated biochar (ABC), 1 wt% Pd/ABC. The suspensions were mixed at 300 rpm for 3 h, covered, before heating at 80°C to drive off the gradually overnight. Once dried, the materials were reclaimed and then transferred to a horizontal tube furnace to be annealed and reduced using a 10% H_2/N_2 flow at 500°C for 3 h ($3^\circ\text{C}/\text{min}$). This created the following samples 1 wt% Pd/ABC-1, 1 wt% Pd/ABC-0.5 and 1 wt% Pd/ABC-0.25.

2.4 Catalyst Testing

The selective hydrogenation of phenylacetylene was probed using the supported Pd bulk and activated biochar materials on a Radleys Starfish Parallel reactor platform (**Figure 8**). Solutions of 0.4 M phenylacetylene (Sigma Aldrich 98% pure) and 0.4 M of decane (Honeywell $\geq 99\%$, internal standard) in 25 mL of ethanol (Analytical grade, Fisher 99.8%) this was used as the physical reaction solvent throughout the work. These solutions were added to two-neck flasks containing 30 mg of catalyst and a hydrogen capillary feed line (PTFE) immersed into the reaction mixture. The hydrogen flow was set to 30 mL/min and the reactor was heated at 30 °C, 50 °C and 70 °C to investigate the activation energy for the reaction, per catalyst. Once at temperature the reaction mixtures initiated by magnetically stirred at 600 rpm, avoiding mass transfer limitations. The reaction was carried out at higher RPM and saw no beneficial improvements to the PA conversion. As a result and for limiting catalyst coming out of solution (moving up the flask), the stirring was ran at 600 rpm, although the hydrogen flow did cause minor agitation, no catalytic turnover was observed. Samples were removed at 0, 10, 20, 40, 60 min then at 1 h intervals until 6 h (0.5 mL), diluted in 0.5 mL ethanol and were filtered to remove the catalyst, the reactions where ran for six hours in total. The samples were collected and stored in a laboratory fridge before running on a LECO Agilent Technologies 7890A GC System for kinetic analysis (**Figure 9**). The reaction conversion and product selectivity where calculated using **Equation 5** and **Equation 6** for all reactions.

$$\text{Conversion} = \left(\frac{\text{Amount consumed}}{\text{Toal amount}} \right) \times 100 \quad \text{Equation 5}$$

$$\text{Selectivity} = \frac{\text{Concentration of product}}{\text{Phenylacetylene consumed concentration}} \quad \text{Equation 6}$$



Figure 8: Radleys Starfish parallel reactor platform operating the hydrogenation of four reactions simultaneously.



Figure 9: LECO-Agilent Technologies 7890A Gas Chromatograph with flame ionisation detector.

2.5 Instrumentation

2.5.1 Gas chromatography (GC-FID)

Gas chromatography (GC) is a common analytical technique that can be used to analysing compounds that can be vaporised without compromising their structure. As you can gather this is a form of chromatography which is a form of separating science. In this case it does it by separating a mixture into its constituent components by passing a sample through a column with an inert carrier gas which is either an inert or unreactive gas such as helium, nitrogen, or hydrogen. This separates the mixture because of the properties of the specific column causing each component to elute at a different time point. Once the sample has come off the column it goes to the detector in this case it is a flame ionization detector (FID). A hydrogen and oxygen flame are used to ionise the sample in the carrier gas as the gas is unaffected by the flame. The resulting ions from being ionised create an electric current that is amplified and sent to a computer the magnitude of the current is proportional to the amount of sample present. With this there are limits to how much can be detected and with FID that is the range of 0.1 to 100000 ppm.

A calibration was run for phenylacetylene, styrene and ethylbenzene with an internal standard of decane. five points were used to produce this calibration with concentrations of 2M, 1M, 0.5M, 0.25M and 0.125M this was done to determine the best method to use and where the reactant and products elute off the column. The 1 ml sample from the catalyst testing was run at an initial temperature of 90 °C then at 10 °C per minute the temperature is increased to 110 °C and held for 20 seconds after that at a rate of 2 °C per minute the temperature is increased to 115 °C per minute.

2.5.2 Fourier transform infrared spectroscopy (FTIR)

FTIR is a tool that allows us to investigate what functional groups are present on the surface of a sample, in this case biochar¹²⁵. Although infrared (IR) radiation does not have sufficient energy to physically move electrons to different energy levels, it can stimulate bond movement. This movement can be regarded as a combination of bond vibrations, angle bending/rocking and more complex movements. Specific bond movements generate unique IR spectra, many of these are characteristic for the compounds scanned and others can be ascribed to atmospheric effects such as a very broad -OH stretch at $\sim 3500\text{ cm}^{-1}$, this is characteristic of water. If a sample is not completely dry, this signal can be extremely dominant. Additionally, a peak at $\sim 2349\text{ cm}^{-1}$ is identified for atmospheric carbon dioxide and can generally be evidenced that an operator has been breathing on/near the sample holder. A full break down of all FTIR spectra obtained for the feedstocks and biochars are shown in **Chapter 3**. The FTIR was carried out to identify if leaching the feedstock would harm the structure of the feedstock as well as showing how or if the structure of the biochar is changed due to the different temperature it was pyrolysed at.

The FTIR spectra were acquired using Thermo Scientific Nicolet iS5 with a PIKE MIRacle single reflection horizontal ATR accessory. The instrument spectral resolution was set between 4000 cm^{-1} to 600 cm^{-1} , and the resolution was set to 4 cm^{-1} . A background reading of four scans was taken before the first run and after every three samples to eliminate a changing background environment.



Figure 10: Thermo Scientific Nicolet iS5 without the PIKE MIRacle single reflection horizontal ATR accessory.

2.5.3 Thermogravimetric analysis (TGA)

Thermogravimetric analysis (TGA) is used as it can provide both quantitative and qualitative data. It does this by recording the changes in the mass of a sample in percentage as a function of temperature and or time, in a controlled environment of either oxygen/air or inert gas. A TGA is used to determine the moisture, volatile components, its fixed carbon content and ash loading of a sample. The TGA of the raw and leached barley straw was carried out in triplicate using a large scale (~1 g) LECO TGA 701 using the following settings.

- The **moisture phase** starts at ambient temperature to 107 °C at 6 °C min⁻¹ and held for 15 min under a nitrogen atmosphere (10 L/min).
- After that the **volatile phase** takes place, this is where lids are placed on the crucible to protect the machine then it heats up from 107 °C to 950 °C at 5 °C min⁻¹ once at temperature it holds for 7 min under a nitrogen atmosphere (15 L/min).

- After this it cools from 950 °C to 600 °C. Once at 600 °C the instrument opens, and the lids are removed. The **ashing phase** takes place from 600 °C to 750 °C at 3 °C min⁻¹ under an air atmosphere to allow for combustion (10 L/min), there is no hold time, and the instrument will then cool slowly to room temperature.



Figure 11: Figure 10: LECO TGA 701 thermogravimetric analyser for multiple, large samples under parallel conditions.

Additional thermogravimetric analysis was carried out using a Mettler Toledo TGA/DSC 1 (~10 mg) in air at 30 mL/min, with a ramp rate of 10 °C/min from room temperature to 750 °C, holding for 1 h to monitor the ash content of the produced biochars, this instrument is shown in **Figure 11**.

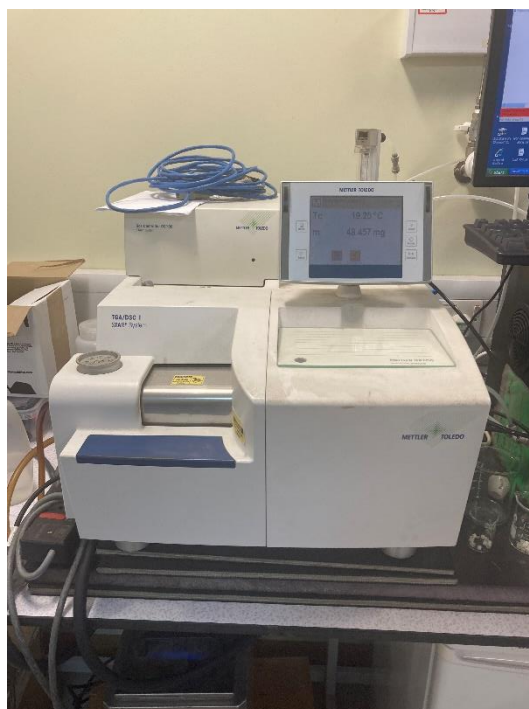


Figure 12: Mettler Toledo TGA/DSC 1 STAR system for small scale samples.

2.5.4 Ultimate Analysis

Ultimate Analysis is used to determine the carbon, nitrogen and hydrogen present in a sample, for all samples a Fisons Instruments EA 1108 CHNS elemental analyzer was used. Both feedstock and biochar samples were processed, approximately 2 mg of each sample was weighed into a tin cup. The cups were then compacted, making sure to remove as much air as possible (to eliminate nitrogen variation). The sample was then placed into the carousel where it drops into the ignition chamber which is at 950 °C, flushing with oxygen (99.9995%, Energas). The gases released from the combustion (CO, CO₂, H₂O, NO, N₂O and NO₂) were analyzed using both thermal conductivity and infrared detectors to determine the percentage of carbon, hydrogen and nitrogen in the sample. By utilizing the ash value found by TGA, one can estimate oxygen content of the samples by subtracting the C%, H%, N% and ash from 100.



Figure 13: Fisons Instruments EA 1108 CHNS elemental analyzer

2.5.5 Scanning Electron Microscopy (SEM)

Scanning electron microscopy is used to look at the surface topography and composition of a given sample in this work that is the Pd supported biochar. It does this by using a focused beam of electrons to scan the surface of the sample in a raster scan pattern. The electrons from the scanning will interact with the atoms and give off a range of signals that can be detected and this is what is used to identify surface topography and element composition.



Figure 14: Zeiss Evo 60 SEM with an Oxford instruments X-Max 80

2.5.5.1 Energy Dispersive X-ray Spectroscopy (EDX)

The monometallic biochar catalysts were analysed by using Energy Dispersive X-ray spectroscopy (EDX). An x-ray source is used to irradiate the sample causing photons to excite a core electron resulting in said electron being ejected from its shell. An electron from an outer shell fills the place of the missing excited electron. As this exchange of electrons occurs, the change in energy can be emitted as x-rays, the analyser can differentiate elements by the number and intensity of the emissions. The sample composition can be determined by integrating the relative intensity of the signal. EDX is a great tool to determine the atomic ratios in samples.

2.5.6 Transmission Electron Microscopy (TEM)

Samples were dispersed in methanol, deposited and sonicated on a 300-mesh carbon supported copper grid which was allowed to dry under ambient temperature. The dried grids were then imaged using a FEI Titan3 Themis 300: X-FEG 300 kV S/TEM with S-TWIN objective lens, monochromator (energy spread approx. 0.25 eV), multiple HAADF/ADF/BF STEM detectors,

FEI Super-X 4-detector EDX system, Gatan Quantum ER energy filter for EELS and EFTEM and Gatan On. Images were processed using ImageJ2 (Fiji) version 1.53 software, where particle size distributions were plotted using OriginPro.



**Figure 15: FEI Titan3 Themis 300 Transmission Electron Microscope
(University of Leeds)**

2.5.7 Brunauer–Emmett–Teller (BET) theory

Brunauer–Emmett–Teller (BET) theory is a method used to measure the surface area of porous or solid materials. It does this based on the adsorption isotherms of a non-reactive gas like nitrogen or argon, however, can also be carried out using mercury, in this case nitrogen was used across a range of pressures that covers the monolayer of the material. The obtained isotherms are transformed into the linearized BET plot (**Equation 7**), where the monolayer can be determined ¹²⁶. Approximately 0.05 g of each bulk and mesoporous biochar were de-gassed with a Micrometric FlowPrep 060 Sample Degas System under a nitrogen flow at 110 °C

for 3 h. After which a Micromeritics TriStar surface area and porosity analyzer (**Figure 16**) was used to determine the surface area, pore diameter and pore volume using nitrogen as the probing gas.

$$\frac{P}{V_a(P_0 - P)} = \frac{1}{V_m C} + \frac{C - 1}{V_m C} \left(\frac{P}{P_0} \right) \quad \text{Equation 7}$$

Where:

- P = pressure
- P₀ = saturation pressure
- V_a = volume adsorbed
- V_m = monolayer volume
- C = multilayer adsorption parameter



Figure 16: Micromeritics TriStar Surface Area and Porosity Analyzer with degassing station.

The physisorption of nitrogen is at 77.5 K, this allows the physical adsorption of nitrogen onto the surface in monolayers (single nitrogen molecules packed side by side), here the surface area measurements can take place. The monolayer coverage is then determined by calculating

how much N₂ has bonded to the surface. Relatively weak intermolecular forces known as Van der Waals forces are the cause of the interaction between the nitrogen molecules and the material. An assumed equilibrium between the adsorption and desorption is achieved by gradually increasing the pressure of nitrogen through the analysis. As this is done at low temperatures, the nitrogen molecules interact with other in leu of the adsorbate, this is called nitrogen multilayers.

The Langmuir theory has been modified slightly to allow the development of the theory of nitrogen physisorption. The modification to the Langmuir theory was because it did not account for the formation of N₂ multilayers so to account for the interaction between the N₂ layers a new constant was established C. The linear region of the BET plot is used to calculate the specific surface area, if we assume the packing between the nitrogen molecules is 0.162 nm², this indicates the monolayer coverage. By using **Equation 8 and Equation 9**, the parameters of the process can be expressed. Assuming the equal spacing between the nitrogen molecules we can determine the true surface area calculation and the multilayer interaction constant.

$$C \propto \exp \frac{E_1 - E_L}{RT} \qquad \text{Equation 8}$$

Where:

- C - multilayer adsorption parameter
- E₁ - the heat of adsorption for the first layer (kJ mol⁻¹)
- E_L - the heat of adsorption for the second subsequent N₂ layers (kJ mol⁻¹)
- R - Universal gas constant (8.314 J mol⁻¹ K⁻¹)
- T - Analysis temperature (K)

$$SA = \frac{V_m \sigma N_a}{mv}$$

Equation 9

Where:

- SA - BET specific surface area.
- V_m - monolayer volume
- Σ - N_2 packing value (0.162 nm²)
- N_a – Avogadro number (6.022×10^{23})
- T – Analysis temperature
- m – sample mass
- v - gas molar volume

2.5.8 Powder X-ray Diffraction (PXRD)

XRD is used to determine the crystallinity and structure of the sample in this case biochar. An advantage of using x-ray diffraction is it is seen as no-destructive technique for the analysis of samples meaning they can be recovered after being scanned they can be re-calmed and uses in catalysis or further characterisation can be carried out. Similarly, as to the previously mention EDX it involves photoemissions form the x-ray source which is from Cu radiation. X-rays are produced when an electron for a higher shell fills the hole that if left when the core electron level loses and electron. This radiation crated by this process is angled towards the sample through a monochromator. A smooth surface is essential for this to work so the sample must be ground into a fine powder. The powder will be a range of mesh sizes but to the naked eye the powder will seem to be of homogeneous size. Constructive interference with the incident rays is still possible as there will be a enough crystallites in the correct orientation meaning that the crystalline or amorphous material scanned due to the displayed diffraction pattern. We can understand constructive interference by using Bragg's law (**Equation 10**), where refraction

angles are observed only if the interplanar distance is equal an integer multiplied by the x-ray wavelength ¹²⁷.

$$n\lambda = 2d \sin \theta \quad \text{Equation 10 – Bragg's Law}$$

Where:

- λ is the wavelength of the x-ray source, in this case Cu radiation (0.154 nm).
- n is the multiplication integer (order of reflection).
- d is the interplanar distance.
- θ is the diffraction angle at which the peak is associated with.

The diffractogram is used to depict the nanoparticles if the loading of the active mental and crystallite size is high enough. From the reflection seen a miller index can be assigned, as well as using the Scherrer equation (**Equation 11**) to calculate an estimate for the crystallite size. The information this provides is useful because it can give an early indication into the particle size before using the more advanced method of Transmission Electron Microscopy. A limitation to the detection of crystallite occurs with relation to the crystallinity of the supporting material as well as if the particles present are ≤ 3 nm this will cause the peaks to lose its shape as well as broaden. This is due to the destructive interference limiting any constructive interference that leads to the peak. The way to resolve this problem is to monitor multiple crystal planes then averaging the crystallite size.

$$\tau = \frac{K\lambda}{\beta \cos \theta} \quad \text{Equation 11}$$

Where:

- t is the mean crystallite size.
- K is a dimensionless shape factor (0.89).
- λ is the wavelength of the radiation used (Cu - 0.154 nm).

- B is the Full Width at Half Maximum (FWHM) as calculated by the instrument or by manual integration.
- θ is the diffraction angle at which the peak to be measured is based



Figure 17: PANalytical Empyrean series 2 diffractometer.

Chapter 3

**The textural and
chemical properties
of bulk and
mesoporous biochars**

3.0 The textural and chemical properties of bulk and mesoporous biochars

In this section I will present and rationalise the results collected on the production and characterisation of both bulk and mesoporous biochars denoted in two sections as “batch char” which led to the naming of ‘BC’ and “activated biochar” which is mentioned as ‘ABC’, which are derived from barley straw waste. These materials were then impregnated with Pd to generate catalytic packages for the selective hydrogenation of phenylacetylene, the application of these functionalised biochars are shown in **Chapter 4**. The core aims of this research are as follows:

- Understand the effect of pyrolysis temperature on biochar structure, how this can be used to enhance or limit catalytic conversion.
- Produce a range of mesoporous biochars using chemical activation, determine the optimum process for synthesising high surface area carbon materials.
- Monitor the effect of biochar support on the produced Pd nanoparticles, are they stable?
- Assess the benefit of a mesoporous biochar catalyst on the phenylacetylene reaction. Is this a rational material to be used for a batch reactor or mass transfer limited?

3.1 Characterisation of Raw and Leached Barley Straw

3.1.1 Thermogravimetric Analysis (TGA)

Barley straw pre-treatment in the form of leaching was carried out, as described in **Chapter 2**. This is a type of physicochemical pre-treatment and is carried out to remove or reduce any water-soluble inorganic impurities in the barley straw^{128, 129}. As can be seen in **Table 6**, through TGA (proximate analysis) the leaching has significantly decreased the ash content from 3.50 wt% to 1.66 wt%, a reduction of 53%. This reduction in ash is most likely due to the removal of K, Cl and S (although S was not found to be present in the virgin feedstock), as leaching has been shown to reduce these elements over time, albeit K and Cl remove at a fast rate, S requires

a longer leaching residence time, as shown by Taylor et al. ^{130, 131}. The feedstocks in **Table 6** also show a moisture reduction of 69% between raw and leached barley straws which have 8.08 wt% and 2.55 wt% moisture, respectively. The drop-in moisture is due to that after leaching, the barley straw was dried overnight at 105 °C, where the raw barley straw was not. Note, there is still moisture present in the leached sample, this is assumed to be trapped within the lignocellulosic structure and could be due to a mild hygroscopic nature. It is postulated that this moisture can be removed through augmented drying technologies such as a vacuum oven. It is believed that the vacuum drying will not alter the internal structure, unlike pre-treatments that operate at pressure, followed by a rapid pressure drop such as CO₂ explosion or AFEX. Vacuum drying is not a sudden pressure drop, it is gradual. We can also see that the main component of the barley straw is its volatiles. As the barley straw is thermally degraded, it's volatile components in the organic sections are liberated. One can see that this value increases by ~10% after the barley straw has been leached. Increasing the carbon content through this pre-treatment is not possible, therefore it can be assumed that the decreases in both ash and moisture contribute to the rise in volatile value. Additionally, through decreases to both ash and moisture we can see that leaching has a beneficial effect on the higher heating value (HHV) as the value is increased by 6%. HHV, otherwise known as the gross calorific value, is the total amount of heat that can be produced from the feedstock when it is completely combusted. Although not in the scope of this thesis, it does show that leaching barley straw has a positive effect on barley straw being used for heating.

Table 6: Results from the Proximate analysis of raw and leached barley straw.

Sample	Ash (wt%)	Fixed Carbon (wt%)	Moisture (wt%)	Volatile (wt%)	HHV (MJ/Kg)
Raw <0.25 mm Barley Straw	3.50 ± 0.02	10.82 ± 0.34	8.08 ± 0.02	77.59 ± 0.34	15.90
Leached <0.25 mm Barley Straw	1.66 ± 0.02	9.77 ± 1.74	2.55 ± 0.15	86.02 ± 1.85	16.85

The thermogravimetric analysis curves can give insight into how the leaching pre-treatment has/has not affected the lignocellulosic structure. **Figure 18** and **Figure 19** show the mass loss of the feedstock with respect to temperature. **Figure 18** illustrates the thermal degradation pathway, showing a large difference between the raw and leached feedstocks, black and red lines, respectively, specifically the loss of mass as a function of temperature. Due to the leached barley straw being dried and the raw barley straw not, the former has significantly less moisture content than the raw barley straw (**Table 6**). This is shown by the larger initial curve from the raw barley straw, compared to the leached barley straw at 107 °C, this means that more mass has been lost in the sample through water removal¹³¹. The breakdown of hemicellulose and cellulose accounts for much of the volatile matter in barley straw as this feedstock has a relatively low amount of lignin in it¹³². It can be seen that the second mass loss for the leached barley straw is shown to thermally decompose at a higher temperature range of 240-400 °C compared to the raw barley straw 220-400 °C. The mass loss seen between the 600-1000 °C has been linked to the more complex lignin structure being thermally decomposed as it contains polymeric, aromatic rings and chains, causing this to thermally decompose over a wide range of temperatures¹³³.

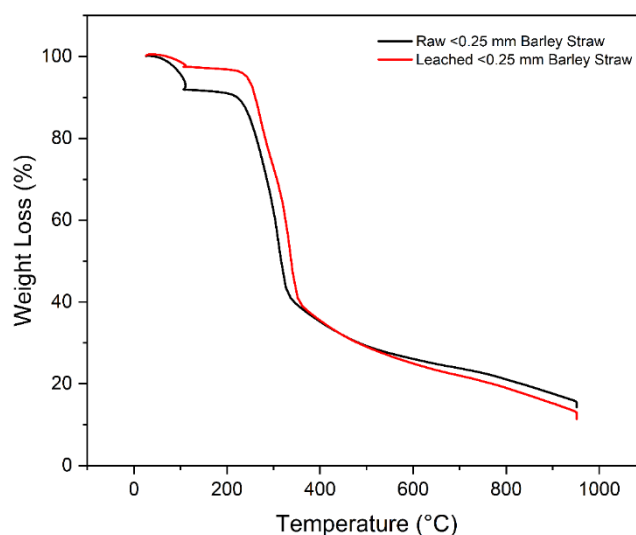


Figure 18 Weight loss curve for raw and leached barley straw

Figure 19 shows the derivative thermogravimetry, specifically the first derivative mass loss which presents the mass loss per minute, over time. We can see that the first peak on the graph is the mass loss of water, ranging from 35 °C to 107 °C. The next spike is a broad mass loss range from 200 °C to 500 °C. For the raw (black) we can only see one peak with a shoulder, after leaching we see that the shoulder has separated into a second peak. This shoulder is known to be due to be the depolymerization of the hemicellulose and pectin, followed by the main peak which is the degradation of cellulose ¹³⁴. We can also see that after leaching there is a shift in the main peak at 300 °C this shifting to lower temperature could be associated with the leaching process itself, this can disrupt hydrogen bonding (intermolecular interactions) which overall weaken the organic structure subtly. It is believed that this part of the “depolymerisation step”¹³⁵.

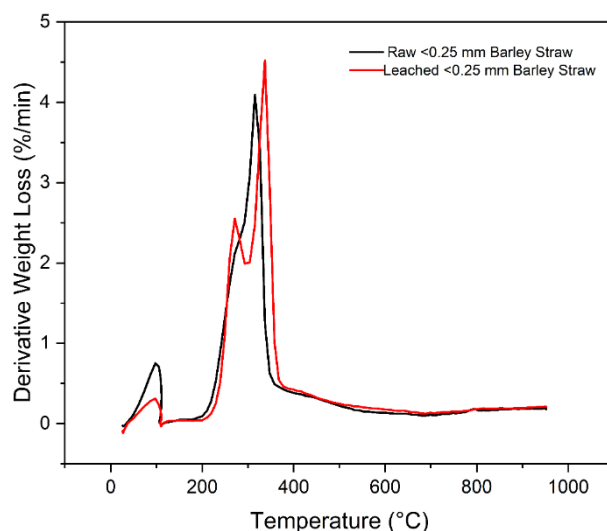


Figure 19: Derivative Weight Loss Graph for raw and leached barley straw

3.1.2 Ultimate analysis of raw and leached barley straw

Ultimate analysis was used to determine what affect leaching barley straw had on the organic content said barley straw. As we can see the from **Table 7**, as we leach feedstock the carbon and hydrogen is increased from 43.50 to 44.90 wt% and 6.35 to 6.41 wt%, respectively. The nitrogen decreased from, 0.52 to 0.30 wt% this is a decrease of 42%, this is a positive result as less nitrogen in the feedstock will result in less NO_x (NO, N₂O and NO₂) molecules been released during thermal processing, specifically gasification or combustion for energy, leading to a greener product, evidenced further by a substantial increase in C:N ratio, these data points are also in agreement with data published on similar samples ¹³⁵.

Table 7: Results from the Ultimate analysis of raw and leached barley straw.

Feedstock	C (wt%)	H (wt%)	N (wt%)	C/H	C/N
Raw <0.25 mm Barley Straw	43.50	6.35	0.52	6.85	83.65
Leached <0.25 mm Barley Straw	44.90	6.41	0.30	7.00	149.67

3.1.3 FTIR of raw and leached barley straw

FTIR was carried out to see how leaching barley straw effected its structure, as well as to see how the pyrolysis process changes the structure, in terms of chemical bonding opposed to

physical appearance. **Figure 20** shows that leaching has not changed the overall structure as the chemical stretches and bend are close to being identical between the two feedstocks, albeit with a slight decrease to moisture content shown at 3354 cm^{-1} (broad -OH stretch), agreed by the thermogravimetric analysis. Peaks that are indicative of cellulose and hemicellulose are; C-H stretching at 2883 cm^{-1} , C-H bending at 1368 cm^{-1} , C-OH bending at 1306 cm^{-1} , C-O-C asymmetry stretching at 1162 cm^{-1} and the C-O stretching at 1031 cm^{-1} . We can also see at 1731 cm^{-1} there is C=O stretching, which is expected from both hemicellulose and lignin. Another indication of lignin are the three peaks at 1616 cm^{-1} , 1506 cm^{-1} and 1426 cm^{-1} which are the aromatic skeletal vibrations in lignin ^{134, 136}.

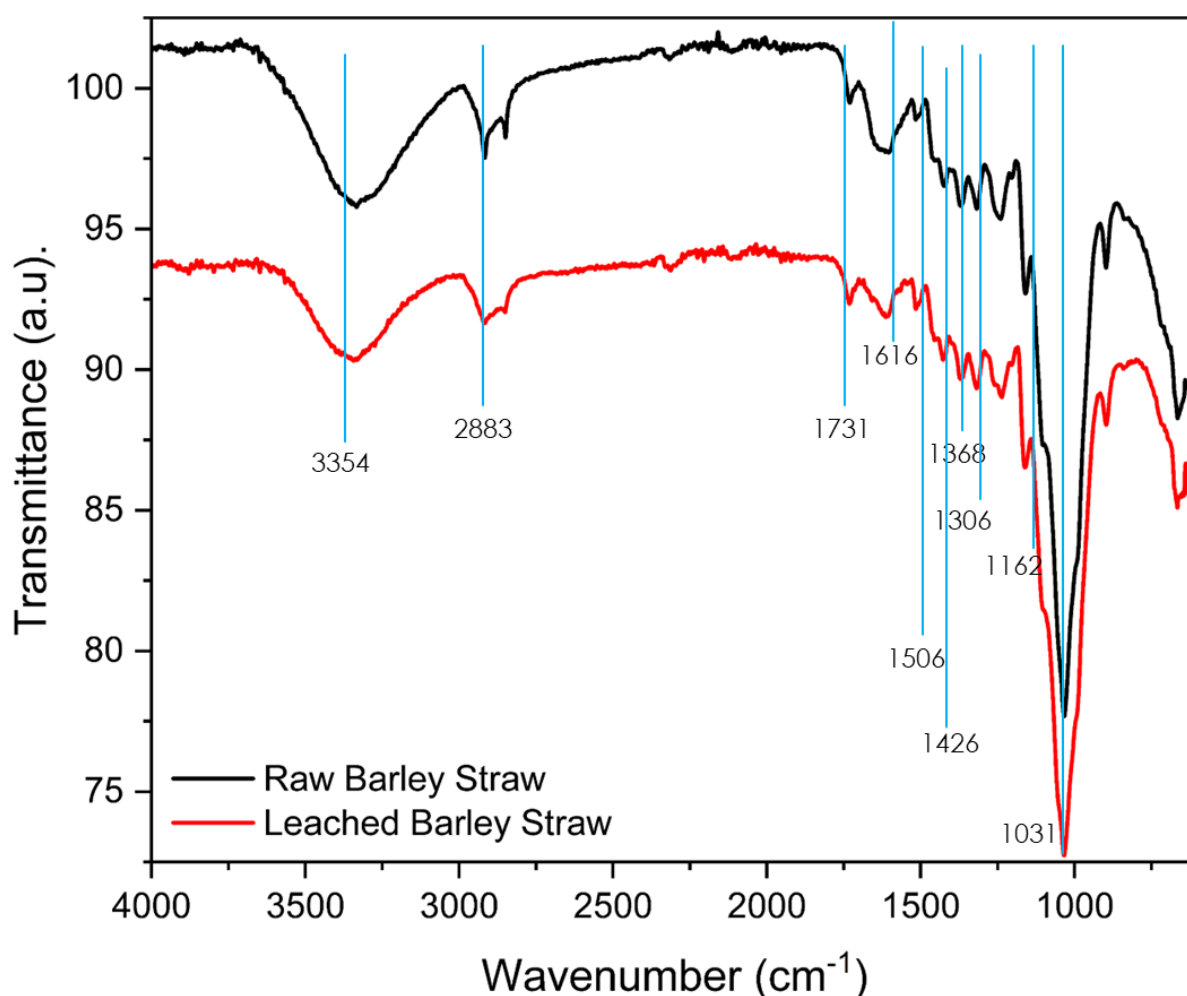


Figure 20: FTIR of raw and leached barley straw.

3.1.4 SEM of raw and leached barley straw

By using scanning electron microscopy (SEM) on both the raw and leached barley straw, we can investigate how the leaching process has changed the surface morphology. **Figure 21** is that of raw barley straw at a particle size of <0.25 mm at slightly varying magnification for **Figure 21a** and **Figure 21b**. Due to knife milling to reduce the parent feedstock size we can see the edges of the image are jagged and rough, we can also see a well-defined structure (no obvious deviations away from straw). For **Figure 22**, the feedstock imaged is post leaching, at similar magnification for both **Figure 22a** and **Figure 22b**. In the **Figure 22b** there is a yellow box showing that the previously well-defined structure has been softened somewhat after leaching. As well in **Figure 22b** there is a red box showing indentations into the barley straw, clearly caused through the leaching process, possibly through impaction due to the irregularity in spacing between the indents. The circular indents, were measured to have an average diameter of $10.49 \pm 2.75 \mu\text{m}$. The overall surface morphology for the leached barley straw compared to raw barley straw are not massively different. Other than from some mild fracturing and pitting that has been shown for previous images. The differences shown in images A and B for **Figure 22** are in different regions of the sample and therefore contains isolated regions of what appears to be delamination of the barley straw. Delamination could also be a function of the initial milling process and therefore could be present in the raw material ^{7, 131}.

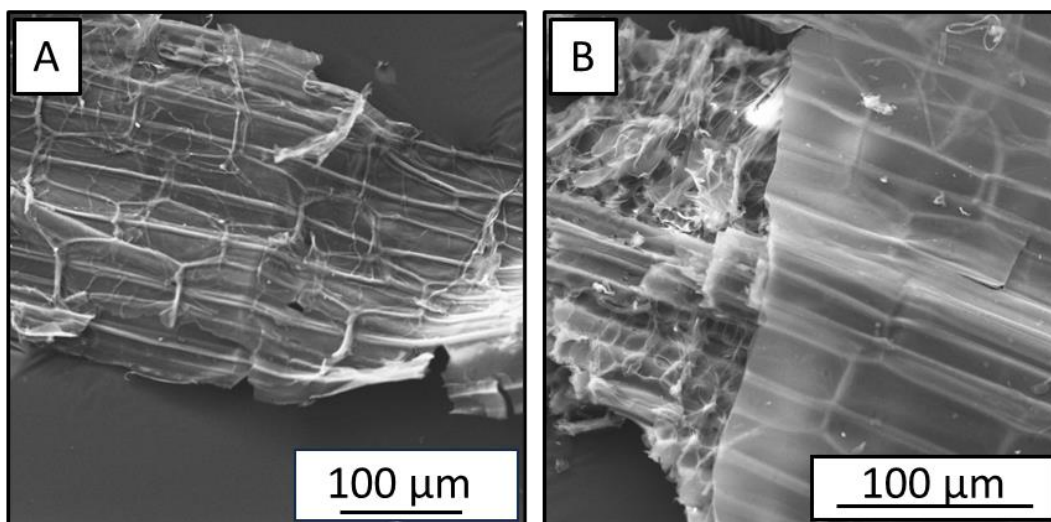


Figure 21: SEM of raw barley straw (0.25 mm grains), where A and B are at the same magnification but in different regions on the sample.

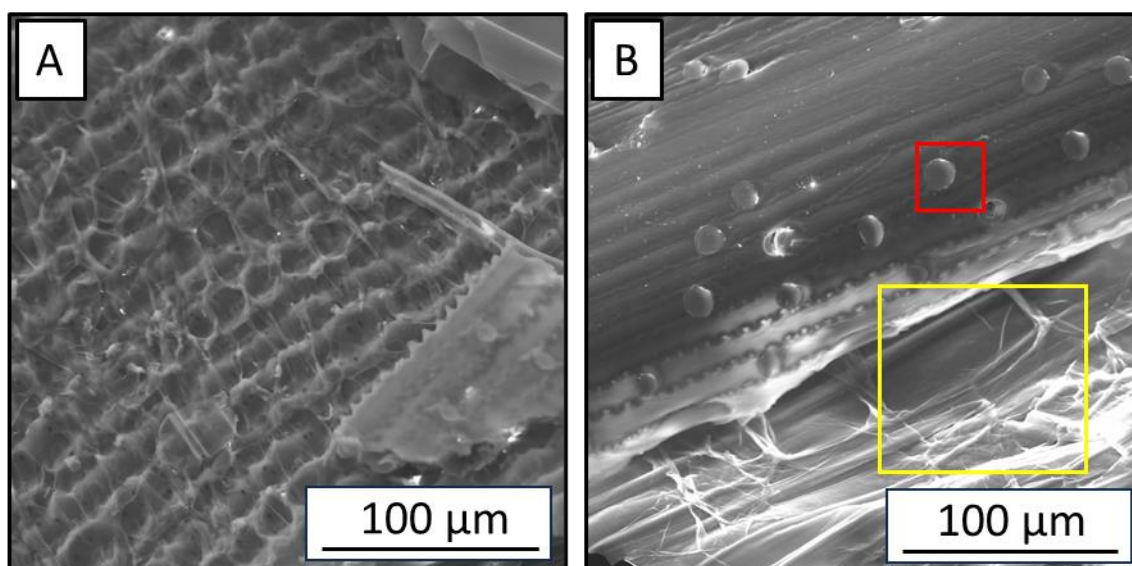


Figure 22: SEM image of leached barley straw, where A and B are at the same magnification but in different regions on the sample.

3.2 Characterisation of bulk biochars

As covered in **Chapter 2**, a family of bulk biochars were synthesised using four different maximum pyrolysis temperatures, 500 °C, 600 °C, 700 °C and 800 °C, with no other activation or post processing. After removing all surface bound oil and tar, the biochars were characterised using the techniques mentioned previously for the feedstocks, as well as porosimetry.

3.2.1 Thermogravimetric analysis of bulk biochars

Due to the low sample masses of the produced biochars, the LECO 701 TGA used for the raw feedstocks was not appropriate as the lowest mass for this TGA was 100 mg, using this size of sample would consume large amounts of product, especially due to triplicate analysis. Therefore, for all chars and Pd doped biochars, a Mettler Toledo TGA/DSC 1 STAR was used as it handles far lower sample masses (**Figure 11**). In comparison with the raw and leached barley straw in **Figure 18** that began breaking down at around 200 °C, we can see in **Figure 23** (biochar produced via pyrolysis at 800 °C) that the major ‘breakdown’ does not occur until 400 °C, that is an increase of 200 °C. This is due to the lack of volatiles present meaning in the material; therefore, it can be said that the bulk biochar 800 has become more thermally stable, especially as this TGA was carried out in air opposed to nitrogen for the raw feedstock. In nitrogen it was already shown to be thermally stable (the sample was not fully decomposed). We can see that combustion began at ~400 °C for this sample. Unfortunately, due to time and sample mass restraints, only the bare 800 °C could be characterised out of the bare bulk biochars as the other samples were impregnated with Pd for catalysis. Further biochars could have been made but would not be ‘identical’ as technically they would be from different batches, although we assume that the leached barley straw is homogenous.

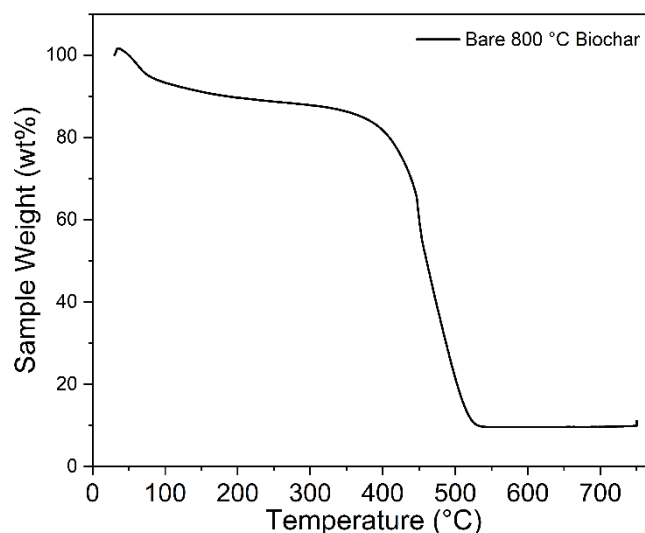


Figure 23: TGA Weight loss curve for Bare 800 °C Biochar

3.2.2 Ultimate analysis of bulk biochars

The ultimate analysis of the bulk biochars was carried out to see how the pyrolysis process affected the organic components, compared to the leached barley straw feedstock. From **Table 8**, it can be seen a that there is large increase in the carbon fraction from 44.90 wt% to 74.93 wt%. 78.92 wt%, 79.37 wt% and 75.59 wt% for the biochars produced at 500 °C, 600 °C, 700 °C and 800 °C. These are increases of 66.88 %, 75.77 %, 76.77 % and 68.35 %, respectively compared to the leached parent feedstock also shown in **Table 8**. This increases in carbon content as the temperature increases is due to the removal of oxygen from the feedstock, the dominate reaction in pyrolysis is the removal of oxygen without combusting to CO or CO₂. Additionally, through this process there is an increase in the peak size in terms of C=C and or C≡C bonding as temperature increases, as shown in **Figure 24**. This could link to removal of hydrogen and oxygen from the feedstock, especially as a core action of pyrolysis is deoxygenation of a material ¹³⁷. We can also see that as pyrolysis temperature is increased the content of hydrogen is reduced, in this case it goes from 6.41 wt% to 3.21 wt%, 2.22 wt%, 1.46 wt% and 1.68 wt% this is a decrease of 49.92 %, 65.37 %, 77.22 % and 73.79 % for 500 °C, 600 °C, 700 °C and 800 °C, respectively. In this case the hydrogen would be liberated as H₂,

CH₄ and in some cases a low concentration of NH₃. The decrease in hydrogen content and the increasing C/H ratio indicates carbonization as well as an increase the aromaticity of the biochar¹³⁸.

Table 8: Results from the ultimate analysis of raw and leached barley straw compared to that of biochar produces at 500°C, 600 °C, 700 °C and 800°C.

Feedstock	C (wt%)	H (wt%)	N (wt%)	C/H	C/N
Raw <0.25 mm Barley Straw	43.50	6.35	0.52	6.85	83.65
Leached <0.25 mm Barley Straw	44.90	6.41	0.30	7.00	149.67
500 °C Biochar	74.93	3.21	0.65	23.34	115.28
600 °C Biochar	78.92	2.22	1.27	35.55	62.14
700 °C Biochar	79.37	1.46	0.55	54.36	144.31
800 °C Biochar	75.59	1.68	1.48	44.99	51.07

3.2.3 FTIR analysis of bulk biochars

Figure 24, compared to that of **Figure 20** features have been smoothed/removed by the pyrolysis meaning that we have reduced and, in some cases lost functional groups. This is backed up by the TGA data showing the depolymerisation and breaking down of cellulose and hemicellulose, as well as some lignin between 200 °C to 500 °C. we can also see at 2097 cm⁻¹ a new peak starts to emerges at 500 °C, becoming more prominent as the temperature is increased, this is highlighted in **Figure 24** by a red box around the new group. From the spectra we can deduce that this is C=C=C or C≡C stretching, often seen as functionality pertaining to Lewis acid characteristics, which has been shown in the past to promote hydrogenation reactions¹³⁹. Also, it is seen that as the temperature increases the peak at 2097 cm⁻¹ becomes more prominent which means that the Lewis acid density increases as a function of temperature.

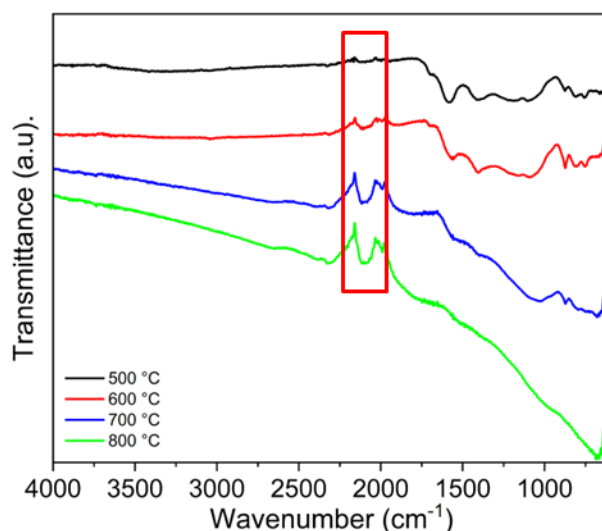


Figure 24: FTIR of biochar made at 500 °C, 600 °C, 700 °C and 800 °C.

3.2.4 SEM/EDX analysis of bulk biochars

SEM images of the bulk biochars were acquired and analysed to identify any differences in the surface morphology that have occurred due the different pyrolysis temperatures. This data is presented in **Figures 25-27**, where there does not appear to be a significant difference in the surface morphology of the biochars, meaning temperature has no obvious physical damage to the sample. We can see in image **Figure 25a**, **Figure 26a** and **Figure 27a** there are some surface characteristics that are present in all three samples. This means that the pyrolysis temperature does not affect these formations and that they are a natural feature of the barley straw waste, irrespective of thermochemical conversion. We can also see in **Figure 25b**, **Figure 26b** and **Figure 27b** that the pyrolysis temperatures do not affect the shape of the biochar particles, all three images have a similar appearance of just ‘chunks’ of barley straw that are now biochar, in essence a deoxygenated form of its parent self. Unfortunately, SEM images were not captured for the bare BC/800 sample, although it is safe to assume that it would be similar to BC/500, BC/600 and theorised

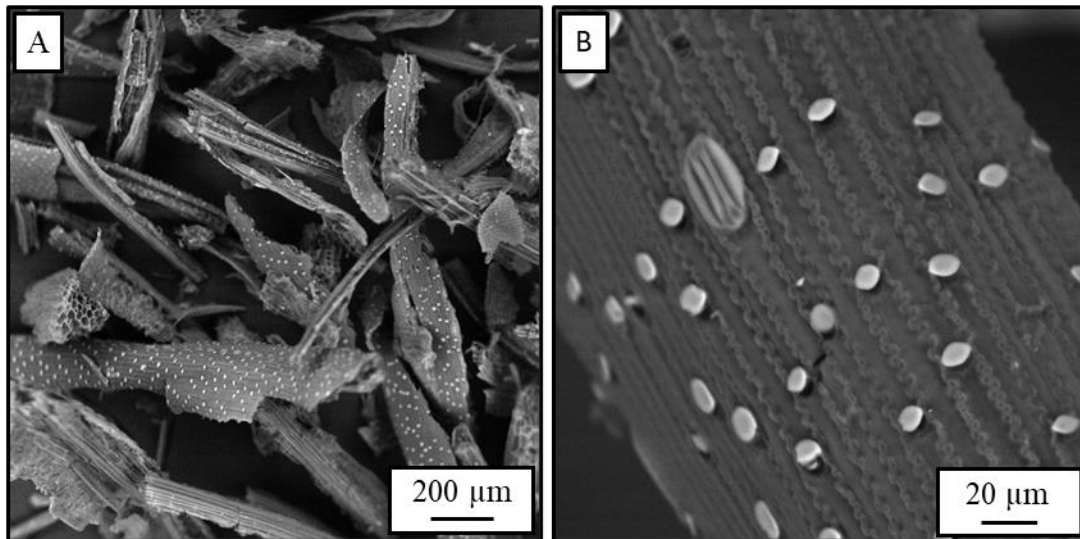


Figure 25: SEM images of [A] BC/500 biochar at a magnification of X100 and [B] BC/500 biochar at a magnification of X1000.

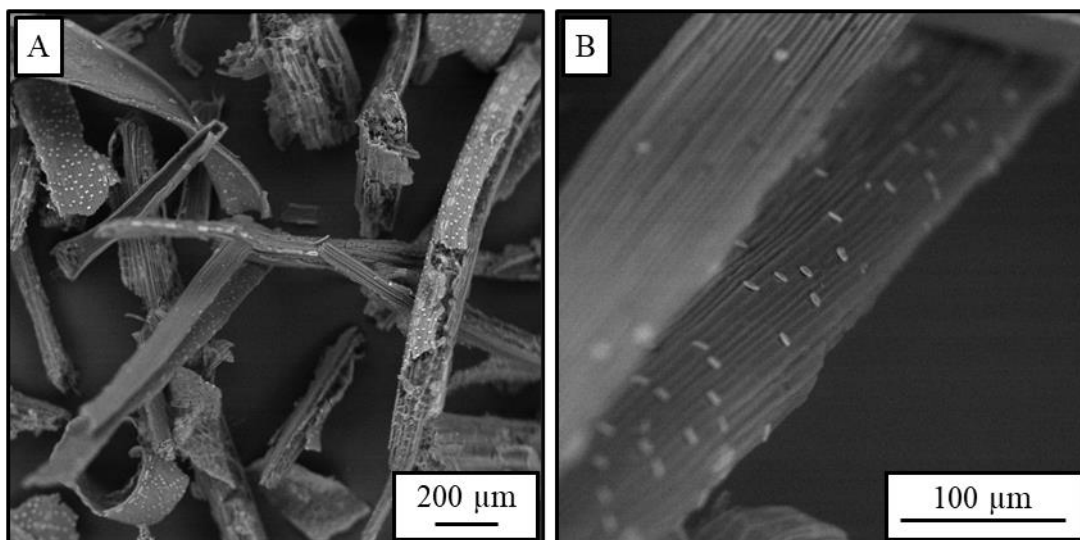


Figure 26: SEM images of: [A] BC/600 biochar at a magnification of X100 and [B] BC/600 biochar at a magnification of X500.

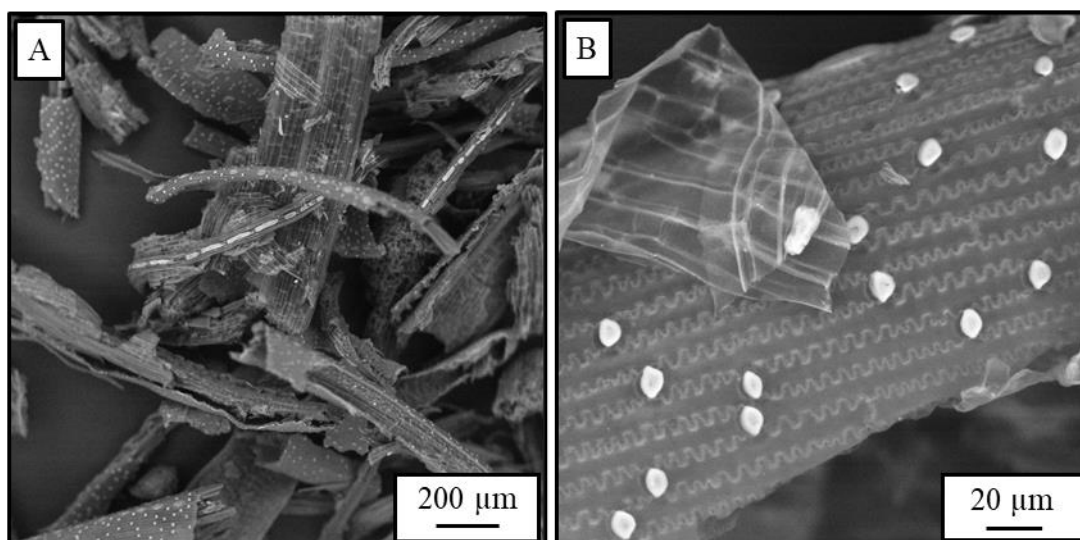


Figure 27: SEM images of: [A] BC/700 biochar at a magnification of X100 and [B] BC/700 biochar at a magnification of X1000.

3.2.5 Porosity of bulk biochars

Brunauer–Emmett–Teller (BET) analysis was carried out on the bulk biochars but a measurement was not able to be made this is due to the bulk nature of the biochar. This means that there was no measurable pore network, the bulk properties are visualised in the SEM data. It is expected from similar data reported by the Taylor group that the surface area of bulk barley straw could be similar to bulk wheat straw, where a surface area of $\sim 20.75 \text{ m}^2 \text{ g}^{-1}$ was found for a biochar carbonized at $400 \text{ }^\circ\text{C}$ ⁴¹.

3.3 Characterisation of Pd doped bulk biochars

As covered in **Chapter 2**, the family of synthesised biochars using the four different maximum pyrolysis temperatures, $500 \text{ }^\circ\text{C}$, $600 \text{ }^\circ\text{C}$, $700 \text{ }^\circ\text{C}$ and $800 \text{ }^\circ\text{C}$ where they were impregnated with palladium at a nominal loading of 1 wt%, using the wet impregnation method described in **Chapter 2**. After annealing to leave just Pd (ligand free), the Pd doped bulk biochars were characterised using techniques mentioned for the bare biochars, as well as EDX and TEM for Pd content present and nanoparticle sizing/distributions.

3.3.1 Thermogravimetric analysis of Pd doped bulk biochars

As we can see from **Figure 28** with comparison to **Figure 18**, they both start decomposing in air at ~ 400 °C, meaning that the thermal stability gained from the pyrolysis process was not lowered by the addition of Pd, as well as the annealing. An observation can be made that the addition of the Pd has made it so that the Pd doped bulk biochar break down at a slower rate than that of the basic bulk biochar.

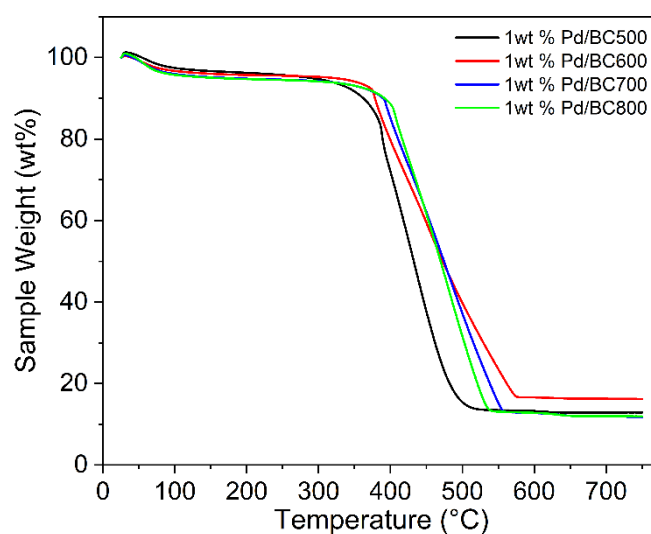


Figure 28: TGA weight loss curve for Pd doped bulk biochars Pd/BC500, Pd/BC600, Pd/BC700 and Pd/BC800

3.3.2 Textural properties of Pd doped bulk biochars

The ultimate analysis of Pd doped bulk biochars was done to see how the addition of Pd and the process of annealing affected the biochar structure compared to the bulk biochars. As we can see between **Table 8** and **Table 9**, the addition of Pd has had no significant effect on the content of carbon, hydrogen, or nitrogen within experimental error. Alongside Ultimate analysis Brunauer-Emmett-Teller (BET) was carried out on the Pd doped bulk biochars but as with the bulk biochars a measurement was not able to be made this is again due to the bulk nature of the biochar as well as what litter porosity the bare bulk has it may now be filled with Pd reducing the already small porosity reducing it even further.

Table 9: Results from the Ultimate analysis, TGA and BET of 1 wt% Pd/BC500, Pd/BC600, Pd/BC700, and Pd/BC800

Material	C (%)	H (%)	N (%)	Ash (wt%)	Surface area (m ² g ⁻¹)
Pd/BC500	45.07	1.51	0.45	12.99	Bulk
Pd/BC600	74.38	2.12	0.66	16.16	Bulk
Pd/BC700	78.85	1.96	0.56	11.76	Bulk
Pd/BC800	75.51	1.43	1.63	11.96	Bulk

3.3.3 FTIR of Pd doped bulk biochars

Again, in **Figure 29** we can see that there is known difference to the chemical bonding to the carbon structure previously seen for the bare biochars in **Figure 24**. This means that the Pd impregnation, as well as the annealing process has not affected the newly formed peak at 2097 cm⁻¹, indicating that this new peak is a stable formation in the biochar and that the C=C=C or C≡C are not reduced after further biochar processing after pyrolysis, also that their presence may have a driving force in the hydrogenation reactions.

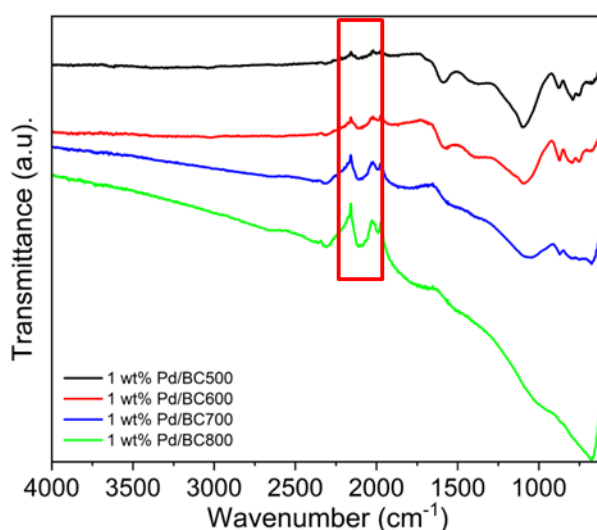


Figure 29: FTIR of 1 wt% Pd/BC500, 1 wt% Pd/BC600, 1 wt% Pd/BC700 and 1 wt% Pd/BC800

3.3.4 PXRD of Pd doped bulk biochars

As can be seen in **Figure 30**, we can observe that as the pyrolysis temperature is increased the less prominent the silicon impurities in the biochar become. This can also be seen more clearly in **Table 10** where it is shown that the silicon content reduces from 16.39% in leached barley straw to 11.80 %, 8.41 % and 7.02 % in BC/500, BC/600 and BC/700, respectively. Overall this is a reduction of 28% for BC/500, 49% for BC/600 and 57 % for BC/700, compared to that of leached barley straw. We can also clearly see the presence of Pd in the materials and from the diffractograms we can determine that the reflections seen are the Pd (111) at 40°, Pd (200) at 46° and Pd (220) at 67°^{87, 140}. The intensity in the reflections is variable depending on the presence of crystalline silica which cause the Pd reflections to appear higher/lower in intensity.

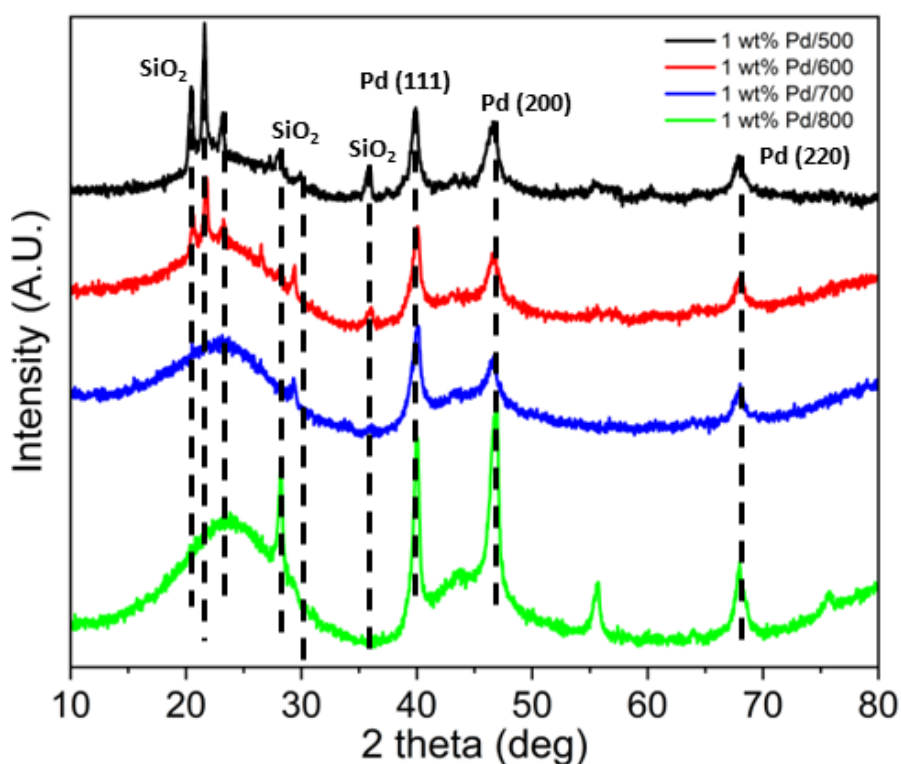


Figure 30: PXRD of Pd doped bulk biochar 1 wt% Pd/BC500, 1 wt% Pd/BC600, 1 wt% Pd/BC700 and 1 wt% Pd/BC800

Table 10: The reduction in silicon content in biochars by varying pyrolysis temperature.

Sample Name	Si (wt%)
Leached Barley Straw	16.39
BC/500	11.80
BC/600	8.41
BC/700	7.00

3.3.5 SEM/EDX of Pd doped bulk biochars

To look at the surface morphology for the bulk and mesoporous biochar, scanning electron microscopy (SEM) was carried out on the samples at different magnifications to look for differences in the structure that may result from the Pd impregnation and subsequent thermal processing in the N₂/H₂ stream to anneal and reduce the Pd nanoparticles. The Pd doped biochars were analysed and the images are presented in **Figures 31-Figure 34**. Collectively these images show the impact of different reaction conditions (including BC/800) on the structure of the biochar, both initial pyrolysis temperature, Pd impregnation and post addition thermal processing. Agreeing with the images shown for the Pd free biochars (**Figure 25-Figure 27**), the pyrolysis temperature has no effect on the overall surface morphology as all images appear similar. However, the images in **Figure 31-Figure 34** show a range of different grain sizes, this is believed to be due to manual grinding the materials into a powder form after annealing and reduction. **Table 11** shows the average Pd loading per biochar material, taken across a number of sites in different areas of the imaged sample. The measured Pd content was found to be 0.69 wt%, 0.71 wt%, 0.70 wt% and 0.64 wt% for Pd/BC500, Pd/BC600, Pd/BC700 and Pd/BC800, respectively. This data shows that across the samples, the Pd loadings across all four samples are very similar.

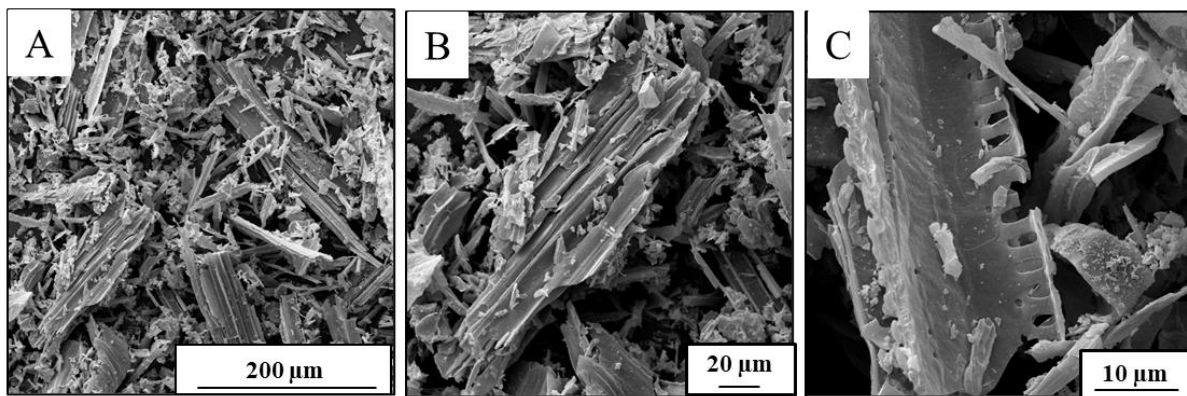


Figure 31: SEM image of [A] Pd/BC500 biochar at a magnification of X450, [B] Pd/BC500 biochar at a magnification of X1000, [C] Pd/BC500 biochar at a magnification of X4000

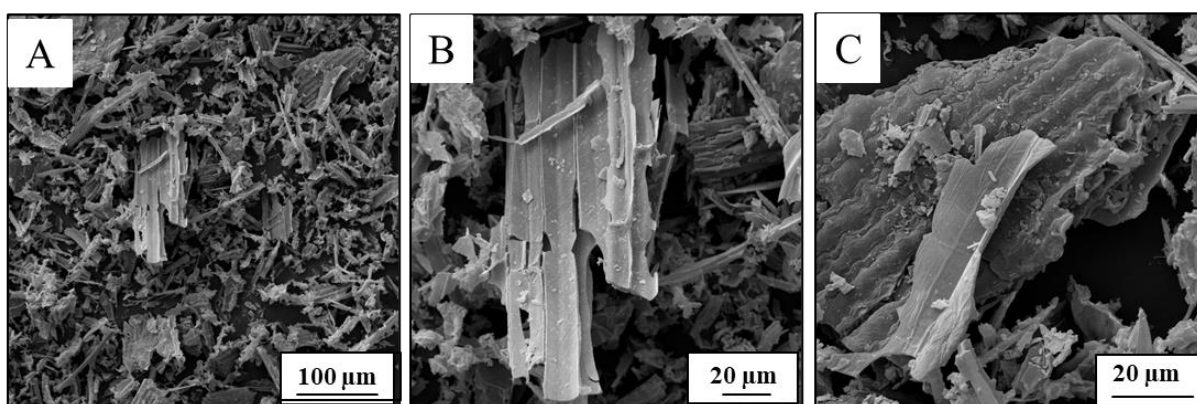


Figure 32: SEM image of [A] Pd/BC600 biochar at a magnification of X400, [B] Pd/BC600 biochar at a magnification of X1140, [C] Pd/BC600 biochar at a magnification of X2000

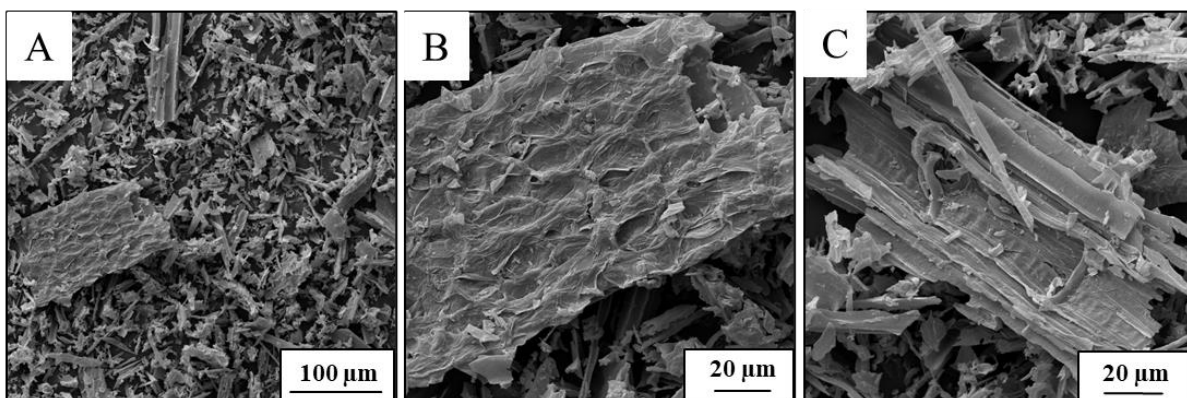


Figure 33: SEM image of [A] Pd/BC700 biochar at a magnification of X450, [B] Pd/BC700 biochar at a magnification of X1350, [C] Pd/BC700 biochar at a magnification of X1500

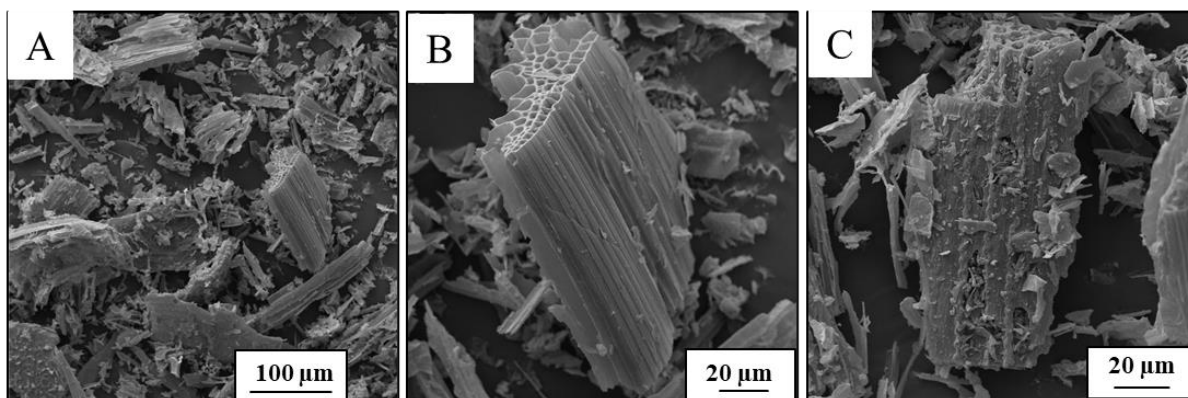


Figure 34: SEM image of [A] Pd/BC800 biochar at a magnification of X400, [B] Pd/BC800 biochar at a magnification of X1200, [C] Pd/BC800 biochar at a magnification of X1350

Table 11: Measured loading of Pd on bulk biochar through EDX

Sample	Pd/BC500	Pd/BC600	Pd/BC700	Pd/BC800
Pd loading	0.69 wt%	0.71 wt%	0.70 wt%	0.64 wt%

3.3.6 TEM of Pd doped bulk biochars with particle size histograms.

As we can see from **Figures 35-42**, we have generated Pd nanoparticles, dispersed across the biochar support. The clarity of the images is due the fact that Pd has a larger electron density compared to the carbon support, there contrasts under the electron beam ¹⁰. From these images we can see the measured size of the Pd (TEM) is within error of the XRD estimations (**Table 11**). It was found that as pyrolysis temperature was increased, the larger the Pd appeared after annealing. This is due to the metal support interactions between the Pd nanoparticle and the biochar support. In this case the biochar acts as a weak support in terms of attractions, apparently weakening as the pyrolysis temperature increased. Often, when nanoparticles increase in size across materials, one may assume that the metal loading is accountable. For the materials shown in **Table 12**, this is not the case as the Pd loading is similar across all four biochar supports. A similar trend for Pt nanoparticle support interactions has been shown previously, here ystalline supports such as γ -Al₂O₃, MgO, CeO₂ and ZnO have a far stronger

attraction meaning the nanoparticles do not agglomerate and appear monodisperse ¹¹. However, a support such as amorphous SiO₂, does not show this feature and result in a more polydisperse size with agglomerates forming. The biochars are mostly amorphous in nature and therefore act similarly (in terms of metal support interactions) with SiO₂.

The variation in Pd particles sizes is shown in **Table 12**, comparing the estimated XRD size again the measured particles from TEM images are shown to be spherical in nature and presented in **Figures 35, 37, 39 and 41**, with corresponding particle size distributions in **Figures 36, 38, 40, 42**. The histograms show that the nanoparticles range between 3-8 nm, averaging at 6.30 ± 3.22 nm for 1 wt% Pd/BC500, 6.31 ± 3.38 nm for 1 wt% Pd/BC600, 6.23 ± 2.72 nm for 1 wt% Pd/BC700 and 7.48 ± 4.03 nm for 1 wt% Pd/BC800. This data shows that although globally the nanoparticle size is similar for the four materials, there is a mild variation in particle sizes, if considering the standard deviations which follow a linear trend (assuming 1 wt% Pd/BC700 as an outlier) of increasing as pyrolysis temperature increases. For the 1 wt% Pd/BC800 material, the broader particle size variation is mapped to measured, individual particles of 13-18 nm, with some agglomeration beginning to occur.

Table 12: Results of TEM and XRD showing Pd sizing and loading.

Material	Pd (wt%)	Pd size (XRD) (nm)	Pd size (TEM) (nm)
Pd/BC500	0.69 ± 0.32	7.99	6.30 ± 3.22
Pd/BC600	0.71 ± 0.47	8.20	6.31 ± 3.38
Pd/BC700	0.70 ± 0.30	8.75	6.23 ± 2.72
Pd/BC800	0.64 ± 0.18	9.40	7.48 ± 4.03

Figure 35c shows high resolution image of a single Pd nanoparticle, impregnated into the BC500 support. At atomic resolution, one can perfectly see the Pd atom arrangement that make up the nanoparticle. By measuring the distance between Pd atoms, the lattice spacing can be deduced to rationalise the overall structure. The XRD data previously in **Figure 30** shows that

the dominant reflection is the Pd (111). The measured lattice spacing in **Figure 35c** was found to be 0.23 nm, this is indicative of the (111) atom arrangement, validating the XRD data.

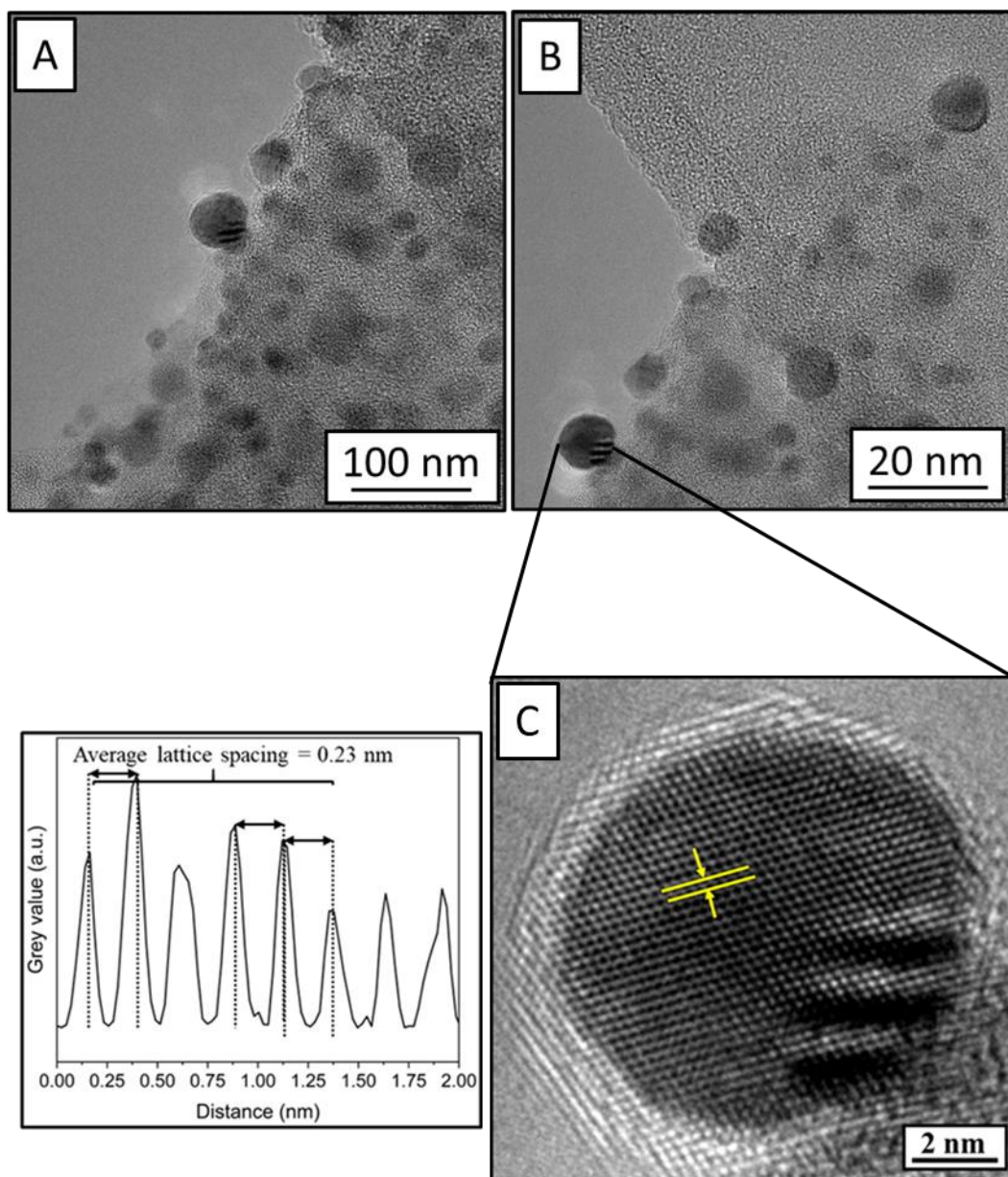


Figure 35: TEM images of [A] Site A of Pd/BC500, [B] Site B of Pd/BC500 at similar magnifications and [C] An atomically resolved Pd nanoparticle with accompanying lattice spacing

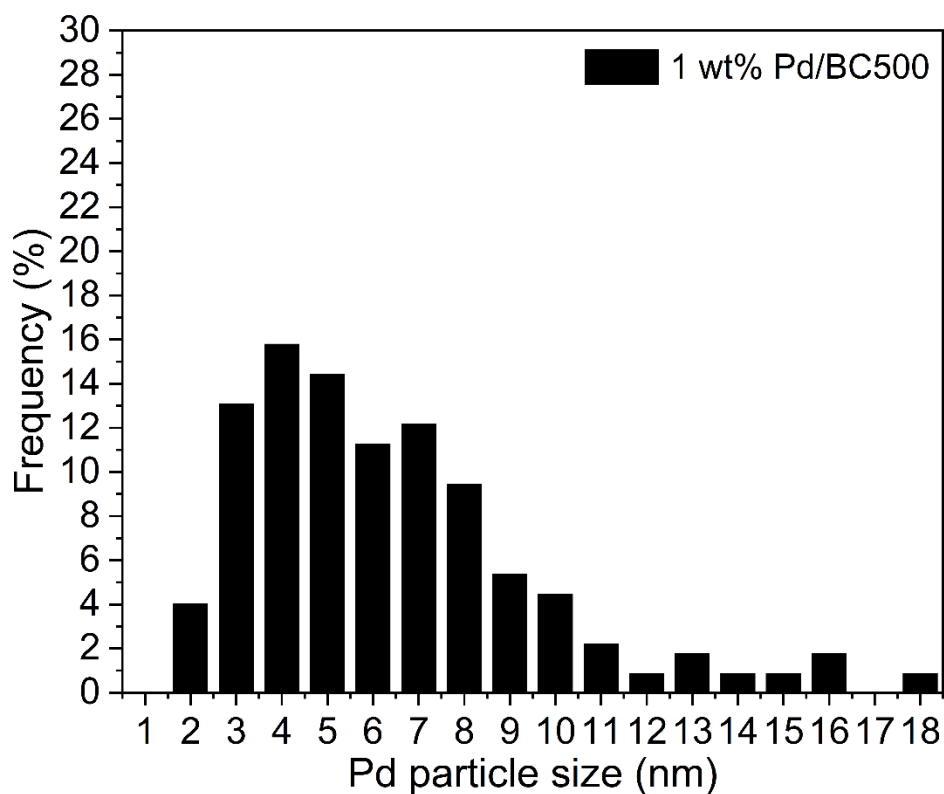


Figure 36: Pd particle size distribution for Pd/BC500

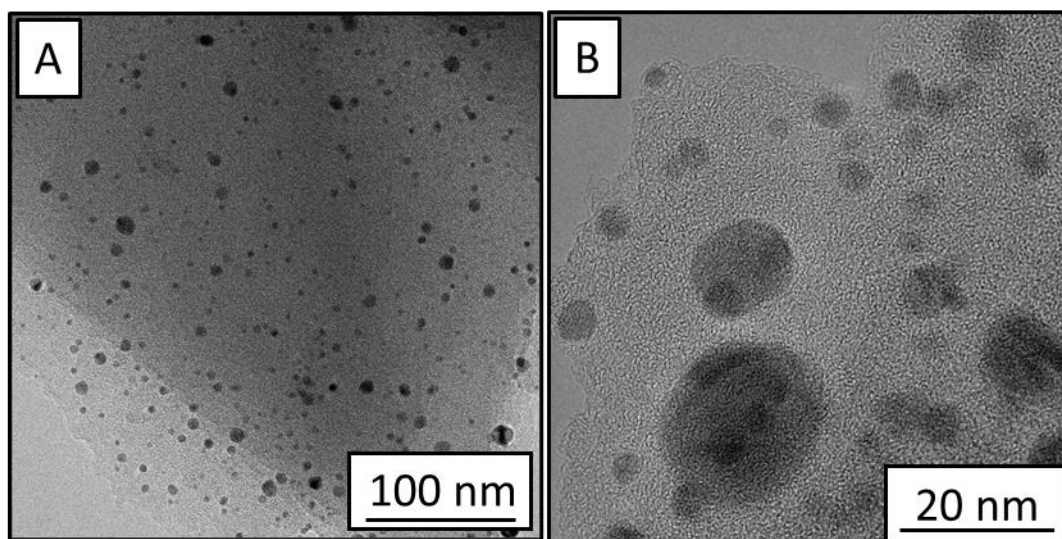


Figure 37: TEM images of [A] Site A of Pd/BC600 at low magnification and [B] Site B of Pd/BC600 at high magnification.

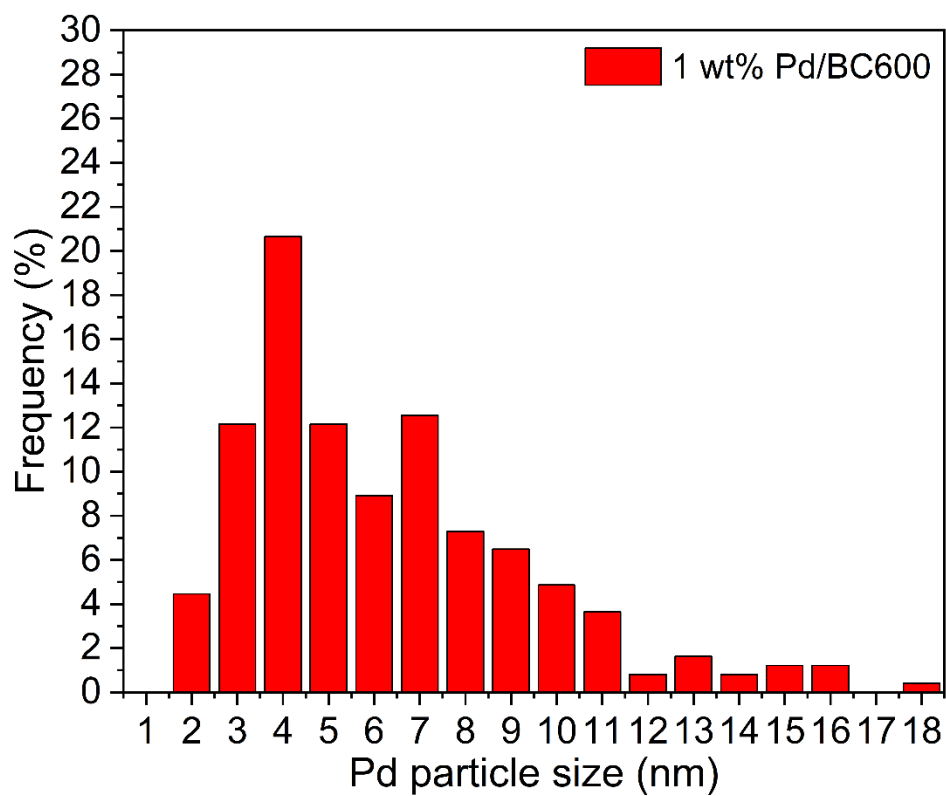


Figure 38: Pd particle size distribution for Pd/BC600

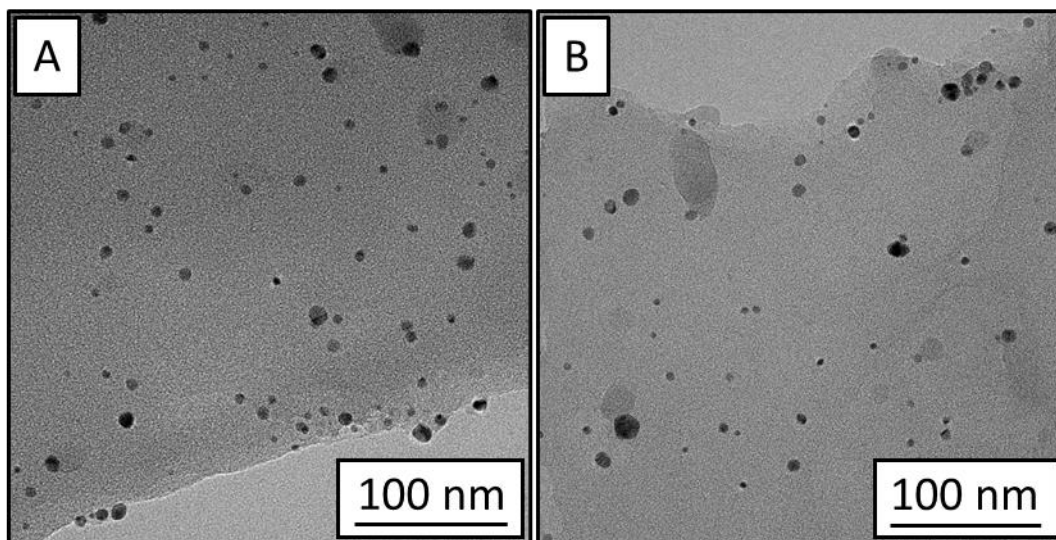


Figure 39: TEM images of [A]site A of Pd/BC700 [B] Site B of Pd/BC700 both at similar magnification

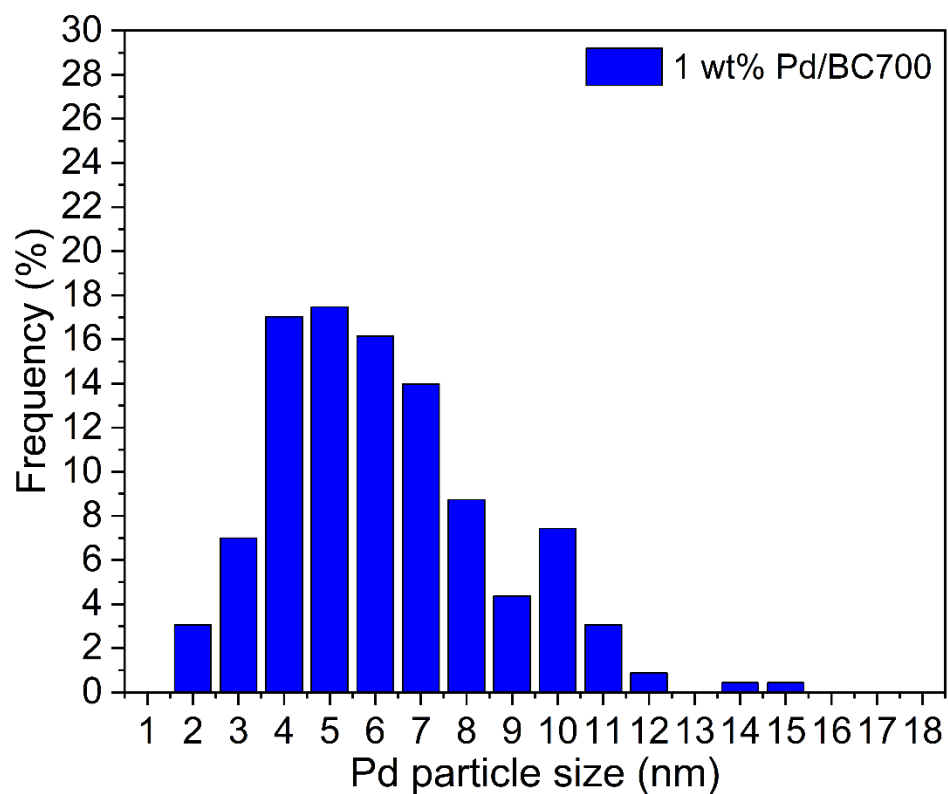


Figure 40: Pd particle size distribution for Pd/BC700

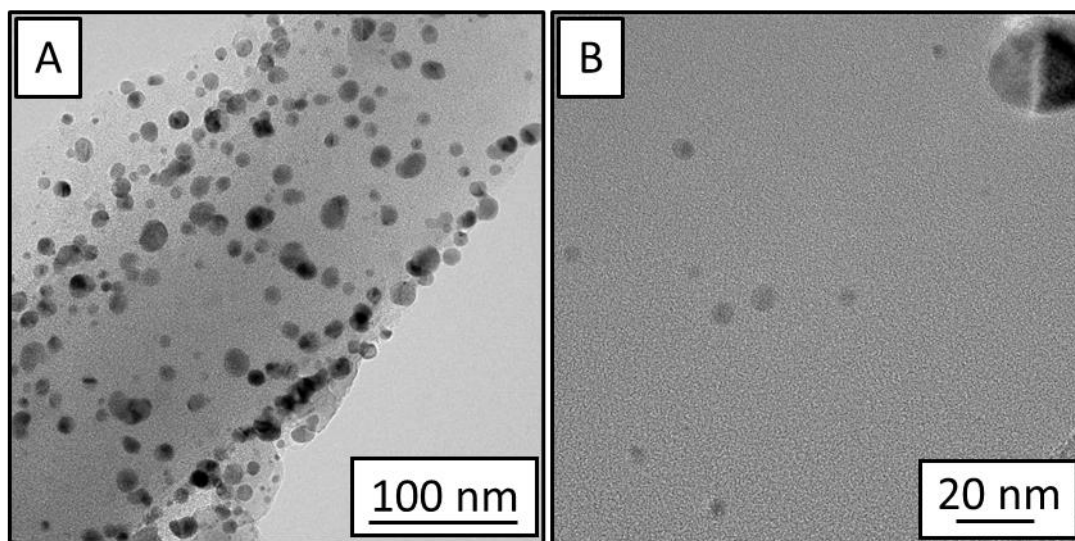


Figure 41: TEM images of [A] Pd/BC800 [B] Pd/BC800

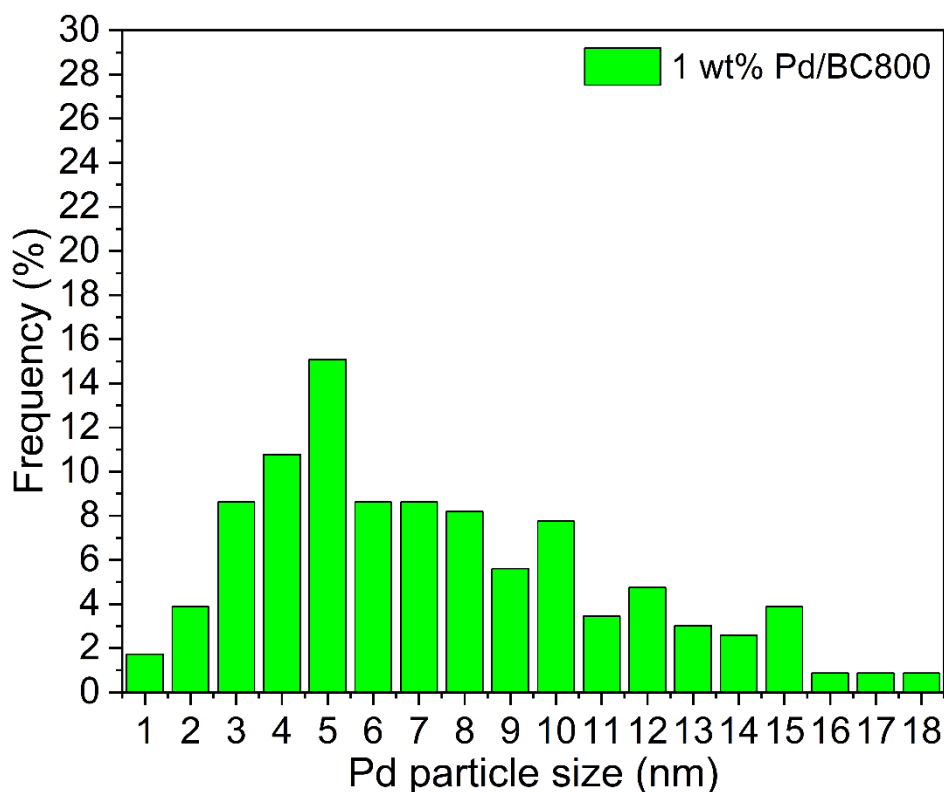


Figure 42: Pd particle size distribution for Pd/BC800

3.4 Characterisation of high surface area mesoporous biochars

As covered in **Chapter 2**, a family of mesoporous biochar were synthesised using three different weight ratios of barley straw to potassium hydroxide (KOH), 1:1, 1:0.25 and 1:0.25. Post pyrolysis the materials were refluxed in hydrochloric acid and washed in deionised water to remove the KOH, as well as any soluble ash components. The resulting mesoporous biochars were characterised using techniques mentioned for the previous bulk biochar.

3.4.1 Thermogravimetric analysis of mesoporous biochars

As we have already established in the previous section, the biochar becomes more thermally stable after pyrolysis. Where the raw and leached feedstock would begin to decompose from 200 °C in nitrogen, the bulk biochar started to decompose/combust at 400 °C (air). We can see in **Figure 43** that the mesoporous biochars had a further improvement to its thermal stability as they begin to decompose in air at >500 °C. This is assumed to be due to the effect of the KOH impregnation and the subsequent hydrolysed of cellulose and hemicellulose, leading to a

structural rearrangement where the lignin polymeric backbone has been altered. In addition, it has been found in the literature that the addition of KOH into a biomass residue will slow the thermal degradation of the remaining cellulose, that wasn't removed during the hydrolysis processing¹⁴¹. **Figure 43** shows that there is a substantial decrease in weight during the first thermal stage, moisture removal. Due to their porous and somewhat hygroscopic nature, they are able to store a lot of water from the atmosphere, as shown by ABC-0.5 which has an initial decrease of ~17 wt%. Although this material does not have the highest surface area and available pore network, the heightened moisture value for this material was subject to how it was stored (not in an oven or desiccator).

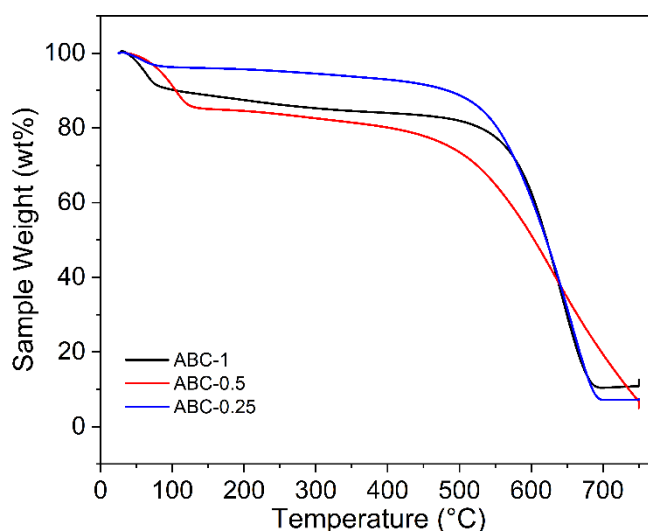


Figure 43: TGA weight loss curve for mesoporous biochars ABC-1, ABC-0.5 and ABC-0.25

3.4.2 Textural properties of high surface area mesoporous biochars.

For this section we compare the carbon, hydrogen and nitrogen from the bulk biochar created at 800 °C as a benchmark material, to that of the mesoporous biochars as both were created at 800 °C. **Table 13** shows that ABC-1 and ABC-0.5 has lower carbon, hydrogen, and nitrogen compared to the bulk BC800 material, this makes logical sense as the KOH has hydrolysed the cellulose and hemicellulose, by doing so liberating CO and CO₂, as shown in **Equations 2-4**,

as a result losing carbon into the gas phase prior to pyrolysis. It is anticipated that the incorporation of higher KOH concentration will lead to deeper carbon removal from the biochars, resulting in a lower carbon and hydrogen content, while nitrogen could be found to increase through the pyrolysis process. In **Figure 44** is a stacked plot of the BET isotherms from ABC-1, ABC-0.5 and ABC-0.25. Using this data, we can deduce this is a mesoporous material through the large adsorption capacity (higher nitrogen quantity adsorbed). We can understand from this data that the plots resemble type IV isotherms which is also indicative of a mesoporous material. Moreover, and possibly the most striking addition is the rapid expansion of available surface area for this family of materials. **Table 13** shows that by starting with the lowest KOH loading, the surface area of the char begins to develop ($1095.23 \text{ m}^2 \text{ g}^{-1}$). As the KOH content increases, ABC-0.5 presented an available surface area of $1392.87 \text{ m}^2 \text{ g}^{-1}$, this is an increase of 1.27x. This increases further for ABC-1 to $1436.81 \text{ m}^2 \text{ g}^{-1}$, a further 1.03x increase and overall resulting in a surface area 1.31x greater than the lowest KOH addition.

Table 13: Results from the ultimate analysis, TGA and BET of ABC-1, ABC-0.5, ABC-0.25

Material	C (wt%)	H (wt%)	N (wt%)	Ash (wt%)	Surface area ($\text{m}^2 \text{ g}^{-1}$)	Pore Volume ($\text{cm}^3 \text{ g}^{-1}$)	Pore size (nm)
BC800	75.59	1.68	1.48	11.14	Bulk	-	-
ABC-1	71.26	0.83	1.24	12.61	1436.81	0.36	3.90
ABC-0.5	69.49	1.52	1.22	7.35	1392.87	0.41	6.60
ABC-0.25	79.13	1.79	1.19	4.99	1095.23	0.17	4.20

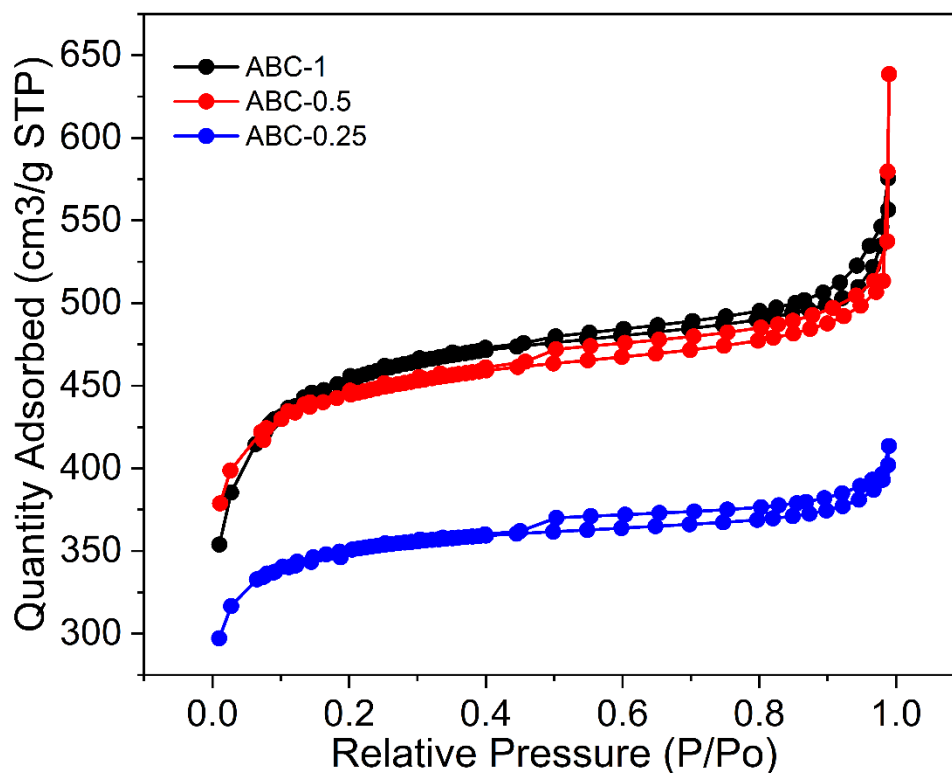


Figure 44: A stacked plot of BET Isotherms for ABC-1, ABC-0.5 and ABC-0.25

3.4.3 FTIR of mesoporous biochars

As we can see from **Figure 45**, the FTIR spectra of the three mesoporous biochars shows that, similarly with the bulk biochars, there is a drastic reduction in functional groups in comparison to the virgin feedstock. Again, the peak at 2097 cm^{-1} is characterised as either $\text{C}=\text{C}=\text{C}$ or $\text{C}\equiv\text{C}$ and induced through the thermochemical process. As previously understood, these are known to influence Lewis acid characteristics which has been shown in the past to promote hydrogenation reactions¹³⁹. This feature does not appear to increase/decrease with respect to KOH addition, meaning that it is purely temperature based and appear to the same magnitude as the BC800 material shown in **Figure 29**. Although it can be assumed to show similar Lewis acidity, it can be assumed that a highly porous material could result in a greater dispersion of surface Lewis acidity, opposed to highly concentrated areas for the bulk material. There is also

a small feature around 2800 cm^{-1} which is emerging, this is typically assigned to CO_2 , most likely derived from atmospheric adsorption.

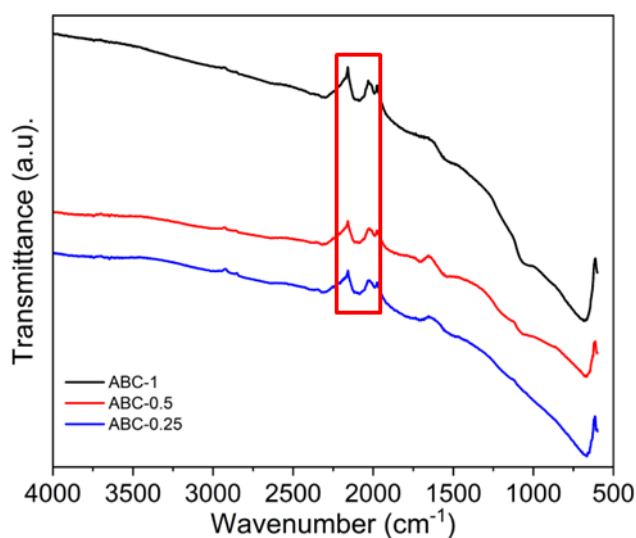


Figure 45: FTIR spectra of ABC-1, ABC-0.5, ABC-0.25

3.4.3 XRD of mesoporous biochars

Figure 46 shows stacked x-ray diffractograms of the three mesoporous biochars, compared with the benchmark BC800. Exhibiting the same amorphous carbon and turbostratic structure at 43° , the BC800 material shows a series of well-defined crystalline peaks at 28° , 46° , 56° , 65° and 69° which have been shown previously to be silicon-based entities in the carbon structure, namely, the Si (111), (220), (311), (400) and (331). After feedstock pre-treatment (KOH addition with sonication) and the post pyrolysis processing in the form of acid reflux and washing, it appears that the silicon previously present has been either removed or dramatically reduced. As silicon is not digested by HCl, it is assumed that the initial pre-treatment with KOH has liberated or led to the evolution of silicon containing volatiles during pyrolysis, possibly through a structural weakening during the hydrolysis steps^{142, 143}. However, the acid can digest other elements in the ash such as Ca, Cl, Na and Fe leaving behind a ‘purer’ carbon, albeit in a mostly amorphous state¹⁴⁴.

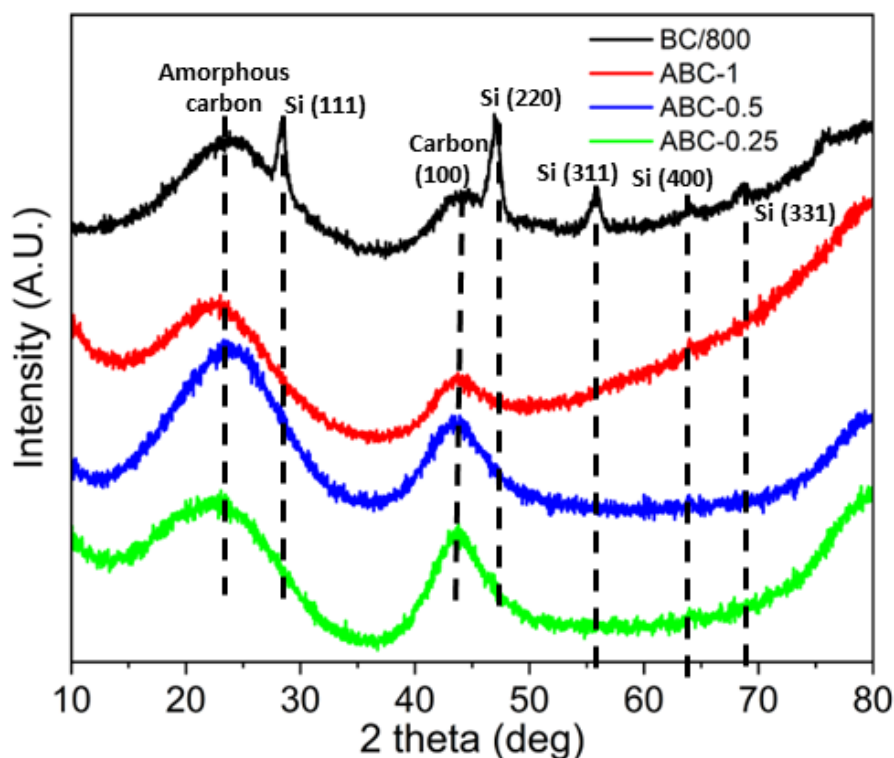


Figure 46: PXRD of mesoporous biochars ABC-1, ABC-0.5 and ABC-0.25 with comparison to the bulk biochar BC/800

3.5 Characterisation of high surface area, Pd doped mesoporous biochars

Following the development of the mesoporous biochars, they were subsequently impregnated with palladium to achieve a nominal loading of 1 wt% using the method described in **Chapter 2** and shown to be effective earlier in this chapter. After the metal salt was dispersed in solution and mixed with the mesoporous biochar, it is believed that diffusion will be facilitated throughout the mesoporous structure, as well as on the bulk surface. Once dried, the material was annealed and reduced to remove the precursor ligand and leave behind Pd⁰. The resulting Pd doped mesoporous biochars denoted as 1 wt% Pd/ABC-1, 1 wt% Pd/ABC-0.5 and 1 wt% Pd/ABC-0.25 where characterised using techniques mentioned previously.

3.5.1 Thermogravimetric analysis of mesoporous Pd doped biochars

Once again, the Pd doped mesoporous biochars mimic the thermal stability to the Pd free biochars. However, in this case the inherent moisture content is much lower the materials shown in **Figure 47**.

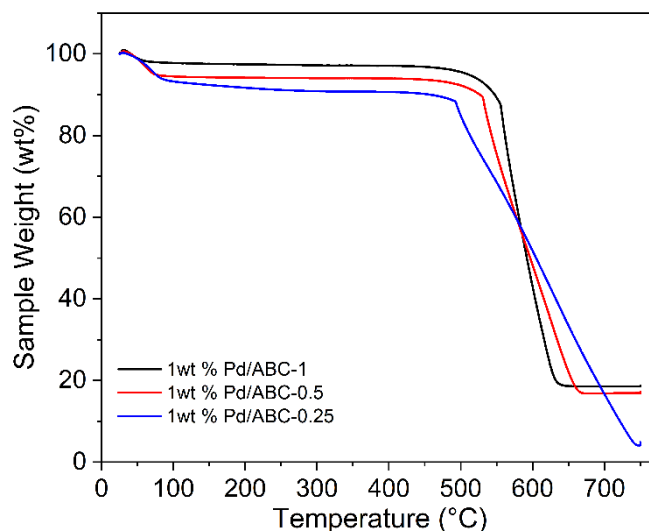


Figure 47: TGA weight loss curve for mesoporous Pd doped biochars Pd/ABC-1, Pd/ABC-0.5 and Pd/ABC-0.25

3.5.2 Textural properties of mesoporous Pd doped biochars

Table 14 shows a direct comparison with **Table 13**. The values are within the expected experimental error and natural variance of the feedstock. With this in mind, we can confidently state that the addition of the Pd has not significantly altered the biochar and its ash content. Again, we can look at the isotherms shown in **Figure 48** to understand how the addition of Pd can alter the pore structure, especially after annealing. Often this results in a slight decrease in available surface area and pore volume as the impregnation process will deposit components into the support structure. In **Figure 48** we can see that for Pd/ABC-1 and Pd/ABC-1, their isotherm remains similar to **Figure 44**, meaning this it is a type IV mesoporous isotherm. However, the isotherm for Pd/ABC-0.25 appears different. The adsorption section of the isotherm remains consistent with that of its equivalent in **Figure 44**, but the desorption

component is not correct, potentially due to a fault during data collection. This does not affect the data presented as all values used are from the adsorption values, not desorption.

Table 14: Results from the Ultimate analysis, TGA and BET of 1 wt% Pd/ABC-1, 1 wt% Pd/ABC-0.5 and 1 wt% Pd/ABC-0.25

Material	C (wt%)	H (wt%)	N (wt%)	Ash (wt%)	Surface area (m ² g ⁻¹)	Pore Volume (cm ³ g ⁻¹)	Pore size (nm)
Pd/ABC-1	75.40	0.00	1.22	18.70	1329.31	0.38	4.30
Pd/ABC-0.5	85.60	0.82	1.22	17.16	1368.82	0.49	3.90
Pd/ABC-0.25	75.58	0.82	1.19	4.92	989.00	0.13	3.20

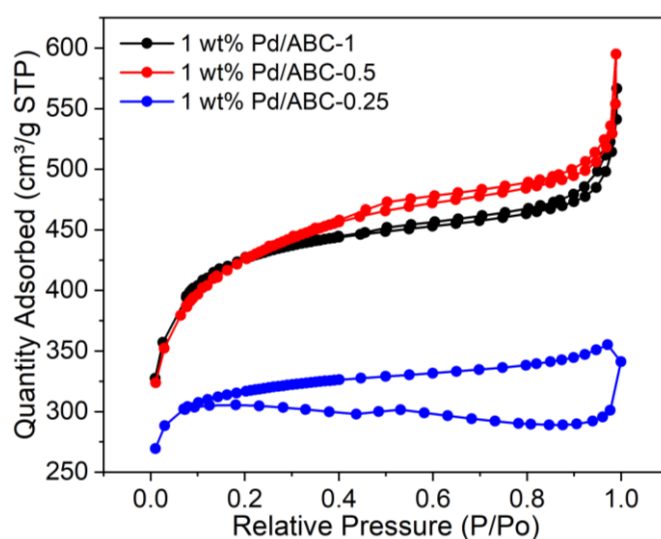


Figure 48: A stacked plot of BET Isotherms for Pd/ABC-1, Pd/ABC-0.5 and Pd/ABC-0.25

3.5.3 FTIR comparison of mesoporous Pd doped biochars

We can see by comparing **Figure 45** and **Figure 49**, the data are within experimental error, this indicates that the addition of Pd and the process of annealing has no significant effect on of the structure of the Pd doped mesoporous biochar. This specifically pertains to the organic structure present, this also shows that the indicated C=C=C linkages have not been removed/disrupted through the addition of the Pd and further thermal processing.

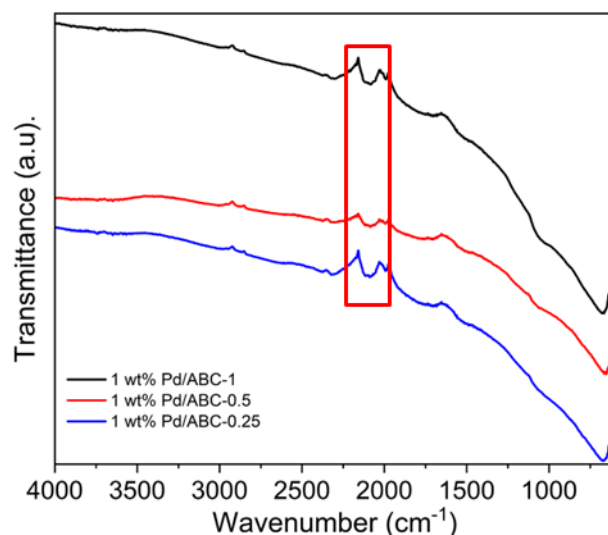


Figure 49: FTIR of Pd/ABC-1, Pd/ABC-0.5 and Pd/ABC-0.25

3.5.4 XRD of mesoporous Pd doped biochars

In **Figure 50** we can see that the impregnation of Pd has been successful, similarly with the bulk biochars previously shown (**Figure 46**). Additionally, the data shows that there is no contamination/anomalies, including silica that has been previously seen for biochars. Each of the Pd entities can be indexed in the same manner as before, this means that the reflections observed are Pd (111), Pd (200) and Pd (220)¹⁴⁰. A note of mention is that due to different sample quantities available, a different form of sample mounting was used for Pd/ABC-1 and Pd/ABC-0.5, utilising a much lower sample mass on a zero-background holder. As a result, the counts obtained were far lower than the Pd/ABC-0.25. As the data presented is not variable to its counterparts, the overall intensity for this scan was reduced by 100x.

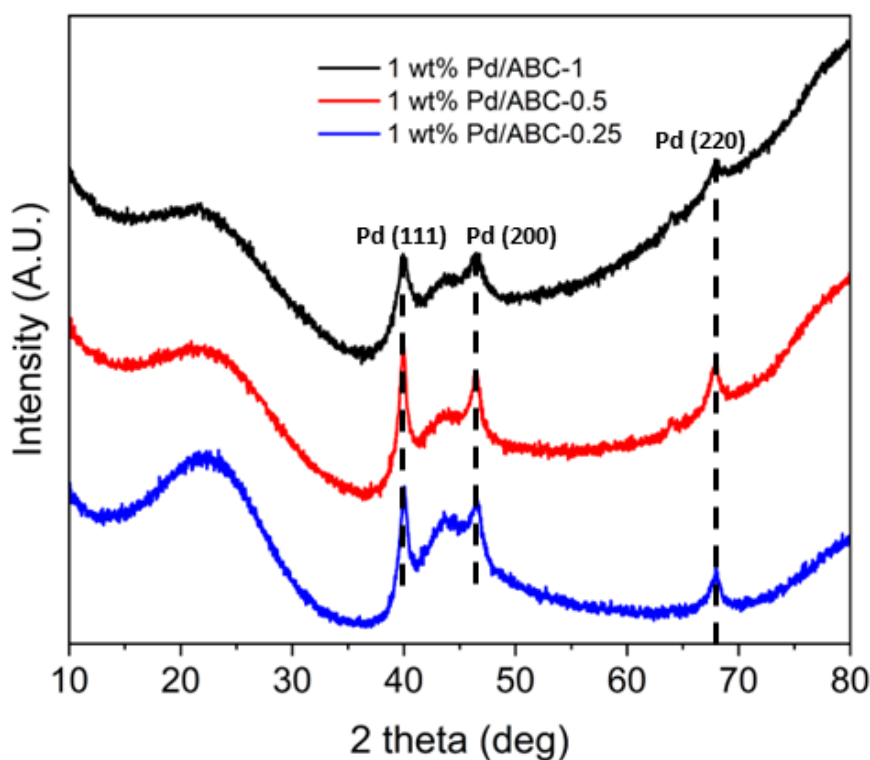


Figure 50: PXRD of mesoporous Pd doped biochars Pd/ABC-1, Pd/ABC-0.5 and Pd/ABC-0.25 (the data shown for Pd/ABC-0.25 has been divided by 100x to bring its intensity in line with the other two samples due to different sample amounts used)

3.5.5 SEM/EDX of mesoporous Pd doped biochars

A few grains of biochar were analysed and are presented in **Figures 51-53**. This data elegantly shows the impact of the KOH added to the feedstock before pyrolysis and how this affects the structure once pyrolyzed. For the Pd/ABC-1, which is born from a 1:1 biomass-KOH ratio, there is a well-defined network of pores that can be seen in **Figure 51a**, with subsequent images at increasing magnification in **Figure 51b** and **Figure 51c**. **Figure 51c** shows the pore structure at 25000x magnification where one can see the various cavities in the material, strikingly different to the bulk biochars previously seen which still resembled the parent barley straw structure. We can also see that the effect of KOH for the 1:0.5 (Pd/ABC-0.5, **Figures 52a-c**) material has a different the pore network structure, far less defined than that of the KOH 1:1. Ultimately, although more structured than the bulk biochars, the cavities seen in **Figure 51b-c** are not present, albeit still presenting a high surface area. Finally, in **Figures 53**, Pd/ABC-0.25 appears to heavily resemble the parent barley straw in part, as it is far less “fluffy”, this is

shown in **Figure 53b** and **Figure 53c**. Although this material doesn't appear in the same way as **Figure 51** and **Figure 52**, the pore network is evident and the structure on a whole still appears to have a honeycomb nature (**Figure 53b**) with a variety of cavities present at different sizes. The biochar chemical activation route using KOH has been shown previously in the literature, this shows how the surface of the biochar can be modified to provide a "sponge-like" morphology ¹²⁰. By exploring these materials in the same method as before, via wide EDX scans in a number of regions, the Pd content was found to be 0.25 ± 0.17 wt%, 0.53 ± 0.19 wt% and 0.21 ± 0.07 wt% for Pd/ABC-1, Pd/ABC-0.5 and Pd/ABC-0.25, respectively. This shows that across the samples, the observed Pd loading is different across the three samples is highly variable, as compared to the values shown in **Table 11** to the values in **Table 15**. Although the method of wet impregnation was the same between materials, one can assume that due to the expanded surface area and pore structure, the Pd is far more dispersed into the material. This means that in the specific wide scans obtained, the Pd present could be variable (low in some regions and comparatively higher in concentration in others). However, **Table 15** shows for these scans, there was not substantial variation in Pd content per sample (low standard deviation values). For these materials a more quantitative method of analysis is required such as inductive coupled plasma (ICP), after complete digestion.

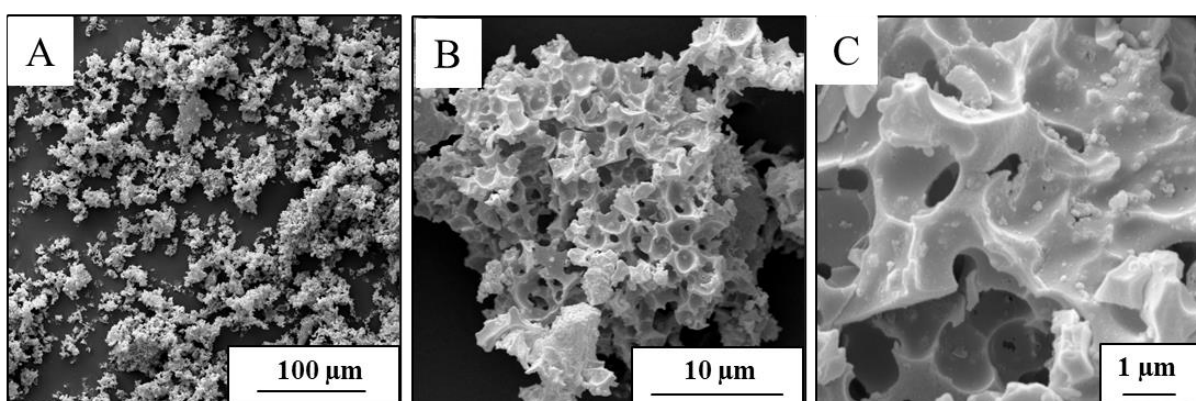


Figure 51: SEM image of [A] Pd/ABC-1 at a magnification of X500, [B] Pd/ABC-1 at a magnification of X2500 and [C] Pd/ABC-1 at a magnification of X25000

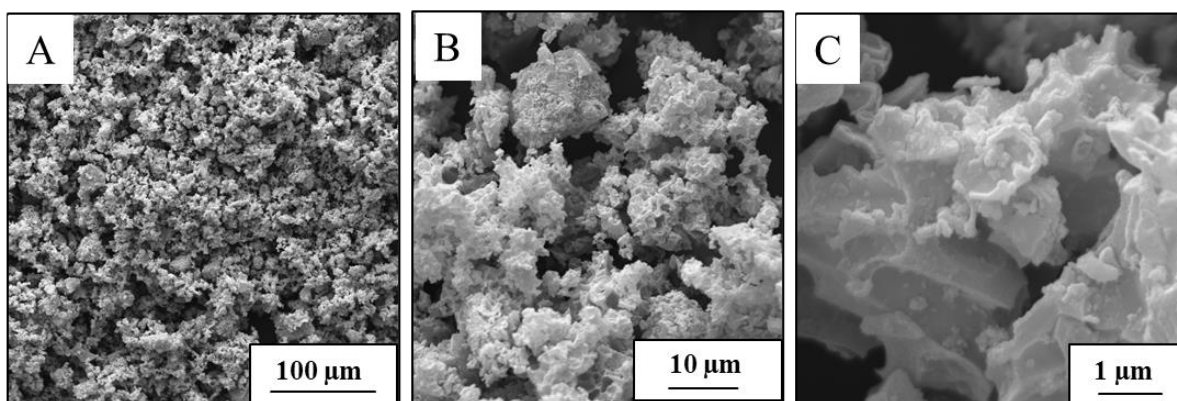


Figure 52: SEM image of [A] Pd/ABC-0.5 at a magnification of X500, [B] Pd/ABC-0.5 at a magnification of X2500 and [C] Pd/ABC-0.5 at a magnification of X25000

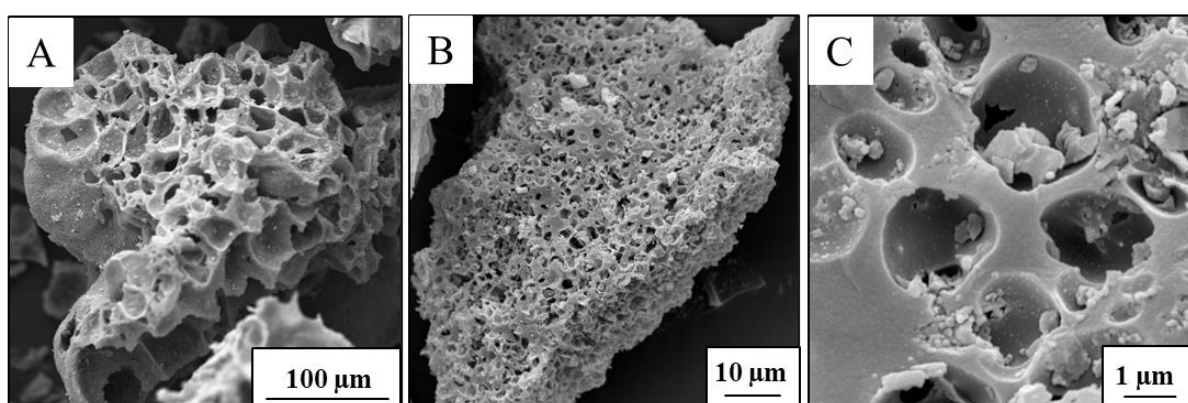


Figure 53: SEM image of [A] Pd/ABC-0.25 biochar at a magnification of X500, [B] Pd/ABC-0.25 biochar at a magnification of X2500 and [C] Pd/ABC-0.25 biochar at a magnification of X25000

Table 15: Measured loading of Pd on mesoporous biochar through EDX

Metal	Pd/ABC-1	Pd/ABC-0.5	Pd/ABC-0.25
Pd	0.29 ± 0.17 wt%	0.53 ± 0.19 wt%	0.21 ± 0.07 wt%

3.5.6 TEM of mesoporous Pd doped biochars with particle size histograms

As we can see from **Figures 54-57**, Pd nanoparticles have once again been synthesised and dispersed across the mesoporous support. The clarity of these images, specifically the metal vs support, is again due to Pd owning a larger electron density compared to the carbon support and therefore providing much greater contrast under the electron beam. We can see from the images that the measured size of the Pd (TEM) is not within the error of the XRD estimations (**Table 15**). However, they are very similar to the Pd/BC samples suggesting that the method of Pd

impregnation was clearly translated across all materials and the overall methodology was reproducible. Reasons as to why the XRD data for the ABC samples was higher pertains to the quality of the scans taken. Previously, it was mentioned that there were low sample quantities used for these scans. This would suggest that (although not seen in the stack a plot as the data are equivalent), the signal to noise ratio has caused the variations in the software outputs, that and a slightly rising background. To overcome this, one could manually integrate the peaks and deduce the FWHM and calculate the particle size. However, the use of PXRD for this was not its primary purpose and a more accurate method of particle sizing was used, TEM. Interestingly, the TEM images showed that although there were clear agglomerates found, the physical shape of the nanoparticles was a mixture of spherical **Figure 54** and rectangular **Figure 56b**.

The particle size histograms show that the nanoparticles range between 2-6 nm, averaging at 5.75 ± 3.75 nm for Pd/ABC-1 and 5.29 ± 3.78 nm for Pd/ABC-0.25 nm. Due to availability of TEM beamtime, the Pd/ABC0.5 material was not imaged. The XRD estimations shown in **Table 16**, although previously stated to not be comparable to the TEM data, the size rationale shown is logical. This data suggests that as the KOH concentration used increased, the resulting material and its Pd particle size increased. In terms of thermal stability, although shown on a bulk level to be comparable, it can be assumed that the metal-support interactions could be weaker as the material becomes more porous. As a result, the Pd particle size could be seen to increase subtly.

Table 16: Table 15: Tables showing estimated and measured Pd size.

Material	Pd (wt%)	Pd size (XRD) (nm)	Pd size (TEM) (nm)
Pd/ABC-1	0.29 ± 0.17	12.09	5.75 ± 3.75
Pd/ABC-0.5	0.53 ± 0.19	10.05	N/A
Pd/ABC-0.25	0.21 ± 0.07	7.46	5.29 ± 3.78

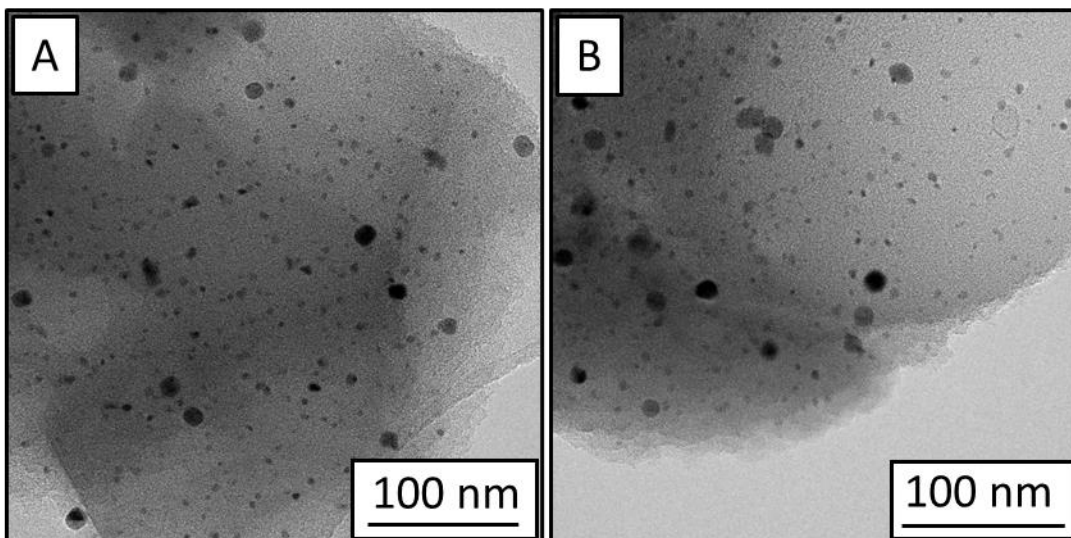


Figure 54: Representative TEM images of [A] Pd/ABC-1 and [B] Pd/ABC-1

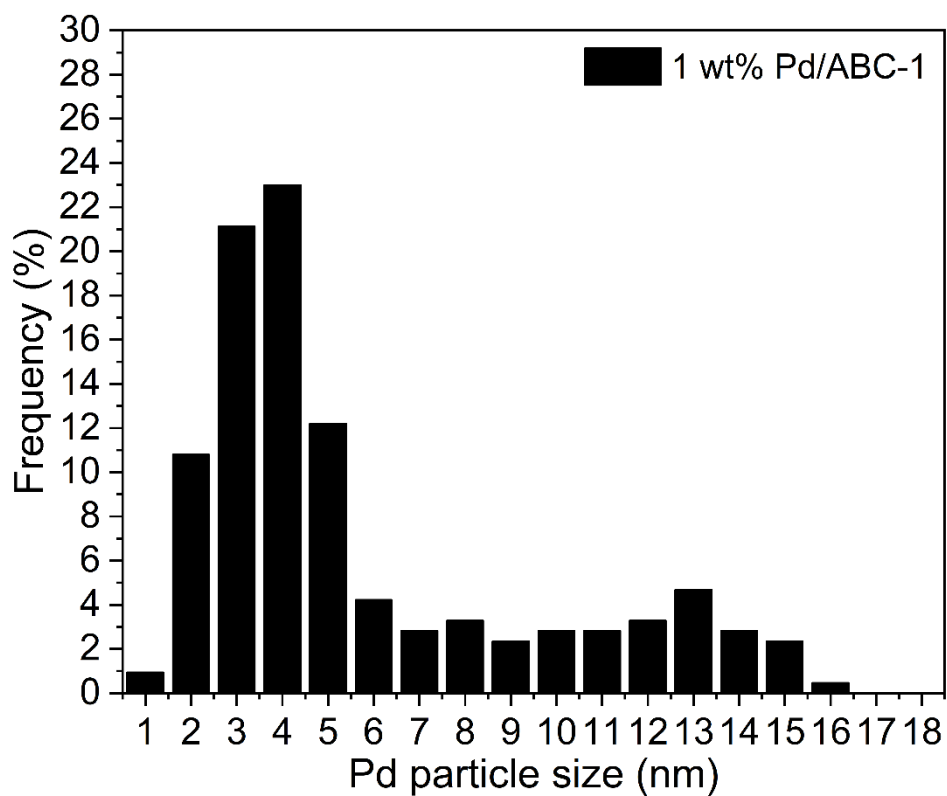


Figure 55: Histogram for measured Pd particle sizes for Pd/ABC-1

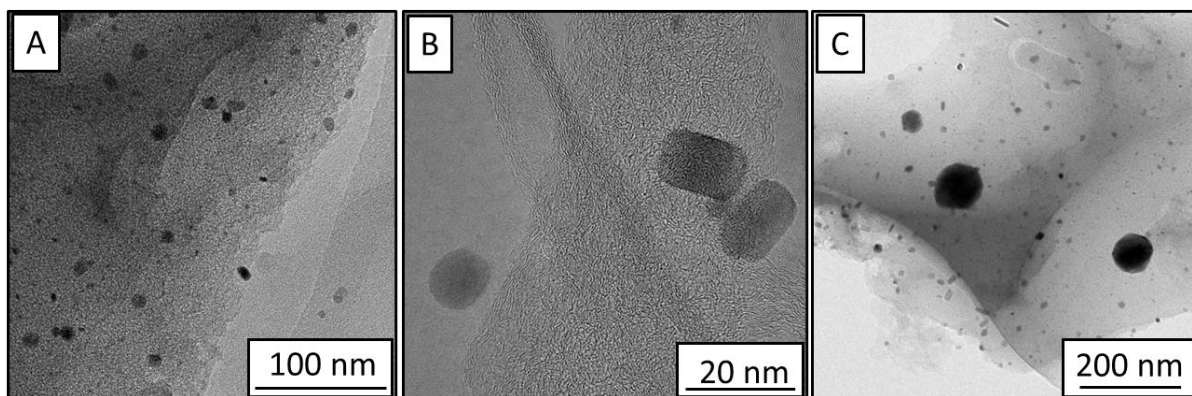


Figure 56: Representative TEM images of Pd/ABC-0.25 at varying magnification (Image A, B and C) to show particle dispersion and agglomerates.

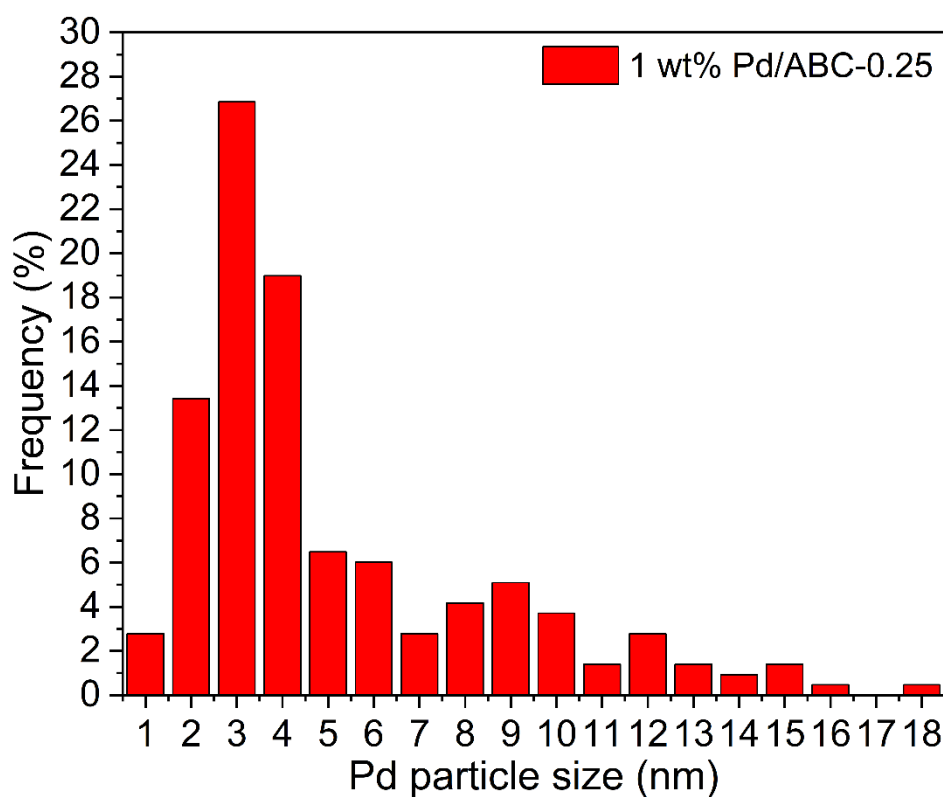


Figure 57: Histogram for measured Pd particle sizes for Pd/ABC-0.25

A complete summary of the data shown in **Chapter 3** can be found in **Section 3.6 (Table 16)** and can be used as a reference point for the characterisation acquired and analysed for the four families of materials created in this thesis, including the bare biochars and Pd impregnated variants.

3.6 Bulk and mesoporous biochar data repository

Table 17: Summary of all characterisations performed, across all samples.

Material	C (%)	H (%)	N (%)	Ash (wt%)	Surface Area (m ² g ⁻¹)	Pore Volume (cm ³ g ⁻¹)	Pore size (nm)	Pd (wt%)	Pd size (XRD) (nm)	Pd size (TEM) (nm)
500 °C	74.93	3.21	0.65	-	Bulk	N/A	N/A	-	-	-
600 °C	78.92	2.22	1.27	-	Bulk	N/A	N/A	-	-	-
700 °C	79.37	1.46	0.55	-	Bulk	N/A	N/A	-	-	-
800 °C	75.59	1.68	1.48	11.14	Bulk	N/A	N/A	-	-	-
ABC-1	71.26	0.83	1.24	12.61	1436.81	0.36	3.90	-	-	-
ABC-0.5	69.49	1.52	1.22	7.35	1392.87	0.41	6.60	-	-	-
ABC-0.25	79.13	1.79	1.19	4.99	1095.23	0.17	4.20	-	-	-
Pd/BC500	45.07	1.51	0.45	12.99	Bulk	N/A	N/A	0.69 ± 0.32	7.99	6.30 ± 3.22
Pd/BC600	74.38	2.12	0.66	16.16	Bulk	N/A	N/A	0.71 ± 0.47	8.20	6.31 ± 3.38
Pd/BC700	78.85	1.96	0.56	11.76	Bulk	N/A	N/A	0.70 ± 0.30	8.75	6.23 ± 2.72
Pd/BC800	75.51	1.43	1.63	11.96	Bulk	N/A	N/A	0.64 ± 0.18	9.40	7.48 ± 4.03
Pd/ABC-1	75.40	0.00	1.22	18.70	1329.31	0.38	4.30	0.29 ± 0.17	12.09	5.75 ± 3.75
Pd/ABC-0.5	85.60	0.82	1.22	17.16	1368.82	0.49	3.90	0.53 ± 0.19	10.05	N/A
Pd/ABC-0.25	75.58	0.82	1.19	4.92	989.00	0.13	3.20	0.21 ± 0.07	7.46	5.29 ± 3.78

Chapter 4

**The selective
hydrogenation of
phenylacetylene using
Pd doped biochars**

4.0 The Selective hydrogenation of phenylacetylene using a bulk and mesoporous biochars.

In this Chapter, I will apply the families of Pd doped biochars (**Chapter 3**) on a model reaction, the selective (or partial) hydrogenation of an alkyne, specifically phenylacetylene. As shown in **Figure 5**, this reaction is subject to a cascade process where further hydrogenation is often seen, resulting in the consumption of the molecule of interest (alkene) and producing the alkane. Conventional catalytic routes have often used materials which can self-poison or prevent the re-adsorption of the alkene by providing a site for surface adsorption. This can also involve using a surface which prevents the parent alkyne from adsorbing in a planer fashion (**Figure 6**). The rationale for accommodating biochars produced through varying conditions (temperature or pre/post activation) will determine if a biorenewable catalyst support can be used to alter the reaction profile of the reaction, without the need to incorporate ad-atoms or additional components which have been used in the past such as Pb or Sn. In a sustainable world, by omitting the use of these metals will reduce the environmental impact of the chemistry as the risk of heavy metal leaching is removed.

4.1 Bulk biochar catalyst hydrogenation reactions

In a stepwise method, the biochars where investigated separately and denoted in two sections as “batch char” which led to the naming of ‘**BC**’ and “activated biochar” which is mentioned as ‘**ABC**’. By taking a systematic approach to this testing, the four bulk BC materials (Pd/BC500, Pd/BC600, Pd/BC700 and Pd/BC800) were utilised at three different temperatures to determine the most effective reaction conditions, and where possible calculate the required activation energy per materials. As shown in **Chapter 3**, the family of BC materials are very low surface area, this means that the dispersion of Pd on the surface will be very low. With that in mind, it can be assumed that either the rate of reaction will be low or the high population of

adsorption sites can lead to over conversion or the over population of activated hydrogen post spillover onto the support from the Pd.

4.1.1 Bulk biochar reactions at 30 °C

With relation to **Figure 58a**, we can see that after six hours (360 min) that the produced materials were confirmed as catalysts for this reaction, evidenced through catalytic turnover leading to a two-stage process, hydrogen activation and bond saturation in the phenylacetylene. The data in **Table 18** shows that Pd/BC500 and Pd/BC800 did not fully convert the phenylacetylene. For the case of Pd/BC500, only 47.94% is converted and for Pd/BC800 only 89.48% was converted, albeit at 100% and 92.30% selectivity to styrene, respectively. However, Pd/BC600 was found to be more active, converting all the phenylacetylene (~100%) after 300 min, providing a modest selectivity of 85.47% towards styrene. Finally, Pd/BC700 appeared to be the most active catalyst as it fully consumed the phenylacetylene after 240 min which is the fastest of the four catalysts at 30 °C, however this was by far the least selective (69.50%), leading to steady consumption of the styrene once the phenylacetylene had been transformed. The trends in reaction selectivity can be found in **Table 18** and **Figure 59b** which shows when styrene begins to be consumed, per catalyst and **Figure 59c** shows the evolution of ethylbenzene as a result of the styrene consumption. An initial deduction can be made for these catalysts, suggesting that there is early evidence that while the Pd content is similar across the materials (**Table 11**), there is an effect of pyrolysis across the biochars, loosely inferring that the catalysts have variable adsorption properties or the promotional effect to the hydrogenation reaction is attributed to an increase in Lewis acid characteristics (evidenced through FTIR. **Figure 29**). With the exception to Pd/BC800 which at this point appears an outlier, the stepwise trend from BC500-BC700 show an increase in Lewis acid content (**Figure 29**), highlighting not only a more rapid initial reaction to styrene, a greater rate of hydrogen cascade reaction to ethylbenzene. This is evidenced in **Figure 58c** which shows the runaway

reaction occurring from 240 min and 120 min, for Pd/BC600 and Pd/BC700, respectively. However, the second hydrogenation reaction was detected at 240 min for Pd/BC800, similar to Pd/BC600.

With this in mind, the data shows that for 30 °C, Pd/BC500 is the most selective, albeit least active catalyst. Clearly, as the support pyrolysis temperature was increased, the selectivity seen for BC500 was sacrificed at a cost of activity for BC600, BC700 and BC800.

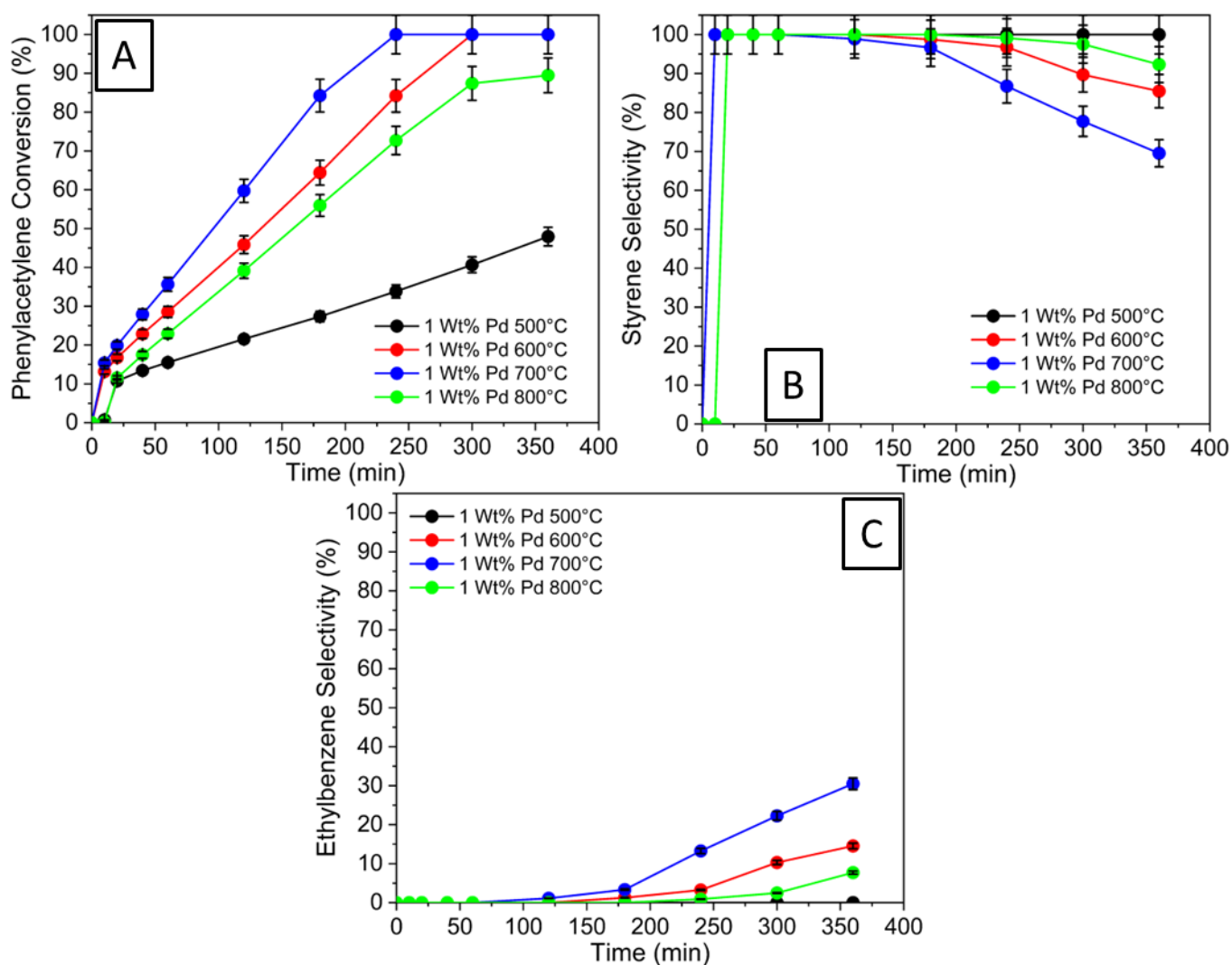


Figure 58: [A] conversion of phenylacetylene at 30 °C. [B] Selectivity of styrene and [C] Selectivity for ethylbenzene for Pd/BC500, Pd/BC600, Pd/BC700 and Pd/BC800

Table 18: Table showing the conversion of Phenylacetylene, Selectivity for styrene and ethylbenzene for Pd/BC500, Pd/BC500, Pd/BC500 and Pd/BC500 at 30°C.

Catalyst	Reaction Temperature (°C)	Phenylacetylene Conversion (%)	Styrene Selectivity (%)	Ethylbenzene Selectivity (%)
Pd/BC500	30	47.94	100.00	0.00
Pd/BC600		100.00	85.47	14.53
Pd/BC700		100.00	69.50	30.50
Pd/BC800		89.48	92.30	7.70

4.1.2 Bulk biochar reaction at 50 °C

To investigate the effect of temperature on this reaction, a strategic increase to 50 °C was implemented, maintaining the same mass of catalyst and flow rate of hydrogen through the solution. **Figure 59a** and **Table 19** both show that for Pd/BC500, the reactivity has increased due to more energy supplied to the reaction. At this mildly elevated temperature 88.33% of the phenylacetylene was converted to both styrene and ethylbenzene, demonstrating that selectivity was not maintained in the same way as at 30 °C. However, shown in **Table 18**, only 47.94% was converted overall, by increasing the temperature the conversion increased by a substantial 45.73%, albeit now reporting a styrene selectivity of 95.55%, in this case the styrene was beginning to be consumed at ~300 min (**Figure 59b** and **Figure 59c**). For Pd/BC600, the effect of temperature was not as profound as a similar reactivity was observed, the phenylacetylene was found to reach the same level of conversion (~100%) at a similar time as the 30 °C data. Interestingly, the selectivity of styrene production for this catalyst was higher for the 50 °C reaction, where 93.48% was found, compared with 85.47% for the lower temperature reaction (**Table 18**). The reactivity for Pd/BC700 operated in the same way as seen for Pd/BC500 where the temperature drove the reaction to fully convert phenylacetylene 120 min, this is half the time required for the 30 °C reaction. However, as is also expected, this accelerated rate of reaction also drove the over hydrogenation to ethylbenzene, resulting in a

change of styrene selectivity from 69.50% (30 °C, **Table 18**) to 63.64% (50 °C, **Table 19**). In a similar fashion, the reactivity also increased for Pd/BC800, evidenced in **Figure 59a** the catalyst fully converted the phenylacetylene after 240 min, whereas at 30 °C it only managed to convert 89.48 %, with near identical selectivity towards styrene, 92.30% and 92.65% for 30 °C and 50 °C, respectively (**Table 17, Table 18**), meaning similar ethylbenzene selectivity too.

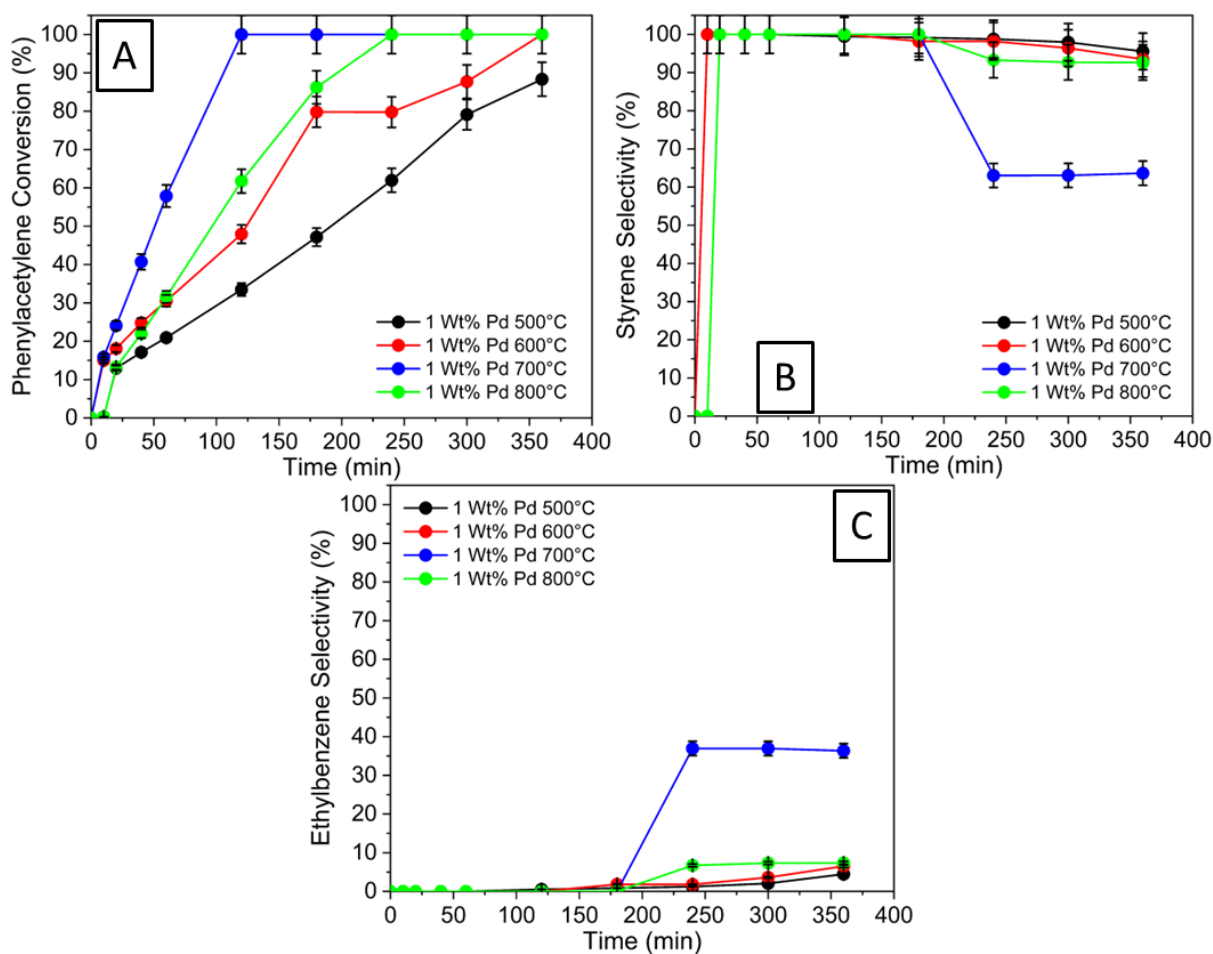


Figure 59: [A] conversion of Phenylacetylene at 50 °C. [B] Selectivity of Styrene at 50 °C and [C] Selectivity for Ethylbenzene at 50 °C 1 wt% BC/500, 1 wt% BC/600, 1 wt% BC/700 and 1 wt% BC/800

To fully deduce the requirement of Pd in this reaction, although hydrogenation has previously been stated as requiring activation via a metal site, the potential for auto-hydrogenation is possible as well as rogue inorganic components of the biochar facilitating both reactions, or

through possible transfer hydrogenation reactions in the alcohol solvent. **Table 19** also shows the phenylacetylene hydrogenation reaction in the presence of the BC support materials alone, tested using the same material mass input, hydrogen flow rate and 50 °C. The data clearly shows there was no observable reaction for this family of Pd free materials, therefore this reaction is solely dependent on the addition of Pd as the catalytic sites. As the supports have been found to drive reaction selectivity, the minimum necessary requirement for both hydrogen activation and the follow-on hydrogen atom utilisation is through an impregnated active site, when operating under an ambient pressure reaction. An increased pressure could facilitate the reactions subtly if a relevant ash-based component could drive the reactions.

Table 19: Conversion of Phenylacetylene, Selectivity for styrene and ethylbenzene for Pd/BC500, Pd/BC600, Pd/BC700 and Pd/BC800 at 50°C, comparing with Pd free BC supports.

Catalyst	Reaction Temperature (°C)	Phenylacetylene Conversion (%)	Styrene Selectivity (%)	Ethylbenzene Selectivity (%)
Pd/BC500	50	88.33	95.55	4.45
Pd/BC600		100.00	93.48	6.52
Pd/BC700		100.00	63.64	36.36
Pd/BC800		100.00	92.65	7.35
BC500	50	0	N/A	N/A
BC600		0	N/A	N/A
BC700		0	N/A	N/A
BC800		0	N/A	N/A

4.1.3 Bulk biochar reaction at 70 °C

The final temperature used for these reactions was 70 °C, still below the boiling points of the solvent, ethanol (78 °C), therefore this reaction remains exclusively in the liquid phase. Assuming the Pd free reactions to operate in an identical manner at 50 °C, they were not ran for the higher temperature reaction.

For Pd/BC500, **Figure 60a** shows that the core hydrogenation reaction has been retarded by an increase in temperature. **Table 19** shows that we can see that the conversion of phenylacetylene

reduced from 88.33% to 52.25% (**Table 20**), an overall decrease of 40.85%. However, at this reduced conversion, the selectivity towards ethylbenzene was eliminated meaning that the reaction operated similarly to 30 °C, with a marginal increase to the conversion after 360 min. **Figure 60a** also shows for Pd/BC600 that the catalyst has fully converted the phenylacetylene after 300 min, an improvement over the 50 °C reaction which reached full conversion at 360 min. However, the selectivity towards styrene was radically reduced to 87.47%, this reaction began to produce ethylbenzene after 180 min, quicker than other reactions using this catalyst at lower temperatures. With regards to Pd/BC700, the phenylacetylene also fully converted after 180 min at 70 °C (**Figure 60a**), this was in fact a reduction in activity as compared to 50 °C (**Figure 59a**) where total conversion takes place at 120 min. Finally, for the Pd/BC800 catalyst the addition of the extra energy has not affected the conversion of phenylacetylene as reaction ran identically at both 50 and 70 °C.

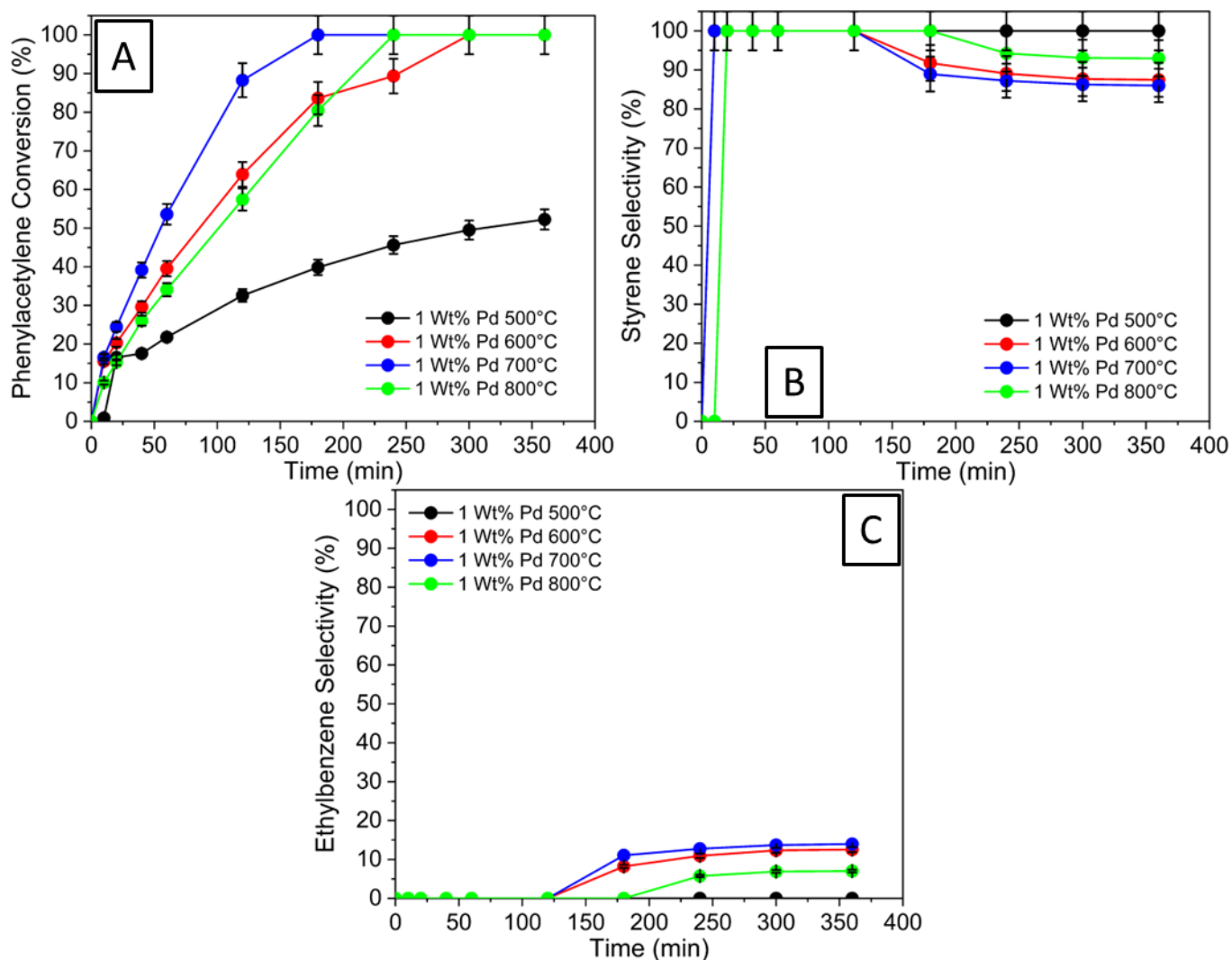


Figure 60: [A] conversion of Phenylacetylene at 50 °C. [B] Selectivity of Styrene at 50 °C and [C] Selectivity for Ethylbenzene at 50 °C 1 wt% BC/500, 1 wt% BC/600, 1 wt% BC/700 and 1 wt% BC/800

Table 20: Table showing the conversion of Phenylacetylene, Selectivity for styrene and ethylbenzene for 1 wt% Pd/BC500, 1 wt% Pd/BC500, 1 wt% Pd/BC500 and 1 wt% Pd/BC500 at 70°C.

Catalyst	Reaction Temperature (°C)	Phenylacetylene Conversion (%)	Styrene Selectivity (%)	Ethylbenzene Selectivity (%)
Pd/BC500	70	52.25	100	0
Pd/BC600		100	87.47	12.53
Pd/BC700		100	86.02	13.98
Pd/BC800		100	92.98	7.02

4.1.4 Initial rate for Bulk biochar reaction

Up to this point, the reaction/catalyst analysis has been relatively basic. In this way only the core conversion and selectivity towards the specific products were monitored. A deeper analysis of the catalyst can be carried out in terms of their performance, especially after the elucidation that Pd was a minimum necessary requirement for catalytic turnover (**Table 18**), a detailed sample of the kinetics can be seen in **Appendix 1**. By measuring the initial rate of reaction, the fastest section of the reaction over the first hour, and dividing by the true mass of Pd in the reaction (the Pd loading in a single 30 mg catalyst charge) the normalised initial rates of reaction can then be mapped to the specific temperatures. The data presented in **Figure 61** and **Table 21** suggests that for Pd/BC500, there is no advantage (in terms of rate) to increase the reaction temperature past 50 °C. However, this is not echoed by the other catalysts as temperature was found in each case to accelerate the rate of reaction. **Figure 61** shows that the logical stepwise increase in temperature benefits each reaction's rate, irrespective of the overall phenylacetylene conversion mentioned above. This means that for 70 °C, the physical catalytic turnover for the Pd nanoparticles is higher across the board, with the exception of Pd/BC700 which appears to not follow this trend. The deviation in rate of reaction for this catalyst could be an anomaly, it is expected that this would deduced upon further repeat reactions. What is interesting from this data is that for 30 °C, (much like 70 °C), there is a volcano plot visible. This centres on Pd/BC700, indicating that the catalyst is the most effective for physical catalytic turnover. One may suggest that the Pd/BC800 has less available Pd but the normalisation to the data omits this factor by dividing the rate by the metal present. Therefore, in terms of raw reaction capability over the first hour it is clear that Pd/BC700 is the best performing, albeit clearly not the most selective, this would be Pd/BC600.

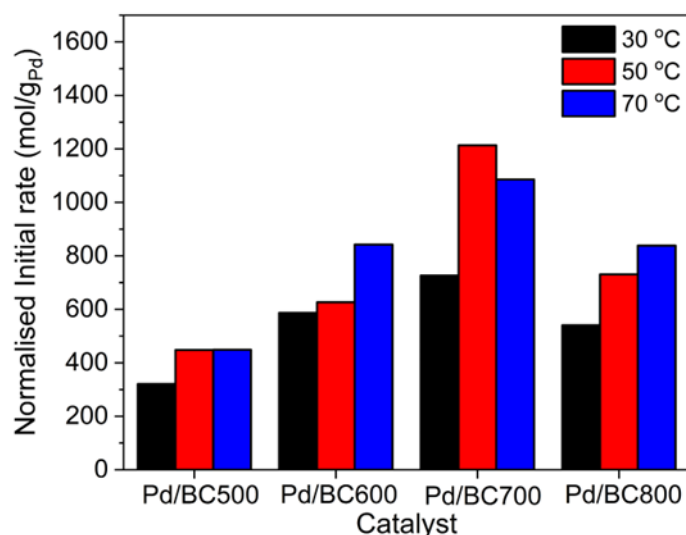


Figure 61: Initial rate of reaction for Pd/BC500, Pd/BC600, Pd/BC700 and Pd/BC800 at 30 °C 50 °C and 70 °C

4.1.5 Reaction activation energy for the Pd/BC catalysts

Again, to analyse the physical properties of each catalyst. One can calculate the true benefit for the catalyst itself by considering its reaction activation energy. This can be accomplished by utilising the initial reaction rates (phenylacetylene concentration change in the first hour) across the various temperatures used (**Table 21**), these values were then substituted into **Equation 12**, the Arrhenius Equation. To work this out you must take the natural log of the measured reaction rate resulting in **Equation 13**, from here **Equation 14** is used which is modelled around the $y = mx + c$ equation for a linear plot, by multiplying the gradient by the universal gas constant, an activation energy in Joules is calculated.

$$k = Ae^{\frac{-E_a}{RT}} \quad \text{Equation 12}$$

Where:

- k = rate constant
- A = pre-exponential factor
- e = base of the natural logarithm
- E_a = activation energy

- R = universal gas constant
- T = absolute temperature

$$\ln k = \ln A - \frac{E_a}{RT} \quad \text{Equation 13}$$

$$\text{gradient} = -\frac{E_a}{R} \quad \text{Equation 14}$$

From the literature we can see that the calculated activation energy for the hydrogenation of phenylacetylene has been found to be between 23.2-53.6 kJ mol⁻¹^{99, 105}. However, in this work, **Table 21** shows that for the bulk series of catalysts the activation energy is significantly lower than that of the literature. The values in this work range as follows; 7.38 kJ mol⁻¹, 7.68 kJ mol⁻¹, 8.95 kJ mol⁻¹ and 9.53 kJ mol⁻¹ for Pd/BC500, Pd/BC600, Pd/BC700 and Pd/BC800, respectively. It is clear that as the pyrolysis temperature is increased for the support, the activation energy required also increases.

Table 21: shows the initial rate for as well as the activation energy for Pd/BC500, Pd/BC600, Pd/BC700 and Pd/BC800

Catalyst	T (°C)	T (K)	1/T	rate (mol h ⁻¹)	Ln (rate)	Gradient	Ea (J mol ⁻¹)	Ea (kJ mol ⁻¹)
Pd/BC500	30	303	0.0033	0.0673	-2.6983	-887.54	7379.00	7.38
	50	323	0.0031	0.0941	-2.3632			
	70	343	0.0029	0.0941	-2.3632			
Pd/BC600	30	303	0.0033	0.1233	-2.0931	-923.35	7676.73	7.68
	50	323	0.0031	0.1316	-2.0283			
	70	343	0.0029	0.1769	-1.7325			
Pd/BC700	30	303	0.0033	0.1525	-1.8805	-1076.10	8946.70	8.95
	50	323	0.0031	0.2548	-1.3673			
	70	343	0.0029	0.2279	-1.4787			
Pd/BC800	30	303	0.0033	0.0974	-2.3293	-1146.50	9532.00	9.53
	50	323	0.0031	0.1316	-2.0283			
	70	343	0.0029	0.1509	-1.8909			

4.2 Mesoporous biochar catalyst hydrogenation reactions

Following the bulk Pd doped biochars, the mesoporous materials, derived from activated biochars, denoted as Pd/ABC-1, Pd/ABC-0.25 and Pd/ABC-0.5, were screened using the same conditions as the bulk catalysts. It is envisaged that the mesoporous materials will facilitate the catalytic reaction at higher rate than the bulk counterparts. This is due to the increased available surface area and dispersion of Pd nanoparticles, as a result allowing Pd that would not be able to partake in the reaction before to undergo catalytic turnover. Albeit, the data in **Chapter 3** does show that for the EDX sweeps that were carried out, the Pd loading is subtly lower than the bulk catalysts. Again, this is postulated to be a matter of dispersion and the EDX scans ran were not of high enough frequency. For the TEM, **Table 16** shows that the measured particle sizes are within error of the bulk counterparts, and therefore any differences to activity and selectivity cannot be attributed to variation in Pd particle size.

4.2.1 Mesoporous biochar reaction at 30 °C

With relation to **Figure 62a**, after 360 min, the Pd doped mesoporous materials were confirmed as catalysts for this reaction. The data in **Table 22** shows that Pd ABC-1, Pd ABC-0.5 and Pd ABC-0.25 did not fully convert the phenylacetylene at 30 °C. At this temperature, phenylacetylene transformation was found to be; 89.65%, 89.98% and 38.41% for Pd/ ABC-1, Pd/ABC-0.5 and Pd/ABC-0.25, respectively. Interestingly, these catalysts presented a modest selectivity towards styrene of 92.09%, 86.15% and 99.47%, this means that although Pd/ABC-0.25 had the lowest overall conversion, it was the most selective, while the Pd/ ABC-1 catalyst proved to be both highly active and selective. In comparison with the bulk material, Pd/BC800, which can be used as the benchmark catalyst due to the same pyrolysis temperature used and potentially same level of Lewis acidity, 89.48% and 92.30% were seen for conversion and selectivity, respectively. This means that the bulk material operated subtly less active, but more selective than the Pd/ABC-1 catalyst. However, the bulk material proved to be far superior in

terms of phenylacetylene conversion and styrene selectivity than Pd/ABC-0.25. This could be assumed that there has been some level of pore blockage or diffusion limitation induced during the reaction, retarding the turnover.

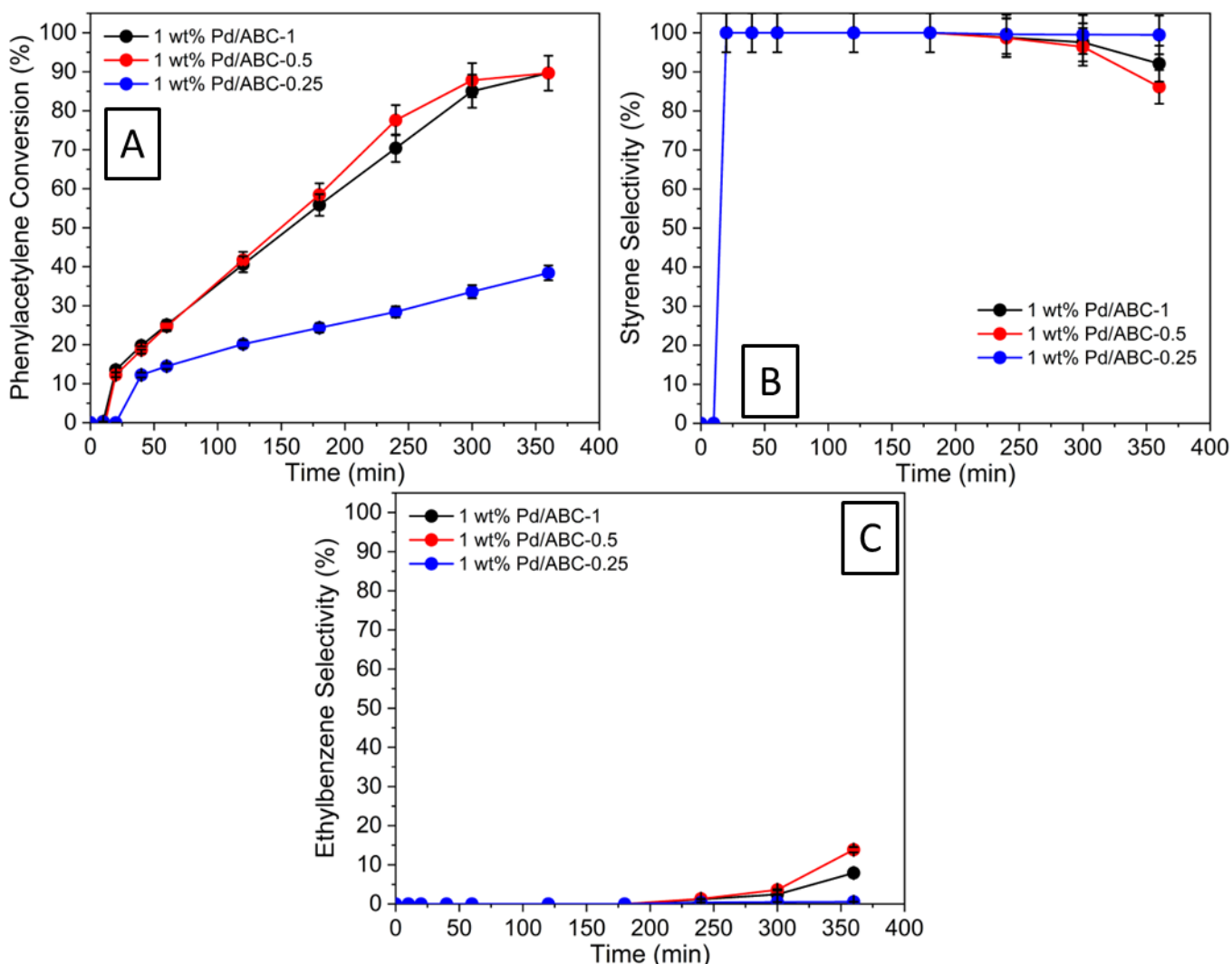


Figure 62: [A] conversion of Phenylacetylene at 30 °C. [B] Selectivity of Styrene at 30 °C and [C] Selectivity for Ethylbenzene at 30 °C for Pd/ABC-1, Pd/ABC-0.5 and Pd/ABC-0.25

Table 22: Table showing the conversion of Phenylacetylene, Selectivity for styrene and ethylbenzene for Pd/ABC-1, Pd/ABC-0.5 and Pd/ABC-0.25 at 30 °C

Catalyst	Reaction Temperature (°C)	Phenylacetylene Conversion (%)	Styrene Selectivity (%)	Ethylbenzene Selectivity (%)
Pd/ABC-1	30	89.65	92.09	7.91

Pd/ABC-0.5	89.98	86.15	13.85
Pd/ABC-0.25	38.41	99.47	0.53

4.2.2 Mesoporous biochar reaction at 50 °C

Again, as with the bulk catalysts, the effect of temperature was screened for this reaction via the same stepwise increase to 50 °C. **Figure 63a** and **Table 23** both show that for Pd/ABC-0.25, the reactivity increased due to more energy supplied to the reaction to 48.70% of the phenylacetylene was converted to both styrene and ethylbenzene. For Pd/ABC-1 and Pd/ABC-0.5 the extra energy input resulted in a reduction of the conversion of phenylacetylene to styrene and ethylbenzene this is shown in **Tables 22 and 23** as Pd/ABC-1 goes from a conversion of 89.65 % to 87.81 % a reduction of 2.05% and for Pd/ABC-0.5 goes from a conversion of 89.65 % to 86.38 % a reduction of 3.65%. For Pd/ABC-1 and Pd/ABC-0.5, due to the increased temperature both presented a 2.05% decrease in selectivity where ethylbenzene began to increase. These changes to phenylacetylene conversion and resulting product selectivities proved to be starkly different than the Pd/BC800 benchmark material. Here, **Table 18** shows that the increase in input temperature promoted conversion by 10.52%. The bulk catalyst also presented styrene selectivity at 92.65%, this is higher than the full family of mesoporous catalysts. However, this is just the end point conversions scrutinised, further into this chapter the true catalyst performances will be probed. Especially due to the lower Pd content reported. Up to this point, both Pd/ABC-1 and Pd/ABC-0.5 appear to operate in a very similar manner, their textural properties are nearly identical as well. The striking differences are the reported Pd content, which was seen to be higher for Pd/ABC-0.5. If the materials are similar, on an industrial outlook, the Pd/ABC-0.5 catalyst would be favoured due to a marginally lower cost of production (lower KOH overhead needed).

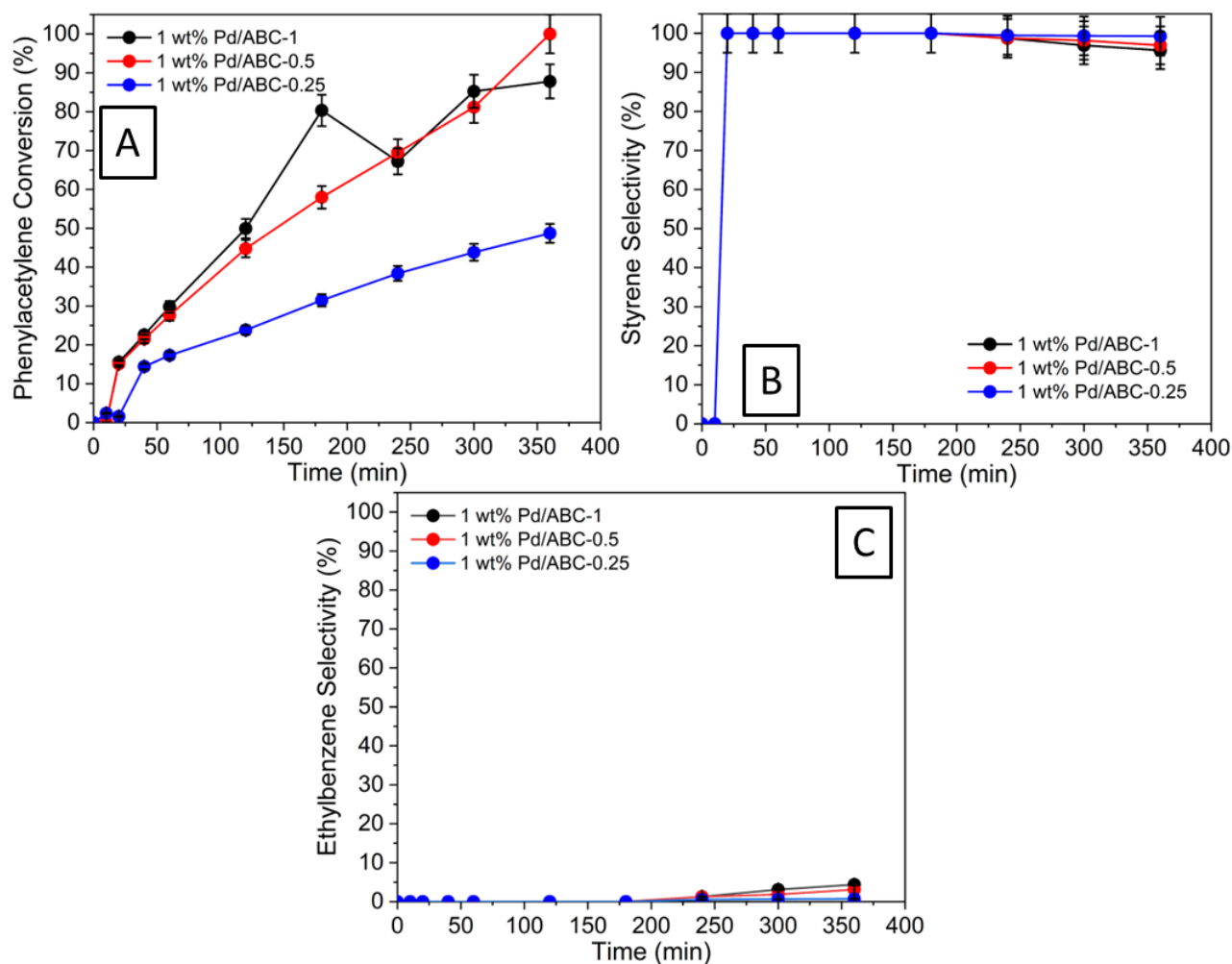


Figure 63: [A] conversion of Phenylacetylene at 50 °C. [B] Selectivity of Styrene at 50 °C and [C] Selectivity for Ethylbenzene at 50 °C for Pd/ABC-1, Pd/ABC-0.5 and Pd/ABC-0.25

Table 23: Table showing the conversion of Phenylacetylene, Selectivity for styrene and ethylbenzene for Pd/ABC-1, Pd/ABC-0.5 and Pd/ABC-0.25 at 50 °C.

Catalyst	Reaction Temperature (°C)	Phenylacetylene Conversion (%)	Styrene Selectivity (%)	Ethylbenzene Selectivity (%)
Pd/ABC-1	50	87.81	95.63	4.37
Pd/ABC-0.5		86.38	96.90	3.10
Pd/ABC-0.25		48.70	99.27	0.73

4.2.3 Mesoporous biochar reaction at 70 °C

The final temperature used for these reactions was 70 °C. With respect to the conversion of phenylacetylene, the additional energy used has resulted in a greater phenylacetylene

conversion for Pd/ABC-1 and Pd/ABC-0.25 at 100 % and 54.92 %, respectively after 360 min (**Table 24**). This is an increase of 12.19 % and 11.33 % respectively from the reactions at 50 °C (**Table 23**). In a similar fashion to this data, the reactions at 70 °C performed likewise with respect to selectivity. **Table 24** shows that the selectivity of styrene decreased again, slightly from 95.63% to 94.37% for Pd/ABC-1, 96.90 % to 92.35% for Pd/ABC-0.5 and 99.27% to 99.08% for Pd/ABC-0.25. As one would expect, by decreasing styrene selectivity marginally, there is a mirrored increase in ethylbenzene selectivity. However, styrene selectivity are far superior for the ABC catalysts compared with the BC counterparts when operating at the same temperature. Taking the benchmark material of Pd/BC800, although the conversion remains at 100% (mapping effectively to Pd/ABC-1 and Pd/ABC-0.5), the selectivity is relatively low at 92.98% towards styrene. This value is much lower than Pd/ABC-1 (94.37%) and Pd/ABC-0.25 (99.08%), albeit for the case of Pd/ABC-0.25 the catalytic conversion was shown to be stunted for the full range of reaction. This could mean that the material was either deficient, problematic or perhaps just needed to be resynthesized.

Ultimately, in terms of pure catalytic conversion and styrene selectivity, the mesoporous catalysts were not beneficial in the grand scheme. By looking only at the 360 min time point, they are very similar to the bulk Pd/BC800 benchmark catalyst, albeit with some variation to reaction selectivity. Also, unlike the bulk counterparts where reaction and selectivity were seen to change linear with respect to temperature, the mesoporous catalysts obey a less linear approach where the reaction at 50 °C seems to be an experimental outlier or the full range.

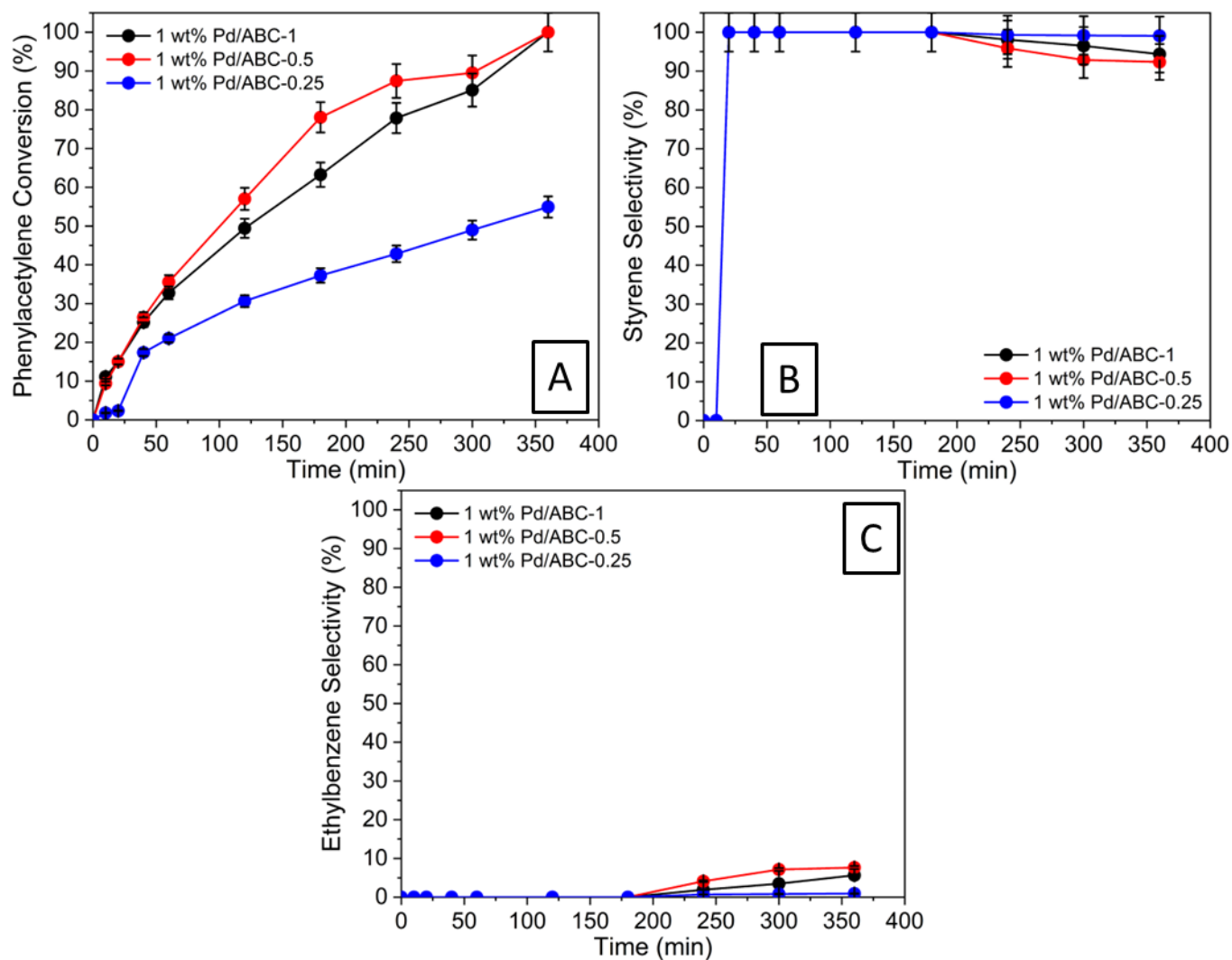


Figure 64: [A] conversion of Phenylacetylene at 70 °C. [B] Selectivity of Styrene at 70 °C and [C] Selectivity for Ethylbenzene at 70 °C for Pd/ABC-1, Pd/ABC-0.5 and Pd/ABC-0.25

Table 24: Table showing the conversion of Phenylacetylene, Selectivity for styrene and ethylbenzene for Pd/ABC-1, Pd/ABC-0.5 and Pd/ABC-0.25 at 70 °C

Catalyst	Reaction Temperature (°C)	Phenylacetylene Conversion (%)	Styrene Selectivity (%)	Ethylbenzene Selectivity (%)
Pd/ABC-1	70	100.00	94.37	5.63
Pd/ABC-0.5	70	100.00	92.35	7.65
Pd/ABC-0.25	70	54.92	99.08	0.92

4.2.4 Initial rate for mesoporous biochar reaction

Moving on from single point analysis, one can consider the initial rate of reaction, identically with the bulk support catalysts. By measuring the initial rate of reaction, the fastest section of

the reaction over the first hour and dividing by the true mass of Pd in the reaction (the Pd loading in a single 30 mg catalyst charge) the normalised initial rates of reaction were then mapped to the specific temperatures. The data presented in **Figure 65a** shows that for all three catalysts, there is a logical stepwise increase rate with respect to temperature. Additionally, this linear trend also follows the physical principle that rate will increase as diffusion capabilities increase, observed by Pd/ABC-1 possessing a higher surface area than Pd/ABC-0.5 and Pd/ABC-0.25. **Figure 65b** shows the normalised initial rates from the bulk support catalysts, although possessing a higher quantity of measured Pd, the initial rates were found to all be slower than Pd/ABC-1 which outperformed all other catalysts, across all three temperatures. The full family of mesoporous support catalysts were found to outperform the benchmark Pd/BC800 catalyst, again across the full temperature range studied.

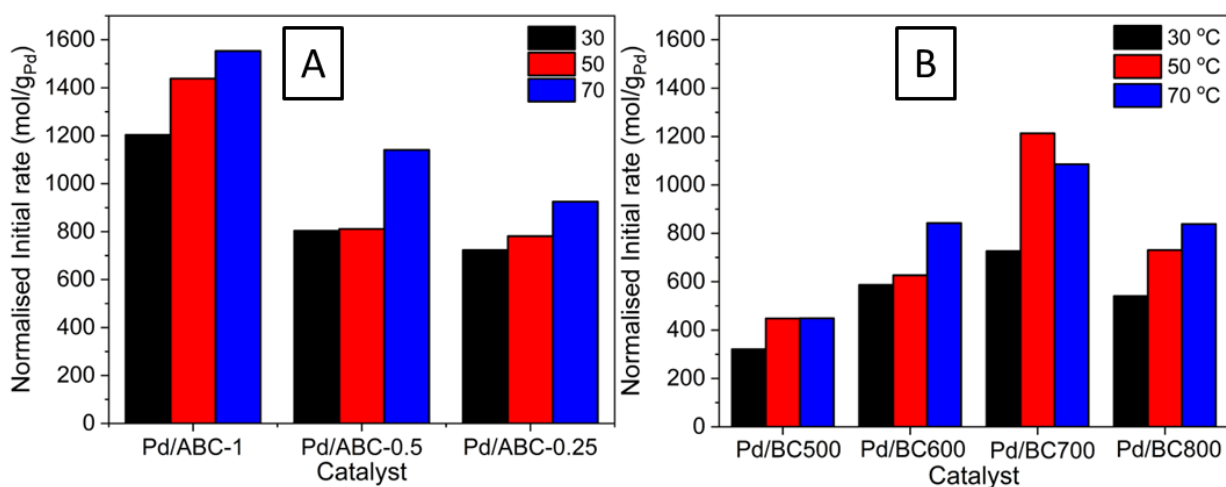


Figure 65: [A] Initial rate of reaction for Pd/ABC-1, Pd/ABC-0.5 and Pd/ABC-0.25 at 30 °C 50 °C and 70 °C. [B] Initial rate of reaction for Pd/BC500, Pd/BC600, Pd/BC700 and Pd/BC800 at 30 °C 50 °C and 70 °C

4.2.5 Reaction activation energy for the Pd/BC catalysts

As can be seen from **Table 25**, from the mesoporous catalysts Pd/ABC-0.5 appears to be the worst in terms of activation energy, due to presenting lower than expected initial rate. As a result the calculated activation energy was found to be 7.41 kJ mol⁻¹, whereas the energies calculated for Pd/ABC-0.25 and Pd/ABC-1 were found to be 5.28 kJ mol⁻¹ and 4.00 kJ mol⁻¹, respectively.

By returning to the bulk support benchmark catalyst, Pd/BC800 was calculated to be 9.53 kJ mol⁻¹, Pd/ABC-1 presents a reduction in the energy required by 58.08% to conduct the phenylacetylene → styrene reaction (as all catalysts proved to be 100% selective at 1 h). Irrespective of the pyrolysis temperature used, one can comfortably state that the mesoporous catalysts exhibited superior rates of reaction over the bulk catalysts, resulting in lowered activation energies. Although Pd/BC500 showed 7.38 kJ mol⁻¹ which is very close to Pd/ABC-0.5 at 7.41 kJ mol⁻¹, the other two catalysts were vastly lower than the bulk supports.

Table 25: Shows the initial rate for as well as the activation energy for Pd/ABC-1, Pd/ABC-0.5 and Pd/ABC-0.25

Catalyst	T (°C)	T (K)	1/T	rate (mol h ⁻¹)	Ln (rate)	Gradient	EA (J mol ⁻¹)	EA (kJ mol ⁻¹)
Pd/ABC-1	30	303	0.0033	0.1083	-2.2227			
	50	323	0.0031	0.0226	-3.7896	-480.58	3995.54	4.00
	70	343	0.0029	0.1398	-1.9675			
Pd/ABC-0.5	30	303	0.0033	0.1205	-2.1157			
	50	323	0.0031	0.1217	-2.1065	-891.72	7413.76	7.41
	70	343	0.0029	0.1711	-1.7653			
Pd/ABC-0.25	30	303	0.0033	0.0651	-2.7321			
	50	323	0.0031	0.0703	-2.6547	-634.48	5275.07	5.28
	70	343	0.0029	0.0833	-2.4857			

4.3 Bulk and mesoporous biochar data repository

As a one stop shop for catalyst screening, **Table 26** shows a full overview of both catalyst families, presenting both conversion and reaction selectivities for all catalyst operating at the various temperature.

Table 26: An overview of phenylacetylene conversion and reaction selectivities, across all temperatures and catalysts after 360 min.

Catalyst	Reaction Temperature (°C)	Phenylacetylene Conversion (%)	Styrene Selectivity (%)	Ethylbenzene Selectivity (%)
Pd/BC500	30	47.94	100.00	0.00
	50	88.33	95.55	4.45
	70	52.25	100.00	0.00
Pd/BC600	30	100.00	85.47	14.53
	50	100.00	93.48	6.52
	70	100.00	87.47	12.53
Pd/BC700	30	100.00	69.50	30.50
	50	100.00	63.64	36.36
	70	100.00	86.02	13.98
Pd/BC800	30	89.48	92.30	7.70
	50	100.00	92.65	7.35
	70	100	92.98	7.02
Pd/ABC-1	30	89.65	92.09	7.91
	50	22.56	95.63	4.37
	70	100.00	94.37	5.63
Pd/ABC-0.5	30	89.65	86.15	13.85
	50	86.38	96.90	3.10
	70	100.00	92.35	7.65
Pd/ABC-0.25	30	38.41	99.47	0.53
	50	48.70	99.27	0.73
	70	54.92	99.08	0.92

4.4 Pd doped biochars – suggested reaction mechanisms.

Concluding on the reactivity of both families of Pd doped biochars, a schematic is shown in **Figure 66**. This highlights both families of materials, the BC range being a bulk material with low surface area, as a result low Pd surface dispersion. By holding a low Pd dispersion, it is

assumed that there is crowding on the surface of the catalyst, especially in terms of activated hydrogen (post dissociation). It is theorised that the hydrogen excess will cause a runaway or cascade reaction on the surface, over hydrogenating styrene as it is being produced or through re-adsorption due to the high Pd surface concentration. **Figure 66** also shows the ABC material which reports high surface area, with low Pd content (EDX). This was assumed to be due to high dispersion throughout the material. This has now been aligned with the lower ethylbenzene selectivity due to a lower concentration of surface activated hydrogen or localised Pd adsorption sites for styrene to re-adsorb.

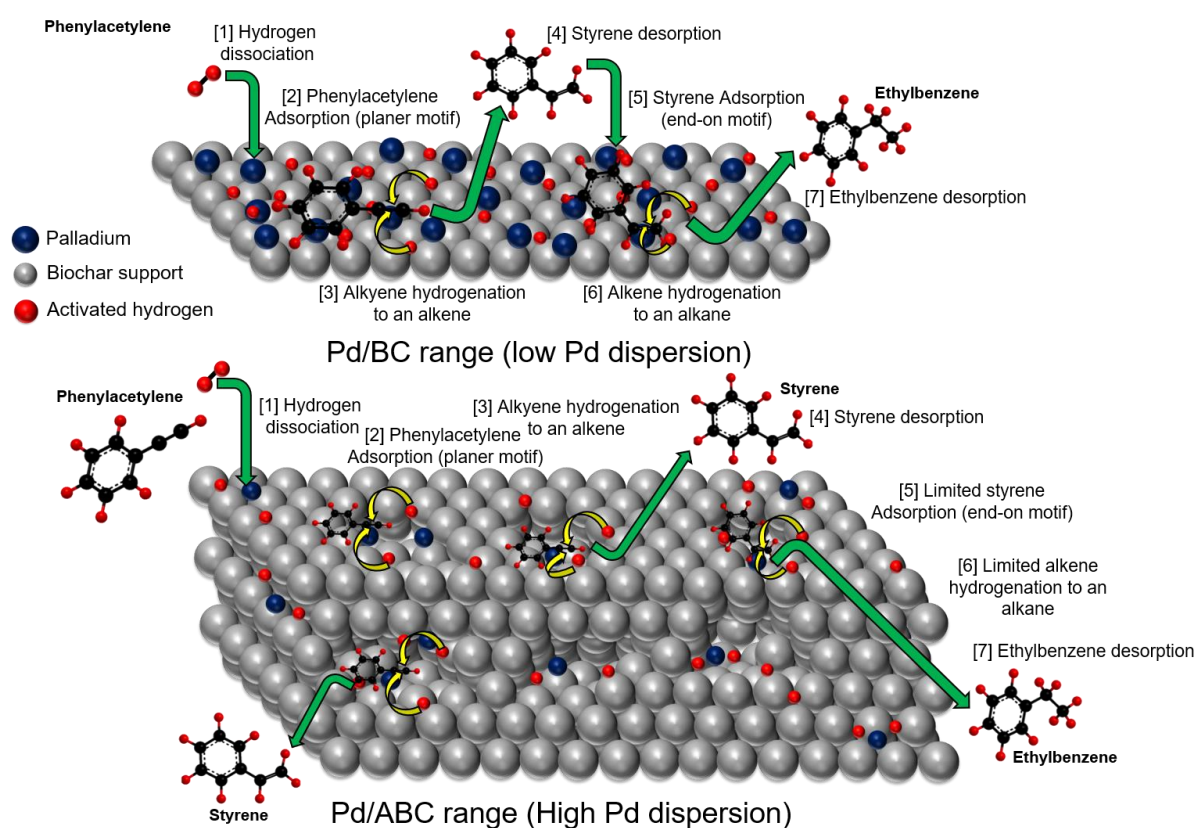


Figure 66: Proposed reaction mechanisms for both the Pd doped BC and ABC families.

Chapter 5

**Conclusions and
Potential Future
Work**

5.1 Conclusions

In conclusion, the work presented in this thesis shows how biochars can be produced from pre-treated lignocellulosic biomass waste, namely barley straw. By starting from a base pyrolysis approach and increasing the maximum temperatures used, a narrative was established that shows how the biochars although appear similar, have different chemical structures. These chemical structures are presented through increases to C=C bond stretching in FTIR at 2800 cm^{-1} , often denoted as induced Lewis acidity. Although this work has not quantified such acidity, routes to investigate this could be ammonia TPD or the adsorption of pyridine/propylamine followed by thermogravimetric analysis. The resulting mass loss can be integrated and used to determine the Lewis acid density of the catalyst. Previously, the wider literature has suggested that this acidity promotes hydrogenation reactions but doesn't specify whether this is a case for activity or reaction selectivity. This work has found that it is indeed activity, where the biochars produced at $500\text{ }^{\circ}\text{C}$, $600\text{ }^{\circ}\text{C}$, $700\text{ }^{\circ}\text{C}$ and $800\text{ }^{\circ}\text{C}$, showed how the rate of phenylacetylene hydrogenation could be increased. It was found that the benefit to activity was maximised for the BC700 material ($700\text{ }^{\circ}\text{C}$), albeit caused a substantial loss in reaction selectivity by promoting the cascade reaction pathway. This reaction pathway directed the over hydrogenation of phenylacetylene to ethylbenzene, through the consumption of styrene, the desired product. As previously stated, the Lewis acid sites promote hydrogenation reactions. The over conversion was found to be favoured for supports that were pyrolyzed at higher temperatures¹³⁹. As a result of this by dispersing the Pd active sites, which were found to be vital for this reaction, one could negate the cascade reaction. Again, it is acknowledged that dispersion measurements were not conducted in this work but could be deduced through CO chemisorption or x-ray photoelectron spectroscopy to look at the catalyst surface. Indeed, the mesoporous ABC catalyst family, with the exception of a single reaction (Pd/ABC-0.5, $30\text{ }^{\circ}\text{C}$) do not present major selectivities towards ethylbenzene. Potentially due to the expanded

surface areas of these materials; 1329 m² g⁻¹, 1368 m² g⁻¹ and 989 m² g⁻¹ for Pd/ABC-1, Pd/ABC-0.5 and Pd/ABC-0.25, respectively vs unmeasurable bulk materials, it is believed that the Pd dispersion is vast. This means that unless the surface restricts the re-adsorption of styrene (not a planer molecule), the dispersion of Pd could preferentially activate hydrogen and crowd the surface and therefore limit ethylbenzene production. In terms of normalised rates per gram of Pd, the mesoporous catalysts were superior on all front and provide a linear trend of activity vs temperature. An identical trend is seen for the bulk support materials, although to a lesser degree, meaning that the Pd sites present are not conducting catalytic turnovers at the same rate. With respect to the data shown the ABC family of materials were found to be more selective to styrene than their bulk (BC) counterparts. Both families of materials exhibited similar reaction conversions overall. Finally, irrespective of biochar production route, both methods yielded materials which could be impregnated in the same way with Pd and providing nanoparticles (after thermal processing) which are comparable in size (confirmed by HRTEM). Collectively, this work highlights a rational route to sustainable catalysis by accommodating a biorenewable waste stream, barley straw. Although the lignocellulosic feedstock can be variable, through pre and post pyrolysis processing, one can generate highly porous biochars with vast available surface areas. Although the reaction used as catalyst validation approach may not have fully benefitted from the mesoporous catalysts (with the exception of a higher rate, as both bulk and mesoporous catalysts yielded 100% phenylacetylene conversion), it is believed that they will come into their own for more complex catalytic transformations.

5.2 Future Work

Upon completion and reflection of the designed project, it is believed that next steps for possible research directions could contain the following:

- Investigate further ratios of feedstock to KOH to find the optimal mixture to achieve the maximum surface area available.
 - Probe deeper how surface area of the support can be best used to maintain styrene selectivity.
- Take sustainability to the next level by investigating how low the Pd content could be before losing the high rates of reaction and selectivity.
 - If the Pd is critically low, can cheaper and more abundant metals such as Cu or Ni be used either in an alloy for or individual sites to support the reaction? Can the Pd be used to just activate the hydrogen dissociation, allowing the other metals to operate in the absence of hydrogen pressure.
- Finally, are biorenewable feedstocks all similar when it comes to biochar derived support materials?
 - Investigate alternative feedstocks such as coffee waste as well as other waste streams to see how the surface area develops upon activation.
 - Do these materials all present similar Lewis acidities?
 - Can the same level of Pd dispersion be achieved?
- Investigate the recyclability of the catalysts, could the mesoporous materials be beneficial for sustained usage? Would the bulk materials lose activity after the first reaction if there are carbonaceous deposits on the Pd sites?

Chapter 6

References

6.0 References

1. B. Cox, S. Innis, N. C. Kunz and J. Steen, *Communications Earth & Environment*, 2022, **3**.
2. Y. P. Akshata D Metal Catalysts Market by Catalyst Type (Platinum, Ruthenium, Palladium, Titanium, Zinc, Copper, Others), by Applications (Automotive, Petrochemical, Pharmaceutical, Others): Global Opportunity Analysis and Industry Forecast, 2021-2031, <https://www.alliedmarketresearch.com/metal-catalysts-market-A47250>).
3. C. D. Millholland, Industrial Uses Of Catalysts, <https://www.thermofisher.com/blog/materials/characterizing-the-effectiveness-of-industrial-catalysts/#:~:text=Catalysts%20in%20industry,catalysts%20within%20the%20manuf acturing%20process.>).
4. A. Devi, S. Bajar, P. Sihag, Z. U. D. Sheikh, A. Singh, J. Kaur, N. R. Bishnoi and D. Pant, *Bioengineered*, 2023, **14**, 81-112.
5. J. K. Saini, R. Saini and L. Tewari, *3 Biotech*, 2015, **5**, 337-353.
6. R. Chandra, H. Takeuchi and T. Hasegawa, *Renewable and Sustainable Energy Reviews*, 2012, **16**, 1462-1476.
7. M. Taylor, H. Alabdrabalameer and V. Skoulou, *Sustainability*, 2019, **11**.
8. E. Roduner, *Chem Soc Rev*, 2014, **43**, 8226-8239.
9. J. A. Enterkin, K. R. Poepelmeier and L. D. Marks, *Nano Lett*, 2011, **11**, 993-997.
10. M. J. Taylor, S. K. Beaumont, M. J. Islam, S. Tsatsos, C. A. M. Parlett, M. A. Isaacs and G. Kyriakou, *Appl Catal B-Environ*, 2021, **284**.
11. M. J. Taylor, L. J. Durndell, M. A. Isaacs, C. M. A. Parlett, K. Wilson, A. F. Lee and G. Kyriakou, *Appl Catal B-Environ*, 2016, **180**, 580-585.

12. M. J. Islam, M. G. Mesa, A. Osatiashtiani, J. C. Manayil, M. A. Isaacs, M. J. Taylor, S. Tsatsos and G. Kyriakou, *Appl Catal B-Environ*, 2021, **299**.
13. S. K. Johnston, T. A. Bryant, J. Strong, L. Lazzarini, A. O. Ibhaddon and M. G. Francesconi, *Chemcatchem*, 2019, **11**, 2909-2918.
14. R. A. Sheldon and H. V. Bekkum, *Fine Chemicals through Heterogeneous Catalysis*, WILEY-VCH, 2001.
15. R. Ramachandran and R. K. Menon, *International Journal of Hydrogen Energy*, 1998, **23**, 593-598.
16. A. Z. Fadhel, P. Pollet, C. L. Liotta and C. A. Eckert, *Molecules*, 2010, **15**, 8400-8424.
17. I. Cabria, M. J. López, S. Fraile and J. A. Alonso, *The Journal of Physical Chemistry C*, 2012, **116**, 21179-21189.
18. A. Huang, Y. Cao, R. S. Delima, T. Ji, R. P. Jansonius, N. J. J. Johnson, C. Hunt, J. He, A. Kurimoto, Z. Zhang and C. P. Berlinguette, *JACS Au*, 2021, **1**, 336-343.
19. P. Ryabchuk, M. Anwar, S. Dastgir, K. Junge and M. Beller, *Acs Sustainable Chemistry & Engineering*, 2021, **9**, 10062-10072.
20. C. Cravotto, A. S. Fabiano-Tixier, O. Claux, M. Abert-Vian, S. Tabasso, G. Cravotto and F. Chemat, *Foods*, 2022, **11**.
21. M. J. Antal, K. Mochidzuki and L. S. Paredes, *Ind Eng Chem Res*, 2003, **42**, 3690-3699.
22. B. B. Basak, B. Sarkar, A. Saha, A. Sarkar, S. Mandal, J. K. Biswas, H. Wang and N. S. Bolan, *Sci Total Environ*, 2022, **822**, 153461.
23. J. S. Cha, S. H. Park, S.-C. Jung, C. Ryu, J.-K. Jeon, M.-C. Shin and Y.-K. Park, *Journal of Industrial and Engineering Chemistry*, 2016, **40**, 1-15.
24. T. Y. A. Fahmy, Y. Fahmy, F. Mobarak, M. El-Sakhawy and R. E. Abou-Zeid, *Environment, Development and Sustainability*, 2018, **22**, 17-32.

25. A. Bridgewater, *Thermal Science*, 2004, **8**, 21-50.
26. S. Xiu and A. Shahbazi, *Renewable and Sustainable Energy Reviews*, 2012, **16**, 4406-4414.
27. E. Lazzari, T. Schena, M. C. A. Marcelo, C. T. Primaz, A. N. Silva, M. F. Ferrao, T. Bjerck and E. B. Caramao, *Industrial Crops and Products*, 2018, **111**, 856-864.
28. A. Oasmaa, D. C. Elliott and J. Korhonen, *Energy & Fuels*, 2010, **24**, 6548-6554.
29. W. N. R. W. Isahak, M. W. M. Hisham, M. A. Yarmo and T. Y. Y. Hin, *Renew Sust Energ Rev*, 2012, **16**, 5910-5923.
30. M. H. Rahman, P. R. Bhoi and P. L. Menezes, *Renew Sust Energ Rev*, 2023, **188**.
31. P. T. Williams, *Waste Manag*, 2013, **33**, 1714-1728.
32. H.-P. Schmidt and K. Wilson, The 55 uses of biochar, the Biochar Journal 2014, <https://www.biochar-journal.org/en/ct/2>, (accessed 16/11/2023, 2023).
33. Q. Hu, J. Jung, D. Chen, K. Leong, S. Song, F. Li, B. C. Mohan, Z. Yao, A. K. Prabhakar, X. H. Lin, E. Y. Lim, L. Zhang, G. Souradeep, Y. S. Ok, H. W. Kua, S. F. Y. Li, H. T. W. Tan, Y. Dai, Y. W. Tong, Y. Peng, S. Joseph and C. H. Wang, *Sci Total Environ*, 2021, **757**, 143820.
34. J. Maroušek, O. Strunecký and V. Stehel, *Clean Technologies and Environmental Policy*, 2019, **21**, 1389-1395.
35. E. Batista, J. Shultz, T. T. S. Matos, M. R. Fornari, T. M. Ferreira, B. Szpoganicz, R. A. de Freitas and A. S. Mangrich, *Sci Rep*, 2018, **8**, 10677.
36. A. Smetanová, M. Dotterweich, D. Diehl, U. Ulrich and N. F. Dotterweich, *Zeitschrift für Geomorphologie, Supplementary Issues*, 2013, **57**, 111-134.

37. J. Maroušek, V. Stehel, M. Vochozka, L. Kolář, A. Maroušková, O. Strunecký, J. Peterka, M. Kopecký and S. Shreedhar, *Journal of Cleaner Production*, 2019, **218**, 459-464.
38. D. Grunwald, M. Kaiser, S. Junker, S. Marhan, H. P. Piepho, C. Poll, C. Bammingner and B. Ludwig, *Agr Ecosyst Environ*, 2017, **241**, 79-87.
39. J. Mumme, J. Getz, M. Prasad, U. Luder, J. Kern, O. Masek and W. Buss, *Chemosphere*, 2018, **207**, 91-100.
40. S. Jha, R. Gaur, S. Shahabuddin and I. Tyagi, *Toxics*, 2023, **11**.
41. Priyanka, D. Vashisht, M. J. Taylor and S. K. Mehta, *Frontiers in Environmental Science*, 2023, **11**.
42. X. Tan, Y. Liu, G. Zeng, X. Wang, X. Hu, Y. Gu and Z. Yang, *Chemosphere*, 2015, **125**, 70-85.
43. L. Rodgers, Climate change: The massive CO2 emitter you may not know about).
44. S. S. Senadheera, S. Gupta, H. W. Kua, D. Hou, S. Kim, D. C. W. Tsang and Y. S. Ok, *Cement and Concrete Composites*, 2023, **143**, 105204.
45. G. Mackenzie, A. N. Boa, A. Diego-Taboadal, S. L. Atkin and T. Sathyapalan, *Frontiers in Materials*, 2015, **2**.
46. S. Y. Li, Y. Y. Xu, X. Jing, G. Yilmaz, D. G. Li and L. S. Turng, *Compos Part B-Eng*, 2020, **196**.
47. Q. Zhuo, Y. Liang, Y. Hu, M. Shi, C. Zhao and S. Zhang, *Carbon Research*, 2023, **2**.
48. A. Çay, J. Yanık, Ç. Akduman, G. Duman and H. Ertaş, *Journal of Cleaner Production*, 2020, **251**.
49. J. Layek, R. Narzari, S. Hazarika, A. Das, K. Rangappa, S. Devi, A. Balusamy, S. Saha, S. Mandal, R. G. Idapuganti, S. Babu, B. U. Choudhury and V. K. Mishra, *Sustainability*, 2022, **14**.

50. J. A. Mathews, *Energy Policy*, 2008, **36**, 3633-3639.
51. C. I. partners, CARBON CREDITS EXPLAINED, <https://www.climateimpact.com/services-projects/carbon-credits-explained-what-they-are-and-how-they-work/>).
52. J. Lee, K.-H. Kim and E. E. Kwon, *Renewable and Sustainable Energy Reviews*, 2017, **77**, 70-79.
53. R. Pereira Lopes and D. Astruc, *Coordination Chemistry Reviews*, 2021, **426**.
54. H. Lyu, Q. Zhang and B. Shen, *Chemosphere*, 2020, **240**, 124842.
55. A. Kumar, J. Kumar and T. Bhaskar, *Environ Res*, 2020, **186**, 109533.
56. D. Yao, Q. Hu, D. Wang, H. Yang, C. Wu, X. Wang and H. Chen, *Bioresour Technol*, 2016, **216**, 159-164.
57. B. Nejati, P. Adami, A. Bozorg, A. Tavasoli and A. H. Mirzahosseini, *Journal of Analytical and Applied Pyrolysis*, 2020, **152**.
58. S. Wang, C. Zhao, R. Shan, Y. Wang and H. Yuan, *Energy Conversion and Management*, 2017, **139**, 89-96.
59. A. Fuente-Hernández, R. Lee, N. Béland, I. Zamboni and J.-M. Lavoie, *Energies*, 2017, **10**.
60. B. Tian, S. Mao, F. Guo, J. Bai, R. Shu, L. Qian and Q. Liu, *Energy*, 2022, **242**.
61. N. S. Azman, N. Khairuddin, T. S. M. Tengku Azmi, S. Seenivasagam and M. A. Hassan, *Catalysts*, 2023, **13**.
62. X. L. Wang, Y. Y. Liu, L. J. Zhu, Y. C. Li, K. G. Wang, K. Z. Qiu, N. Tippayawong, P. Aggarangsi, P. Reubroycharoen and S. R. Wang, *Journal of Co2 Utilization*, 2019, **34**, 733-741.
63. M. L. Nieva Lobos, J. M. Sieben, V. Comignani, M. Duarte, M. A. Volpe and E. L. Moyano, *International Journal of Hydrogen Energy*, 2016, **41**, 10695-10706.

64. Z. Guo, G. Bai, B. Huang, N. Cai, P. Guo and L. Chen, *J Hazard Mater*, 2021, **408**, 124802.
65. J. Wu, Y. Yi, Y. Li, Z. Fang and E. P. Tsang, *J Hazard Mater*, 2016, **320**, 341-349.
66. J. de Barros Dias Moreira, D. Bastos de Rezende and V. Márcia Duarte Pasa, *Fuel*, 2020, **269**.
67. P. Lu, Q. X. Huang, Y. Chi and J. H. Yan, *Journal of Analytical and Applied Pyrolysis*, 2017, **127**, 47-56.
68. S. Li, Z. Gu, B. E. Bjornson and A. Muthukumarappan, *Journal of Environmental Chemical Engineering*, 2013, **1**, 1174-1181.
69. R. Ormsby, J. R. Kastner and J. Miller, *Catalysis Today*, 2012, **190**, 89-97.
70. F. Y. Qing-yan Liu, Zhi-hua Liu, Gang Li, *Journal of Industrial and Engineering Chemistry*, 2015, **26**, 46-54.
71. C. Zhang, Z. Cheng, Z. Fu, Y. Liu, X. Yi, A. Zheng, S. R. Kirk and D. Yin, *Cellulose*, 2016, **24**, 95-106.
72. M. D. Kostić, A. Bazargan, O. S. Stamenković, V. B. Veljković and G. McKay, *Fuel*, 2016, **163**, 304-313.
73. T. Dong, D. Gao, C. Miao, X. Yu, C. Degan, M. Garcia-Pérez, B. Rasco, S. S. Sablani and S. Chen, *Energy Conversion and Management*, 2015, **105**, 1389-1396.
74. B. X. Shen, J. H. Chen, S. J. Yue and G. L. Li, *Fuel*, 2015, **156**, 47-53.
75. J. R. Kim and E. Kan, *Journal of Environmental Management*, 2016, **180**, 94-101.
76. S. Manocha, L. M. Manocha, P. Joshi, B. Patel, G. Dangi and N. Verma, 2013.
77. Z. Z. Guo, A. Zhang, J. Zhang, H. Liu, Y. Kang and C. L. Zhang, *Powder Technology*, 2017, **309**, 74-78.
78. J. Hayashi, A. Kazehaya, K. Muroyama and A. P. Watkinson, *Carbon*, 2000, **38**, 1873-1878.

79. X. F. Tan, S. B. Liu, Y. G. Liu, Y. L. Gu, G. M. Zeng, X. J. Hu, X. Wang, S. H. Liu and L. H. Jiang, *Bioresour Technol*, 2017, **227**, 359-372.
80. A. K. Sakhiya, A. Anand and P. Kaushal, *Biochar*, 2020, **2**, 253-285.
81. S. Anto, M. P. Sudhakar, T. S. Ahamed, M. S. Samuel, T. Mathimani, K. Brindhadevi and A. Pugazhendhi, *Fuel*, 2021, **285**.
82. C. D. Venkatachalam, S. Sekar, M. Sengottian, S. R. Ravichandran and P. Bhuvaneshwaran, *Journal of Energy Storage*, 2023, **67**.
83. M. G. Lussier, J. C. Shull and D. J. Miller, *Carbon*, 1994, **32**, 1493-1498.
84. S. Nagano, H. Tamon, T. Adzumi, K. Nakagawa and T. Suzuki, *Carbon*, 2000, **38**, 915-920.
85. E. C. Bernardo, R. Egashira and J. Kawasaki, *Carbon*, 1997, **35**, 1217-1221.
86. A. Somy, M. R. Mehrnia, H. D. Amrei, A. Ghanizadeh and M. Safari, *International Journal of Greenhouse Gas Control*, 2009, **3**, 249-254.
87. K. W. Cheah, M. J. Taylor, A. Osatiashtiani, S. K. Beaumont, D. J. Nowakowski, S. Yusup, A. V. Bridgwater and G. Kyriakou, *Catalysis Today*, 2020, **355**, 882-892.
88. K. W. Cheah, S. Yusup, G. Kyriakou, M. Ameen, M. J. Taylor, D. J. Nowakowski, A. V. Bridgwater and Y. Uemura, *International Journal of Hydrogen Energy*, 2019, **44**, 20678-20689.
89. K. W. Cheah, S. Yusup, M. J. Taylor, B. S. How, A. Osatiashtiani, D. J. Nowakowski, A. V. Bridgwater, V. Skoulou, G. Kyriakou and Y. Uemura, *Reaction Chemistry & Engineering*, 2020, **5**, 1682-1693.
90. A. Volperts, A. Plavniece, G. Dobele, A. Zhurinsh, I. Kruusenberg, K. Kaare, J. Locs, L. Tamasauskaite-Tamasiunaite and E. Norkus, *Renewable Energy*, 2019, **141**, 40-45.
91. S. Sircar, T. C. Golden and M. B. Rao, *Carbon*, 1996, **34**, 1-12.

92. Z. Zhang, Y. Zhang, C. Jiang, D. Li, Z. Zhang, K. Wang, W. Liu, X. Jiang, Y. Rao, C. Xu, X. Chen and N. Meng, *Desalination*, 2022, **529**.
93. S. T. Senthilkumar, R. K. Selvan and J. S. Melo, presented in part at the CARBON MATERIALS 2012 (CCM12): Carbon Materials for Energy Harvesting, Environment, Nanoscience and Technology, Mumbai, India, 2013.
94. L. J. Zhu, S. Yin, Q. Q. Yin, H. X. Wang and S. R. Wang, *Energy Science & Engineering*, 2015, **3**, 126-134.
95. J. Hu, Z. Zhou, R. Zhang, L. Li and Z. Cheng, *Journal of Molecular Catalysis A: Chemical*, 2014, **381**, 61-69.
96. ChemAnalyst, *Global Styrene Market Analysis Report 2023: Plant Capacity, Production, Process, Technology, Operating Efficiency, Demand & Supply, End-Use, Foreign Trade, Sales Channel, Company Share, 2015-2030*, Report 5743474, 2023.
97. A. S. Fedotov, I. Uvarov, M. V. Tsodikov, S. Paul, P. Simon, M. Marinova and F. Dumeignil, *Chem Eng Process*, 2021, **160**.
98. P. V. Markov, I. S. Mashkovsky, G. O. Bragina, J. Wärnå, E. Y. Gerasimov, V. I. Bukhtiyarov, A. Y. Stakheev and D. Y. Murzin, *Chemical Engineering Journal*, 2019, **358**, 520-530.
99. H. Zhou, C. Wu, J. A. Onwudili, A. Meng, Y. Zhang and P. T. Williams, *Waste Manag*, 2015, **36**, 136-146.
100. X. Wang and M. A. Keane, *Journal of Chemical Technology & Biotechnology*, 2019, **94**, 3772-3779.
101. M. Hu, L. Jin, Y. Dang, S. L. Suib, J. He and B. Liu, *Front Chem*, 2020, **8**, 581512.
102. Y. L. Shen, K. J. Yin, C. H. An and Z. H. Xiao, *Applied Surface Science*, 2018, **456**, 1-6.

103. Z. Wang, L. Yang, R. Zhang, L. Li, Z. Cheng and Z. Zhou, *Catalysis Today*, 2016, **264**, 37-43.
104. J. Lian, Y. Chai, Y. Qi, X. Guo, N. Guan, L. Li and F. Zhang, *Chinese Journal of Catalysis*, 2020, **41**, 598-603.
105. B. A. Wilhite, M. J. McCreedy and A. Varma, *Ind Eng Chem Res*, 2002, **41**, 3335-3504.
106. X. D. Wang and M. A. Keane, *J Chem Technol Biot*, 2019, **94**, 3772-3779.
107. L. Yang, S. Y. Yu, C. Peng, X. C. Fang, Z. M. Cheng and Z. M. Zhou, *Journal of Catalysis*, 2019, **370**, 310-320.
108. Y. Liu, W. Guo, X. J. Li, P. Jiang, N. Zhang and M. H. Liang, *Acs Applied Nano Materials*, 2021, **4**, 5292-5300.
109. A. Zharmagambetova, A. Auyezkhanova, E. Talgatov, A. Jumekeyeva, F. Buharbayeva, S. Akhmetova, Z. Myltykbayeva and J. M. L. Nieto, *Journal of Nanoparticle Research*, 2022, **24**.
110. A. W. Augustyniak and A. M. Trzeciak, *Inorganica Chimica Acta*, 2022, **538**.
111. O. A. Kirichenko, L. M. Kozlova, G. I. Kapustin and E. A. Redina, *Russian Journal of Physical Chemistry A*, 2020, **94**, 54-57.
112. S. K. Johnston, N. Cherkasov, E. Pérez-Barrado, A. Aho, D. Y. Murzin, A. O. Ibhaddon and M. G. Francesconi, *Applied Catalysis A: General*, 2017, **544**, 40-45.
113. N. Cherkasov, A. Ibhaddon, A. J. Mccue, J. A. Anderson and S. K. Johnston, *Appl Catal a-Gen*, 2015, **497**, 22-30.
114. N. Cherkasov, A. O. Ibhaddon and E. V. Rebrov, *Applied Catalysis A: General*, 2016, **515**, 108-115.

115. M. García-Mota, J. Gómez-Díaz, G. Novell-Leruth, C. Vargas-Fuentes, L. Bellarosa, B. Bridier, J. Pérez-Ramírez and N. López, *Theoretical Chemistry Accounts*, 2010, **128**, 663-673.
116. H. Lindlar, R. Dubuis, F. N. Jones and B. C. McKusick, *Organic Syntheses*, 1966, **46**.
117. M. J. Islam, M. Granollers Mesa, A. Osatiashtiani, M. J. Taylor, M. A. Isaacs and G. Kyriakou, *Nanomaterials (Basel)*, 2023, **13**.
118. A. C. M. Loy, S. Y. Teng, B. S. How, X. X. Zhang, K. W. Cheah, V. Butera, W. D. Leong, B. L. F. Chin, C. L. Yiin, M. J. Taylor and G. Kyriakou, *Progress in Energy and Combustion Science*, 2023, **96**.
119. O. Bag, K. Tekin and S. Karagoz, *Fuller Nanotub Car N*, 2020, **28**, 1030-1037.
120. W. J. Liu, H. Jiang and H. Q. Yu, *Chem Rev*, 2015, **115**, 12251-12285.
121. R. Sharma, V. Palled, R. R. Sharma-Shivappa and J. Osborne, *Appl Biochem Biotechnol*, 2013, **169**, 761-772.
122. A. M. Dekhoda, E. Gyenge and N. Ellis, *Biomass Bioenerg*, 2016, **87**, 107-121.
123. Y. Fu, Y. Shen, Z. Zhang, X. Ge and M. Chen, *Sci Total Environ*, 2019, **646**, 1567-1577.
124. F. Abbaci, A. Nait-Merzoug, O. Guellati, A. Harat, J. El Haskouri, J. Delhalle, Z. Mekhalif and M. Guerioune, *Journal of Analytical and Applied Pyrolysis*, 2022, **162**.
125. P. R. Yaashikaa, P. S. Kumar, S. Varjani and A. Saravanan, *Biotechnol Rep (Amst)*, 2020, **28**, e00570.
126. P. Sinha, A. Datar, C. Jeong, X. P. Deng, Y. G. Chung and L. C. Lin, *J Phys Chem C*, 2019, **123**, 20195-20209.
127. L. E. Smart and E. A. Moore, Taylor & Francis, 3rd Edition edn., 2005, p. 432.
128. C. Yu, P. Thy, L. Wang, S. N. Anderson, J. S. VanderGheynst, S. K. Upadhyaya and B. M. Jenkins, *Fuel Processing Technology*, 2014, **128**, 43-53.

129. H. A. Alabdrabalameer, M. J. Taylor, J. Kauppinen, T. Soini, T. Pikkarainen and V. Skoulou, *Sustainable Energy & Fuels*, 2020, **4**, 3764-3772.
130. X. B. Wang, A. Adeosun, Z. F. Hu, Z. H. Xiao, D. Khatri, T. X. Li, H. Z. Tan and R. L. Axelbaum, *Proceedings of the Combustion Institute*, 2019, **37**, 2705-2713.
131. M. J. Taylor, H. A. Alabdrabalameer, A. K. Michopoulos, R. Volpe and V. Skoulou, *Acs Sustainable Chemistry & Engineering*, 2020, **8**, 5674-5682.
132. M. Raud, L. Rocha-Meneses, D. J. Lane, O. Sippula, N. J. Shurpali and T. Kikas, *Processes*, 2021, **9**.
133. C. Quan, N. B. Gao and Q. B. Song, *Journal of Analytical and Applied Pyrolysis*, 2016, **121**, 84-92.
134. D. Puglia, F. Luzi, M. Lilli, F. Sbardella, M. Pauselli, L. Torre and P. Benincasa, *Industrial Crops and Products*, 2020, **154**.
135. M. J. Taylor, K. Hornsby, K. W. Cheah, P. Hurst, S. Walker and V. Skoulou, *Sustainable Chemistry for the Environment*, 2024, **7**.
136. X. F. Sun, Z. X. Jing, P. Fowler, Y. G. Wu and M. Rajaratnam, *Industrial Crops and Products*, 2011, **33**, 588-598.
137. A. Tomczyk, Z. Sokolowska and P. Boguta, *Rev Environ Sci Bio*, 2020, **19**, 191-215.
138. K. Wystalska and A. Kwarciak-Kozłowska, *Materials (Basel)*, 2021, **14**.
139. J. J. Corral-Pérez, C. Copéret and A. Urakawa, *Journal of Catalysis*, 2019, **380**, 153-160.
140. R. Molaie, K. Farhadi, M. Forough and S. Hajizadeh, *J Nanostruct*, 2018, **8**, 47-54.
141. C. H. Y. Gyu Hwan Oh, Chong Rae Park, *Carbon Science*, 2003, **4**, 180-184.
142. Y. Xu, G. Yin, Y. Ma, P. Zuo and X. Cheng, *Journal of Materials Chemistry*, 2010, **20**, 3216-3220.

143. X. Kang, L. Wu, J. Xu, D. Liu, Q. Song and Y. Hu, *IOP Conference Series: Materials Science and Engineering*, 2020, **892**.
144. S. M. Lee, S. H. Lee and J. S. Roh, *Crystals*, 2021, **11**.

Appendix 1:

An overview of a typical phenylacetylene reaction where there is a linear conversion over time.

All activation energy calculations and initial rate calculations utilized the change in concentration between the start and first hour of reaction.

